# ANNUAL REPORT

Center for Experimental Nuclear Physics and Astrophysics
University of Washington
May, 2007

Sponsored in part by the United States Department of Energy
under Grant #DE-FG02-97ER41020.

Cover photos, from top to bottom: John Amsbaugh, Tom Burritt and Sean McGee removing the SNO NCD's, Michelle Leber in front of the KATRIN vacuum vessel, and the short-range gravity pendulum.

# INTRODUCTION

CENPA pursues a broad program of research in nuclear physics, astrophysics and related fields. Research activities are conducted locally and at remote sites. CENPA is a major participant in the Sudbury Neutrino Observatory (SNO), the KATRIN tritium beta decay experiment and the Majorana double-beta decay experiment. The current program includes "in-house" research on nuclear astrophysics and fundamental interactions using the local tandem Van de Graaff, as well as local and remote non-accelerator research on fundamental interactions and user-mode research on relativistic heavy ions at large accelerator facilities in the U.S. and Europe.

We thank our external advisory committee, Baha Balantekin, Russell Betts, and Stuart Freedman, for their continuing valuable recommendations and advice. The committee reviewed our program in May, 2005.

Data-taking on the Sudbury Neutrino Observatory project ended November 28, 2006, concluding six highly successful years in which the solar neutrino problem was resolved and new neutrino properties measured. As the heavy water is being returned to the owners, the data from the final phase, during which $^3$He-filled proportional counters were deployed in SNO, are being analyzed. A clear neutron signal is seen and significantly improved precision on the mixing angle $\theta_{12}$ can be expected.

The completion of the main KATRIN spectrometer, its very successful vacuum test and spectacular delivery to the FZK marked the the achievement of a major KATRIN milestone. The UW played a prominent role in the commissioning of the pre-spectrometer, yielding valuable lessons on Penning traps which will be applied to the main spectrometer. Following a review in November, the DOE recently announced its decision to fund the US-KATRIN proposal. This will enable purchasing of long lead-time items to begin, with forward funding assistance being provided by the University of Washington to ease funding profiles.

Our recent test of the gravitational inverse-square law showed that the law is valid at 95% confidence for length scales down to 56 micrometers. This result places a model-independent limit of 44 micrometers on the largest possible size of an extra dimension. It rules out the interpretation of the PVLAS "birefringence of the vacuum" measurement in terms of a low-mass spin-0 meson, and is inconsistent with "natural values" for the chameleon mechanism that was invented to evade experimental limits on string theory's predicted low-mass scalar particles

We have nearly completed our precision $^3$He + $^4$He fusion measurements, with data from counting both the prompt and the activity gamma-rays over the energy range $E_{c.m.}$ = 420 - 1230 keV, and one more lower energy point to be measured. A new beamline has been constructed for our $^{22}$Na destruction experiment, and the target chamber has been designed.

We finished an analysis of data that yields the branch for the $0^+ \rightarrow 0^+$ transition in $^{32}$Ar, which allows an experimental determination of the isospin-breaking correction and a stringent test of calculations.

We have made significant improvements in our production of Ultra Cold Neutrons at Los Alamos, which has allowed us to measure the beta-decay spectrum from UCN at a

rate of approximately 2 Hz. We expect to get a determination of the beta asymmetry to approximately 2% by the end of 2007.

We have completed a survey of minijet number and pt correlations on A-A collision energy and centrality, indicating that minijets form a strong contribution to RHIC A-A collisions although they are strongly altered in central collisions. We are now using the same analysis system to study elliptic flow on its own and relative to minijets, to reconsider its hydrodynamic interpretation and possible alternatives.

Axion Dark Matter eXperiment: We have nearly finished construction and are planning to start commissioning this summer. We anticipate the data-taking will take about a year. The collaboration has endorsed the plan to move the experiment to the University of Washington/CENPA. We plan to submit a proposal to DOE/HEP for this Phase II of the project in summer 2007 for a fall 2008 construction start.

We received DOE/NA22 funding for a large-channel-count TPC for indentification of special nuclear material. The readout electronics and software will be the responsibility of CENPA.

Two CENPA graduate students obtained their Ph.D. degree during the period of this report.

As always, we encourage outside applications for the use of our facilities. As a convenient reference for potential users, the table on the following page lists the capabilities of our accelerators. For further information, please contact Prof. Derek W. Storm, Executive Director, CENPA, Box 354290, University of Washington, Seattle, WA 98195; (206) 543-4080, or storm@npl.washington.edu. Further information is also available on our web page: http://www.npl.washington.edu.

We close this introduction with a reminder that the articles in this report describe work in progress and are not to be regarded as publications or to be quoted without permission of the authors. In each article the names of the investigators are listed alphabetically, with the primary author underlined, to whom inquiries should be addressed.

Derek Storm, Editor

Debra Nastaj, Assistant Editor

## TANDEM VAN DE GRAAFF ACCELERATOR

A High Voltage Engineering Corporation Model FN purchased in 1966 with NSF funds, operation funded primarily by the U.S. Department of Energy. See W. G. Weitkamp and F. H. Schmidt, "The University of Washington Three Stage Van de Graaff Accelerator," Nucl. Instrum. Methods **122**, 65 (1974). Recently adapted to an (optional) terminal ion source and a non-inclined tube #3, which enables the accelerator to produce high intensity beams of helium and hydrogen isotopes at energies from 100 keV to 7.5 MeV.

Some Available Energy Analyzed Beams

| Ion | Max. Current (particle $\mu$A) | Max. Energy (MeV) | Ion Source |
|---|---|---|---|
| $^{1}$H or $^{2}$H | 50 | 18 | DEIS or 860 |
| $^{3}$He or $^{4}$He | 2 | 27 | Double Charge-Exchange Source |
| $^{3}$He or $^{4}$He | 30 | 7.5 | Tandem Terminal Source |
| $^{6}$Li or $^{7}$Li | 1 | 36 | 860 |
| $^{11}$B | 5 | 54 | 860 |
| $^{12}$C or $^{13}$C | 10 | 63 | 860 |
| $^{*14}$N | 1 | 63 | DEIS or 860 |
| $^{16}$O or $^{18}$O | 10 | 72 | DEIS or 860 |
| F | 10 | 72 | DEIS or 860 |
| $^{*}$ Ca | 0.5 | 99 | 860 |
| Ni | 0.2 | 99 | 860 |
| I | 0.001 | 108 | 860 |

*Negative ion is the hydride, dihydride, or trihydride.

Additional ion species available including the following: Mg, Al, Si, P, S, Cl, Fe, Cu, Ge, Se, Br and Ag. Less common isotopes are generated from enriched material.
In addition, we are now producing a separated beam of 15-MeV $^{8}$B at 6 particles/second.

## BOOSTER ACCELERATOR

See "Status of and Operating Experience with the University of Washington Superconducting Booster Linac," D. W. Storm *et al.*, Nucl. Instrum. Methods A **287**, 247 (1990). The Booster is presently in a "mothballed" state.

# Contents

**INTRODUCTION** **i**

**1 Neutrino Research** **1**

**SNO** **1**

1.1 Status of the SNO Project . . . . . 1

**SNO NCDs** **3**

1.2 Stability of the NCD array during SNO phase III . . . . . 3

1.3 Development of the NCD pulse simulation . . . . . 5

1.4 Revisiting the Deployed NCD tilts in SNO . . . . . 6

1.5 Resistive coupler disconnect and NCD data quality . . . . . 7

1.6 A new external alpha counter for the SNO neutral current detectors . . . . . 8

1.7 Energy losses of protons and alphas in NCDs and energy spectra of alphas from the counter walls . . . . . 9

**KATRIN** **11**

1.8 Status of the CENPA contribution to the KATRIN experiment . . . . . 11

1.9 Status of the KATRIN detector mechanical design . . . . . 13

1.10 Commissioning of the KATRIN pre-spectrometer system . . . . . 15

1.11 Updates on simulation for KATRIN detector backgrounds . . . . . 16

1.12 Electron gun for profiling silicon detectors for KATRIN . . . . . 17

1.13 Development of an in-situ dead-layer measurement for the KATRIN detector 19

**Majorana** **21**

1.14 The Majorana neutrinoless double-beta decay experiment . . . . . 21

1.15 Surface contamination simulations for the proposed Majorana neutrinoless double-beta decay experiment . . . . . 23

1.16 Validation of cosmic-ray muon-induced physics within the GEANT4-based simulation and analysis package MaGe . . . . . 24

1.17 Development of technologies for low-background experiments using the MEGA cryostat . . . . . 25

1.18 Low-energy neutron response of germanium detectors in MaGe/GEANT4 . . 26

1.19 LArGe, Liquid Argon Compton suppressed Germanium crystal . . . . . 27

1.20 Design, construction and operation of a small-scale radioactivity assay chamber 29

**2 Fundamental Symmetries and Weak Interactions 30**

**Torsion Balance Experiments 30**

2.1 Torsion balance search for spin coupled forces . . . . . 30

2.2 Tests of the gravitational inverse-square law below the dark-energy length scale 31

2.3 Particle physics implications of our recent test of the gravitational inverse square law . . . . . 33

2.4 A new limit on a P- and T-violating force . . . . . 35

2.5 Laboratory test of Newton's second law in the limit of small accelerations . . 36

2.6 Rotating torsion balance test of the weak equivalence principle for beryllium and titanium . . . . . 37

2.7 Development of a pendulum to test short range spin-spin interactions . . . . 38

2.8 Continued progress toward improved torsion fibers . . . . . 39

2.9 New short range test of Gauss' law for gravity . . . . . 40

2.10 Wedge Pendulum: A new test of the gravitational inverse-square law . . . . 41

2.11 Investigations of small thermal gradient and electrostatic effects for LISA . . 42

2.12 Initial results from the APOLLO lunar-laser ranging experiment . . . . . 43

**Weak Interactions 44**

2.13 NSAC - the data acquisition and control system for the parity non-conserving neutron spin rotation experiment . . . . . 44

2.14 Parity non-conserving neutron spin rotation experiment . . . . . 45

2.15 Nuclear reactions of $^{32}$Ar in Si . . . . . 46

2.16 $^{100}$Tc electron-capture branching ratio with a Penning Trap . . . . . 47

2.17 Status of the ultra-cold neutron $A_\beta$ experiment at Los Alamos . . . . . 49

2.18 Characterization of ultracold neutron detectors for use in the UCNA experiment at LANL . . . . . 50

**Quantum Optics** **52**

2.19 A test of quantum nonlocal communication . . . . . 52

**3 Nuclear Astrophysics** **55**

3.1 Precision measurements of the $^3$He($\alpha$,$\gamma$)$^7$Be cross section . . . . . 55

3.2 E0 emission in $\alpha$ + $^{12}$C fusion at astrophysical energies . . . . . 56

3.3 Motivation for Measuring the $^{22}$Na(p,$\gamma$)$^{23}$Mg Reaction Rate . . . . . 58

3.4 Technical developments of the $^{22}$Na(p,$\gamma$)$^{23}$Mg experiment . . . . . 59

**4 Nuclear Structure** **61**

4.1 Investigation of states in $^{33}$Cl using $^{32}$S$(p,\gamma)$ . . . . . 61

4.2 Measurement of the absolute $\gamma$ branches in the decay of $^{32}$Cl . . . . . 62

4.3 Delayed $\gamma$ branches from $^{32}$Ar $\beta$-decay . . . . . 63

**5 Relativistic Heavy Ions** **64**

5.1 Summary of event structure research . . . . . 64

5.2 Accurate centrality determination in A-A collisions down to single N-N collisions 65

5.3 Precision Glauber-model parameterizations and particle production in A-A collisions . . . . . 66

5.4 Charge-independent angular autocorrelations in Au-Au collisions at $\sqrt{s_{NN}}$ = 62 and 200 GeV . . . . . 67

5.5 Particle identified two particle correlations: techniques . . . . . 68

5.6 Identified-particle two-particle correlations: observations . . . . . 69

5.7 Forward-backward correlations in relation to angular autocorrelations . . . . 70

5.8 Monte Carlo simulations of correlation structures . . . . . 71

5.9 Reaction-plane-dependent correlations . . . . . 72

5.10 Distinguishing elliptic flow from "non-flow" in heavy ion collisions . . . . . 73

5.11 Energy and centrality dependence of elliptic flow in Au-Au collisions . . . . . 74

5.12 Is "elliptic flow" a hydrodynamic phenomenon? . . . . . 75

5.13 "Flow" phenomena in nuclear collisions and Brownian motion . . . . . 76

5.14 Opacity and chiral symmetry restoration in heavy ion collisions at RHIC: the DWEF model . . . . . 77

**6 Electronics, Computing, and Detector Infrastructure 79**

6.1 Electronic Equipment . . . . . 79

6.2 Additions to the ORCA DAQ system . . . . . 81

6.3 Laboratory computer systems . . . . . 82

6.4 Studies of energy losses of fast charged particles . . . . . 83

**7 Accelerator and Ion Sources 84**

7.1 Injector deck and ion sources . . . . . 84

7.2 Van de Graaff accelerator operations and development . . . . . 85

7.3 Physical plant maintenance, repairs, and possible upgrade . . . . . 86

7.4 Axion magnet cryostat: mechanical characteristics . . . . . 87

**8 CENPA Personnel 88**

8.1 Faculty . . . . . 88

8.2 CENPA External Advisory Committee . . . . . 88

8.3 Postdoctoral Research Associates . . . . . 88

8.4 Predoctoral Research Associates . . . . . 89

8.5 Research Experience for Undergraduates participants . . . . . 89

8.6 University of Washington undergraduates taking research Credit . . . . . 89

8.7 Professional staff . . . . . 90

8.8 Technical staff . . . . . 90

8.9 Administrative staff . . . . . 90

8.10 Part time staff . . . . . 91

**9 Publications** **92**

9.1 Published papers: . . . . . 92

9.2 Papers submitted or to be published 2006: . . . . . 95

9.3 Invited talks, abstracts and other conference presentations: . . . . . 97

9.4 Ph.D. degrees granted: . . . . . 101

# 1 Neutrino Research

# SNO

## 1.1 Status of the SNO Project

J. F. Amsbaugh, G. A. Cox, J. A. Detwiler, P. J. Doe, C. A. Duba, G. C. Harper, M. A. Howe, S. McGee, A. Myers, N. S. Oblath, R. G. H. Robertson, T. D. Van Wechel, B. A. VanDevender and J. F. Wilkerson

The Sudbury Neutrino Observatory (SNO) detector took its last production data on November 28, 2006, concluding an extraordinarily successful physics experiment that began in November, 1999, and demonstrated that the solar neutrino problem was due to a new neutrino property, flavor conversion. SNO ran in three distinct configurations or phases; pure heavy water, heavy water with dissolved salt, and heavy water with discrete neutron detectors ('NCDs') deployed in it.

Production running began November 27, 2004 with $^3$He-filled proportional counters deployed in the heavy water. There were 36 'strings' of individual counters filled with $^3$He and another four filled with $^4$He for investigation of backgrounds. The total deployed length of counter was 398 m. Two calendar years of good data have been recorded, with a live-time fraction of neutrino data about 63%. Calibrations made up another 30% of the data, and the remaining 7% consisted of maintenance or shutdown time. The fraction of neutrino plus calibration data selected for analysis was 89%. These fractions were significantly higher than for previous phases.

The day after data acquisition ended, a magnitude 4.1 earthquake struck the Sudbury area, and caused significant effects. Some disused drifts in the Garson mine collapsed. In the Creighton mine, there were minor rockfalls, but no serious damage or injury. It initially appeared that the SNO detector emerged unscathed, but five strings of NCDs (I1, J7, M1, M7, and N2) no longer functioned properly. When removal of NCD strings from the heavy water began, it was seen that gas was leaking from string N2 into the water. Inspection with the remotely-operated vehicle (ROV) showed that the five strings had collapsed near the anchor. Remarkably, however, four of them popped back into their circular shape and regained normal function once they were raised out of the water. It was fortunate that this event did not occur during SNO's NCD data-taking phase.

The 'undeployment' process essentially reversed the deployment process of 2003-2004. The calibration hardware and glove box above the neck of the vessel were removed, and the ROV was lowered into the water. Teams of personnel from CENPA, SNO, Guelph, Oxford, Queen's, and Los Alamos began removing the strings, carrying out neutron calibrations at the center of the vessel with an AmBe source encapsulated in the shuttle float that is part of the mechanism to install and remove NCDs. The counter strings, 9 to 11 m in length in SNO, were cut into sections of 5 m or less at the location of welds by means of a pipe cutter. The sections are now stored in racks in the corridor leading to the SNO cavity pending a decision on their possible future use in another application. (It was hoped that they could be incorporated into a lead-based supernova detector called HALO, but the future of HALO

is uncertain.)

Two strings, K2 and K5, had 'hot spots' observable in Cherenkov light, and special plans were made to study these strings on removal. The composition of the hot spots, whether Th, U, or something else, determines the neutron background to be associated with them. The strings were removed without allowing them to come into contact with anything at the locations of the hot spots, and were stored in a tent in the deck clean room. A 1-m long clamshell proportional flow counter was constructed at CENPA to allow the external alpha activity to be studied. The counter has good energy resolution, position resolution, and azimuthal angle resolution in order to better characterize the hot spots. Difficulties, described elsewhere in Sec. 1.6, were experienced commissioning this External Alpha Counter (EAC).

Some strings exhibited a problem termed RCD, or resistive-coupler disconnect, in which the 325-Ω resistive coupler that matches the characteristic impedance of the NCDs to that of the cables was making poor electrical contact. (see Sec. 1.5). The cable bells were opened on those strings, and loose contacts were observed in K2 and M8, cases with clear RCD symptoms in the data. String J3, which produced non-physics events at low energies that resembled neutrons, was also found to have a loose contact (at the cable side of the resistive coupler, unlike K2 and M8). Other suspect strings, I7, K7, L3, and N4, were opened at the cable bell but did not have loose contacts.

The removal of the NCDs was completed successfully on January 18, 2007. Removal of the heavy water began, and by the end of March, 467 tonnes had been taken to the surface. In parallel, distillation of concentrated brine left from the second phase of running with NaCl in the heavy water began. At the end of March, 7 tonnes out of a total of 35 had been distilled.

The array ran successfully, producing a clear neutron signal that is approximately of the magnitude expected from neutral-current disintegration of deuterium by solar neutrinos. Data are being analyzed under blindness protocols designed by the UW group. In those protocols, a concealed fraction of events is dropped from the data, and some muon-follower neutrons are added back in, before the data are studied by analysts. Data analysis is proceeding along two separate paths. The objective in both approaches is to separate the neutron events from other types of event (alphas, betas, 'non-physics' events) and to minimize the overall statistical and systematic uncertainty. One method includes a set of semi-empirical parameters optimized for the separation by various means such as Fisher Discriminants, Boosted Decision Trees, and polynomial fits. The other approach models each pulse in detail based on the physical processes involved in creating and amplifying the ionization signals. The latter approach is also the basis of the Monte Carlo being developed to serve both analysis communities. It is the approach being followed by the UW group, and a description of its status is contained in Sec. 1.3.

# SNO Neutral Current Detectors (NCDs)

## 1.2 Stability of the NCD array during SNO phase III

S. McGee

The Neutral Current Detector (NCD) array at the Sudbury Neutrino Observatory (SNO) was a collection of 40 9-11 m long ultra-clean, sealed $^3$He and $^4$He proportional counters known as NCD strings. Due to limitations on access to the experimental site, it was necessary to construct the NCD strings from three or four 2.0, 2.5 and 3.0 m sections of individual NCD counters immediately before installation into the active region of the SNO detector. Measures were taken to minimize counter-to-counter gain variations during the NCD gas fill but slight variations were unavoidable. To optimize the energy resolution of an NCD string, the individual counters that comprised an NCD string were selected so their gains were well matched.

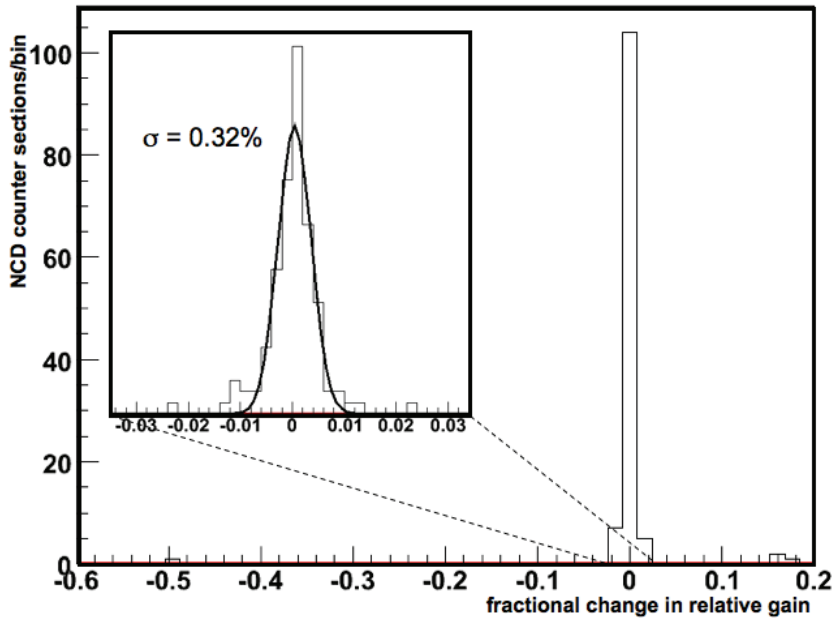


Figure 1.2-1. Plot of the change of gain of the individual counters relative to the string average gain. The majority of the counter relative gains changed very little during the 26 month run time of Phase III. The counter with a relative gain change of -0.5 is the one counter known to have been leaking $^3$He from its active region. This forced the other three counters in that string to have a markedly higher (0.16) relative gain change.

During installation of the NCD array, an AmBe source was placed at the center of each counter section to check electrical continuity of the string and individual counter health before relocation to its assigned location.[1] The source was placed close enough to the counter so approximately 95% of the neutrons captured on the string were captured in the desired

[1]CENPA Annual Report, University of Washington (2004) 22.

counter. The AmBe source allowed for events to be registered by both the $^3$He and $^4$He proportional counters ($\gamma$'s and n's).

Calibrations were done periodically at SNO with neutron-emitting sources attached to a lanyard system. However, this did not allow for the gain of the individual counters of an NCD string to be determined due to limitations in the proximity of source placement and the dispersion of neutrons emitted from the sources. To check individual counter health and stability and the accumulate a large sample of neutron pulses from each counter section, the initial calibration procedure was repeated during the removal of the NCD strings.

During the installation calibrations, the same preamplifier was used to calibrate each NCD counter. However, during the removal calibration, it was desirable to use the preamplifier that had been used with the respective string during the entire NCD run period so the pulse shapes acquired during the calibration could be directly applied in comparison to run-time events. Therefore, to compare the gains of the individual counters at the beginning and the end of Phase III, the gains of the counters relative to the average gain of the entire strings are compared. Deviations in relative gain would be a clear indication of a change in the gain of an individual counter unless, of course, all counters changed in the same way. However, this kind of change would have been seen in the normal calibration of the array and it was not.

Fig. 1.2-1 shows the change in the relative gain of each individual $^3$He counter section with respect to the average gain of the entire string. The majority of the counter sections showed good stability with a deviation of 0.32%. One counter was known to be damaged and leaking $^3$He (into a field-free region of the string) and can be seen as an outlier in Fig. 1.2-1 at -0.5. The other three counters on that string are pushed to a higher fractional difference by this leaking counter, appearing near 0.16, but are themselves still tightly grouped. Not included in this plot are results from the counters of five $^3$He strings that could not be calibrated due to damage incurred during a large earthquake that shook SNO the day after data-taking was completed.

## 1.3 Development of the NCD pulse simulation

N. S. Oblath, R. G. H. Robertson and H. S. Wan Chan Tseung

The events from the Neutral Current Detection (NCD) Array at SNO are current pulses where the integral of the pulse is approximately proportional to the amount of energy deposited in the counter. The shape of the pulse is a result of the energy deposition as a function of ion energy, the geometry of the ionization track within the counter, and a variety of other effects. We want to be able to produce a realistic Monte Carlo data set to show that we understand our detectors and with which we can test our pulse-shape analysis methods. Furthermore, we want to use the neutron-capture and alpha pulse models to fit data pulses. By fitting data pulses with both models we can separate the alpha background pulses from the neutron-capture signal pulses.

Over the past year we have made great progress in improving the models we use for neutron-capture and alpha pulses and the way in which those models are implemented in the SNO Monte Carlo software, SNOMAN. These changes have included:

- Developing a simulation of multiple scattering for the ions in the gas based on the methods used in the SRIM software package,[1]
- Improving our implementation of the ion energy deposition,
- Creating a Monte Carlo simulation of electron drift from scratch to determine the average electron drift speed and diffusion as a function of radius within the counter,
- Adding gas-gain fluctuations and realistic electronics noise,
- Measuring the ion-drift time constant and the energy needed to produce an electron-ion pair,
- Overhauling the electronics and trigger simulations to represent the real system more accurately and to integrate it with the simulation of the SNO PMT system.

A qualitative comparison is shown in the figure below, with data on the left and a simulated pulse on the right. Quantitative comparisons are underway while the last few model improvements are nearing completion.


[1] J. F. Ziegler, *et al.*, in *The Stopping and Ranges of Ions in Matter*, Vol. 1, Pergamon Press (1985).

## 1.4 Revisiting the Deployed NCD tilts in SNO

J. F. Amsbaugh, T. H. Burritt and J. Heise*

Buoyancy should align each neutral current detector, NCD, vertically above its anchor point (AP), but the readout cable at the top of the NCD can pull it out of plumb. The global view camera (GVC), being near the central axis, can only resolve an extreme tilt. At the end of NCD deployment, the GVC and a laser range finder (LRF) were used to estimate these tilts.[1] Similar measurements were done before removing the NCDs. Additional measurements were made with the mounting plate shifted by 7.1 cm. This moved obscured NCDs into the GVC view and provides triangulation. The LRF and GVC angular readouts were replaced, as the ones previous used were inaccurate.

The LRF projects two beams at a known included angle and crossing range enabling triangulation. This is illustrated in Fig. 1.4-1. GVC images of the LRF spots on the NCDs were taken at higher zooms increasing the contrast and resolution. The spot separation measurements need to be corrected for an estimated barrel distortion for the wide angle zooms, mostly the M and N NCD strings. The LRF pointing direction angle is also read out and we use the AV suspension ropes to get the arbitrary offset. The LRF model needed about 5 cm of displacement from the AV axis to minimize the residuals, indicating the mount is not level or the 900-cm long LRF pole is slightly bent. Accuracy is $\pm 0.3°$, consistent with beam width, rope size, and distance. We waited longer for GVC and LRF motions to damp out before taking images with better results. At GVC installation, we discovered the top pole was bent. This particular bend increased the circle swept by the camera center as the pan angle is changed and couples GVC pan and tilt angles when looking from NCD bottom to top, even for a plumb NCD. This requires a more complicated model to analyze GVC top-bottom results. Analysis and a report will be done soon.

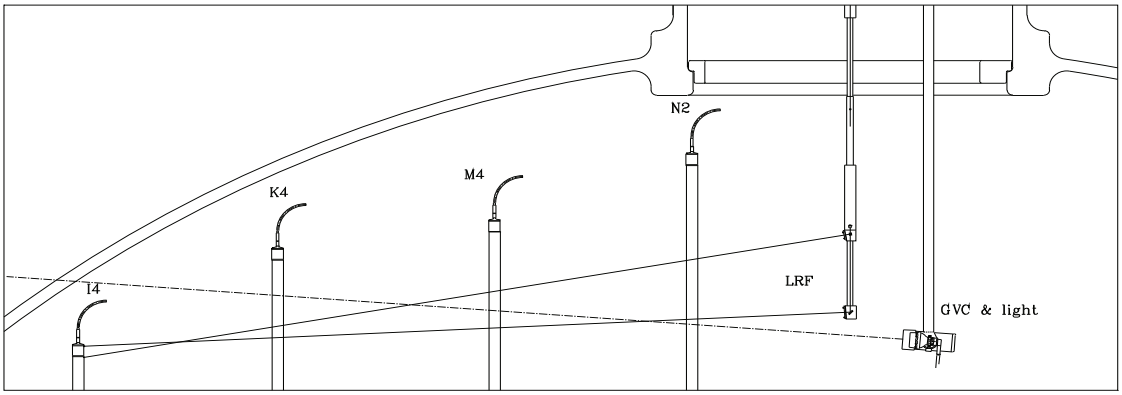


Figure 1.4-1. The laser range finder pointed at NCD string I4 and the GVC pointed at M4. Readout cables truncated.

*Sudbury Neutrino Observatory, Lively, ONT, Canada P3Y 1M3.

[1] CENPA Annual Report, University of Washington (2005) 30.

## 1.5 Resistive coupler disconnect and NCD data quality

T. H. Burritt, G. A. Cox-Mobrand, S. McGee, R. G. H. Robertson and J. F. Wilkerson

During the NCD electronics calibrations, parameters which describe the logarithmic amplification of pulses before they are digitized were observed to deviate significantly from their previous average values for NCD strings 1 (M8) and 31 (K2). Calibration pulses propagate along the NCD cable in the direction opposite of physics signals from the NCD. These pulses observe an impedance mismatch at the junction between the NCD and NCD cable that causes pulse reflections. An examination of the calibration pulses which measured the logamp parameter deviation revealed that the pulse reflection caused by this impedance mismatch was missing from the signal. The NCD and NCD cable are coupled by the "resistive coupler" and based upon this evidence, it is theorized that the resistive coupler disconnected (RCD) from either the NCD or the NCD cable. If true, RCD poses a serious threat to the determination of the detector live-time and NCD data quality.

In response to the RCD theory, a new electronics calibration was devised: the NCD RCD Electronics calibration (NRE). The NRE calibration was initiated in June, 2006, and involves injecting a narrow (78 ns) square wave into the front-end electronics and examining the ensuing pulse reflections. By measuring the amplitude difference between two of the reflection peaks, the presence of the missing reflection can be inferred, since the total injected charge is conserved. The NRE pulse is injected into each NCD electronics circuit once every forty minutes. The missing pulse reflection has not been observed on any other NCDs besides string 1 and 31. (See Fig. 1.5-1).

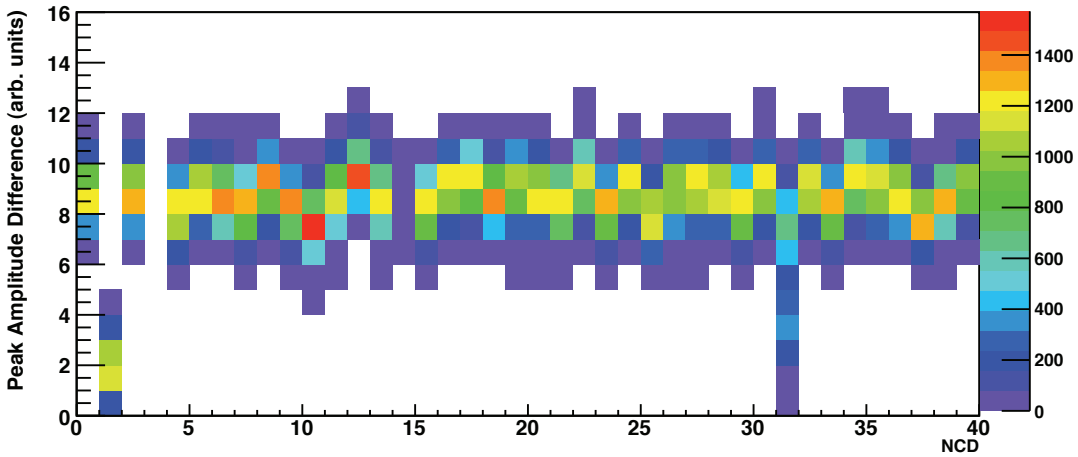


Figure 1.5-1. The difference in peak amplitudes for NRE calibration pulses. NCD strings 1 and 31 indicate a different pulse reflection behavior.

Other attempts to observe RCD behavior have been performed: power spectrum tests, event rate tests, and local bench-tests that attempt to mimic the RCD condition. Tests to measure the time-between-event distribution of various types of noise events have been initiated. A decrease in the rate of these events could be interpreted as a condition for RCD.

## 1.6 A new external alpha counter for the SNO neutral current detectors

N. Gagnon,* S. McGee, A. Myers, R. G. H. Robertson, B. A. VanDevender and T. D. Van Wechel

A new External Alpha Counter (EAC) was constructed at CENPA to count low-level radioactivity on the surfaces of the SNO Neutral Current Detectors (NCDs). This radioactivity produces backgrounds in the SNO detector. If the particular isotopes responsible for these backgrounds can be identified and their strengths determined, the overall systematic uncertainty in SNO's neutral current flux measurement will be significantly reduced for the NCD phase. The EAC is being commissioned at SNO, with counting of NCDs expected to begin in April 2007.

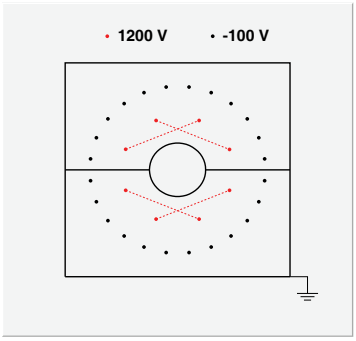


A diagram of the EAC, viewed from the electronics end. The NCD being counted rests in the hole in the middle. The dotted lines show how the anodes are shorted together at the far end. The counter is normally operated with one pair of anodes grounded and the interlaced pair at high voltage.

The EAC is a simple multi-wire proportional counter, sketched in the figure. Its total length is 48 in. The total length includes 3.06 in at the "electronics end" which is filled with wire-binding posts, preamplifiers, and signal and high-voltage connections. Another 2.06-in enclosure at the "far end" contains binding posts and short-circuit jumpers that connect each alternate pair of anode wires. The remaining 42.88-in active volume is filled with P5 gas (95 % Ar, 5 % Methane). The counter is designed so that the symmetric upper and lower halves can be easily separated, allowing insertion of an NCD into a 5-cm diameter opening in the endplates. The NCD is surrounded by a concentric 10 cm diameter ring of 8 active anode wires. The anode wires are made of 25 $\mu$m diameter resistive Stablohm 800. Using resistive anode wires with preamps at each end allows a determination of the longitudinal location of events by a simple charge-division algorithm. Concentric with the NCD and the anode ring is another ring with diameter 16.8 cm consisting of 24 50 $\mu$m diameter copper wires. These wires are held at a small negative potential to suppress events occuring in the outer volume of the EAC.

Nominal conditions for sensitivity to alpha particles with energies in the range from 5–10 MeV are found to occur for an anode voltage $V_a = 1200$ V. However, at these voltages, it was observed that the chamber discharged at a very high rate near the ends of the active volume. The discharges have been temporarily suppressed by coating the anode wire binding posts with an insulating silicone grease. An improved design for the insulating posts is in progress.

*Sudbury Neutrino Observatory, Lively, ONT, Canada P3Y 1M3.

## 1.7 Energy losses of protons and alphas in NCDs and energy spectra of alphas from the counter walls

H. Bichsel, R. G. H. Robertson and H. S. Wan Chan Tseung

The first step in the determination of the pulse shapes in the NCD is a calculation of the track structure of the particles which produce the ionization in the NCD gas. In order to calculate track structures, the collision cross sections $\sigma(E)$ differential in energy loss $E$ for fast charged particles in the gas must be known for both components of the gas (85% by volume of $^3$He and 15% of $CF_4$ at a pressure of 2.5 atm). The Fermi Virtual Photon method (FVP) is used to obtain $\sigma(E)$.[1] The photo-absorption data for He were obtained from the literature.[2,3,4] The total number of collisions per unit length $\Sigma(T)$ ($T$ is the kinetic energy of a proton) for the gas mixture is $0.8/\mu$m at $T = 600$ keV and about $3/\mu$m at $T = 50$ keV. For He-ions the $\Sigma(T)$ are approximately $4\Sigma(T)$ of protons with the same speed (i.e. $T_\alpha \sim 4\ T_p$). In order to calculate the structure of the particle tracks in the gas with 1 $\mu$m segments, a MC calculation with single collisions must therefore be made.

A second problem is the determination of the spectra of the energy deposition in the gas by alpha particles from the wall. Consider alpha particles with energy $T_0$ from a very thin layer in the Ni-wall. If they travel a distance $x$ to the point where they enter the gas, their mean energy $T$ is given implicitly by $R(T) = R(T_0) - x$. They have an energy spectrum $f(T; T_0)$ similar to a Gaussian due to straggling in energy loss. An estimate of the widths of these Gaussians can be made from the literature.[5] Other details are given in Section 6.4 of this report. As an example, a spectrum $f(T)$ of the residual energies below 1 MeV in the gas for 5.4 MeV alphas is given by the solid line in Fig. 1.7-1. Straggling is assumed to be Gaussian, with a full-width-at-half maximum given by the Bohr approximation (approximately 200 keV), reduced by a correction for atomic binding of the electrons. In order to show the importance of straggling, a second function is shown with a straggling-width of 0.01 of the Bohr straggling. Alpha particles are assumed to be produced in an infinitesimal layer every 22 nm inside the Ni, while the FWHM of the Gaussian ($\sim$ 2 keV) is equivalent to 2 nm. Therefore separate straggling functions are seen.

[1] see http://faculty.washington.edu/hbichsel for details.

[2] Joseph Berkowitz, *Atomic and Molecular Photo Absorption*, Academic Press (A division of Harcourt) 2002.

[3] L. C. Lee, E. Phillips and D. L. Judge, J. Chem. Phys. **67**, 1237 (1977).

[4] I. B. Smirnov, Nucl. Instrum. Methods A **554**, 474-493 (2005).

[5] C. Tschalär, Nucl. Instrum. Methods **61**, 141 (1968) and **64**, 237 (1968).

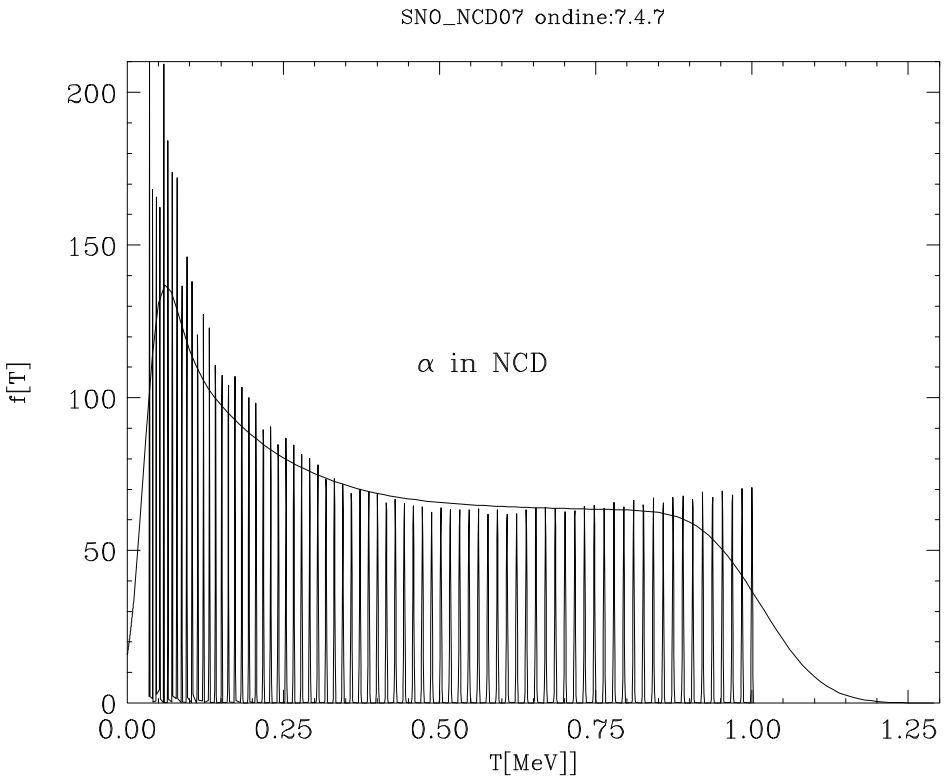


Figure 1.7-1. Energy deposition spectrum in counter gas by alpha particles from the wall. The solid line represents Gaussian straggling with FWHM of 200 keV; the separate functions are calculated with FWHM of 2 keV. Straggling tends to decrease the rise of the spectrum with decreasing energy $T$. For the ionization, a further decrease will occur because of the dependence of $W$ on $T$.

# KATRIN

## 1.8 Status of the CENPA contribution to the KATRIN experiment

T. H. Burritt, P. J. Doe , G. C. Harper, M. A. Howe, M. J. Leber, A. W. Myers, R. G. H. Robertson, B. A. VanDevender, T. D. Van Wechel, B. L. Wall and J. F. Wilkerson.

2006 has been an eventful year for the KATRIN experiment, culminating in the delivery of the main spectrometer vessel. Construction of the vessel was completed in August, 2006. After successful leak checking, the vessel was pumped down using a fore pump to 1.5 x $10^{-3}$ mbar in 48 hours. A single 2800 l/sec turbo-molecular pump was then used to reduce the pressure to 3 x $10^{-7}$ mbar in approximately 20 hours. This is a remarkable achievement for such a large vessel that had not been baked out. After a 9000 km, 60 day voyage the vessel was delivered to the Forschungszentrum, Karlsruhe, and installed in the new spectrometer hall on 29 November, 2006. Subsequently, the vessel has received its thermal insulation and has been attached to the heating/cooling system in preparation for further commissioning.

Commissioning of the pre-spectrometer began in September, 2006. This activity involves two CENPA contributions, the inner electrode system, used to suppress backgrounds originating from the wall of the vessel, and the ORCA data acquisition system. The commissioning exercise was very educational. Significant problems were encountered due to vacuum breakdown conditions that occur in the presence of crossed magnetic and electric fields and to the formation of penning traps. A theoretical understanding of the vacuum breakdown mechanism and the formation of penning traps has been developed. The ability to vary the potential on different parts of the electrode proved to be a valuable diagnostic tool in identifying and understanding the source of the problems. Modifications are underway both to the pre-spectrometer and the main spectrometer to prevent such vacuum breakdown occurring. The ORCA data taking system performed flawlessly during the commissioning exercise.

The pre-spectrometer commissioning made use of a 64 pixel, PIN diode array. Prior to use, the detector was studied using the CENPA, variable energy, electron gun. An important property of the detector is the thickness of the dead layer at the entrance window of the device. The thickness of this layer, which can change due to surface contamination or due to a change in the properties of the device, must be monitored throughout the KATRIN data taking. Two different techniques were investigated. One technique involves varying the angle of incidence of the electron beam. This effectively varied the thickness of the dead layer the beam traversed, allowing an estimate of the layer thickness at normal incidence. Unfortunately, this technique cannot be used in the actual KATRIN experiment, since the angle of incidence cannot be varied. A second technique, involving varying the beam energy, was tested. Both techniques were within reasonable agreement and we are optimistic that the variable energy technique will work well for the KATRIN experiment. This work is described in Sec. 1.13 of this Report.

The electromagnetic design of the overall KATRIN experiment underwent significant changes in 2006. It was determined that the transport magnets that connect the main

spectrometer to the detector system could be discarded without effecting the physics goals of the experiment, thus realizing considerable savings. The detector magnet is in close proximity to the 6-Tesla pinch magnet at the output of the main spectrometer, subjecting both magnets to considerable mechanical loads. It was the recommendation of the magnet experts that the magnets should be designed and commissioned as a pair. As a result we have requested quotes for the pair of magnets as well as quotes for individual magnets. The new electromagnetic design resulted in a new flux tube profile which required slight modification of the internal dimensions of the detector housing.

With the removal of the transport magnets system, the detector is now in more direct contact with the main spectrometer, and therefore the quality of the vacuum in the detector system becomes more critical. In addition, due to the extensive fringe fields associated with the magnets, a new pumping system consisting of cryopumps and non-evaporable getters has been designed. This new vacuum system has been modeled by our KATRIN colleagues at the Accelerator Science and Technology Center, (ASTeC) at the Daresbury Laboratory and found to be compatible with the $10^{-11}$ mbar requirement of the main spectrometer.

The design of the detector system is close to being finalized. Specifications for the detector and the magnet system are complete and preliminary bids have been received for both. As the design matures, modeling of the detector backgrounds has become more detailed, including realistic modeling of the structure of the detector housing using levels of radioactivity obtained by assay of candidate materials. The effects of intrinsic radioactivity and cosmic ray interactions in the magnet have also been incorporated into the model. This work is described in Sec. 1.11 of this Report.

In November the US KATRIN proposal was subject to a DOE Review. The physics goals, technical approach and the strength of the collaboration received strong reviews. At the request of the committee, valuable improvements were made to the management plan. It is anticipated to receive a response by mid-April 2007. If approved, the tentative DOE funding profile will not support immediate purchase of long lead-time, critical path items, such as the magnet system. To address this problem the University has agreed to provide forward funding upon receiving notification of DOE approval. To meet this schedule we rely heavily on the diverse talents of the CENPA staff.

## 1.9 Status of the KATRIN detector mechanical design

T. H. Burritt

In September, 2006 it was realized that considerable savings could be achieved by removing the transport magnets between the main spectrometer and the detector without impacting the physics goals. This optimization of the electromagnetic design in turn required modification of the detector housing design and vacuum pumping systems. The resultant mechanical design is shown in Fig. 1.9-1.

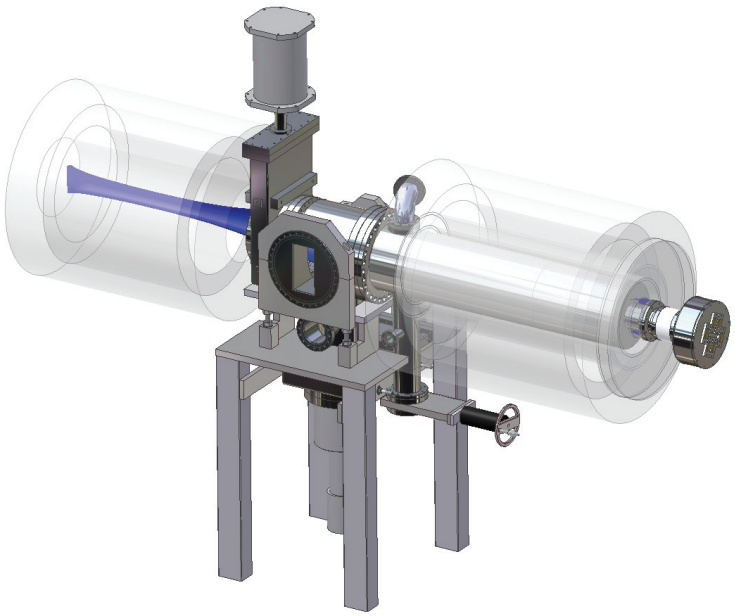

Figure 1.9-1. The general arrangement of the detector vacuum housing. The detector and pinch magnets are ghosted in, the flux tube is shown on the left. Detector signals are extracted through the port on the right.

The pumping system now makes use of cryopumps for both the extreme high vacuum (XHV) region and the medium vacuum region that houses the electronics. The XHV cryopump will be augmented by a non-evaporable getter (NEG) pump to improve hydrogen pumping. The switch from ion pumps to cryopumps was made because the latter are more compatible with high magnetic field environments. Investigations are continuing to determine whether the cryopumps, which contain moving parts, can be replaced by pulse tube coolers which have no moving parts in the cold head and are ideal for high field operation.

The cosmic-ray veto and radiation shield are being designed by our colleagues at MIT. A simple bolt circle on each face of the detector magnet will allow the massive shield and veto to be attached. MIT is also responsible for the calibration system, which consists of a radioactive source and a mono-energetic electron gun that can be scanned over the face of the detector. In order to allow the gun a full range of movement it was necessary to provide square ports as can be seen in Fig. 1.9-1.

Working in conjunction with the engineers at the Forschungszentrum, Karlsruhe (FZK),

a rail system has been designed which supports the magnets and detector system and allows straightforward alignment of the components. This system is being installed at the FZK.

The readout electronics will be provided by the FZK. A scheme for mounting and cooling the detector and the preamplifiers has been approved by the FZK electronics engineering group. The temperature of the detector will be maintained at approximately 120 K. Preliminary tests of the detector cooling scheme have been conducted. Connections between the detector, which sits in the XHV region, and the preamplifiers, which sit in the medium vacuum region, is by means of gold plated pogo-pins. Between 10 - 30 W of heat will need to be removed from the preamplifiers. This will be achieved using liquid nitrogen supplied from a "chicken feeder" system. A commercial company has been identified to provide this system. The front-end electronics sit in the medium vacuum region at the same potential (up to 30 kV) as the post acceleration electrode to which the detector is attached. The scheme for extracting these high potential signal lines from the vacuum chamber can be seen in Fig. 1.9-1.

Fine tuning of the design is currently underway with the goal of producing the detector design manual and holding a final design review at the end of June 2007.

## 1.10 Commissioning of the KATRIN pre-spectrometer system

L. Bornschein,* F. Glück,* M. L. Leber and J. F. Wilkerson

The Karlsruhe Tritium Neutrino experiment (KATRIN) plans to precisely measure the tritium beta-decay electron energy spectrum near the endpoint in order to directly probe the mass of neutrinos in the degenerate region. The highest energy beta-decay electrons from gaseous molecular tritium will be energy analyzed using a 10-m diameter Magnetic Adiabatic Collimation and Electrostatic (MAC-E) spectrometer. This main spectrometer is preceded by a similar but smaller pre-spectrometer that serves as a pre-filter to reduce the number of electrons that enter the main spectrometer. Commissioning of the pre-spectrometer's electric and magnetic systems began in late 2006. Since the design of the main spectrometer is similar, lessons learned at the pre-spectrometer test-setup apply to both spectrometer systems.

In order to measure the transmission function, a photo-electric electron gun was mounted on one end of the pre-spectrometer and Multi-Channel Plate detector on the other. In this configuration the high voltage (up to 35 kV), superconducting magnets (up to 4.5 Tesla), vacuum system, and intrinsic backgrounds could also be tested. In November of 2006, the transmission function was successfully measured at 1 and 1.5 kV. At higher electric and magnetic fields problems were observed in the form of electric breakdown. In order to characterize the problems, a silicon detector was mounted in place of the electron gun. Four measuring devices were used:

- Multi-channel plate detector
- Silicon detector
- Voltage and leakage current read-back of high voltage power supplies
- Ion gauges reading tank vacuum

Electric breakdown occurred when event rates spiked in both detectors, voltage read-back dropped, power supply leakage current increased, and the tank vacuum increased. Vacuum breakdown was observed with voltage settings above 20 kV and no magnetic fields other than earth's natural field. Penning discharges were observed with moderate electric and magnetic fields, starting around 6 kV and 0.1 Tesla. A very high, constant electron background proportional to the electric field setting was observed with no magnetic fields, but it was demonstrated that a more negative potential on the inner electrode could shield these electrons.

In January of 2007, the fields behind the ground cone of the pre-spectrometer were simulated for the first time, confirming Penning traps near the entrance of the pre-spectrometer which could explain the Penning discharge. New electrodes will be manufactured and installed in April 2007 which remove the Penning traps. These new electrodes will also shield sharp edges which could field emit and are the likely the source of the vacuum breakdown. The entrance region to the main spectrometer has also been simulated and electrodes will be designed to prevent similar Penning traps.

*Forschungszentrum Karlsruhe, Institut für Experimentelle Kernphysik, Postfach 3640, 76021 Karlsruhe, Germany.

## 1.11 Updates on simulation for KATRIN detector backgrounds

P. J. Doe, J. Formaggio,* M. L. Leber, R. G. H. Robertson and J. F. Wilkerson

In order to reach the projected neutrino mass sensitivity of 0.2 eV, KATRIN's detector-related backgrounds must be limited to 1 mHz in the energy region of interest. GEANT4-based simulations continue to be used to estimate these backgrounds. As the detector design has evolved and progressed, so have the background simulations. From the silicon detector to the superconducting magnet, the backgrounds from radioactivity in the construction materials, cosmogenics, and interactions of cosmic rays have been estimated. Fig. 1.11-1 shows the simulation geometry. Estimates indicate that the design goal of 1 mHz in KATRIN's region of interest will be met.

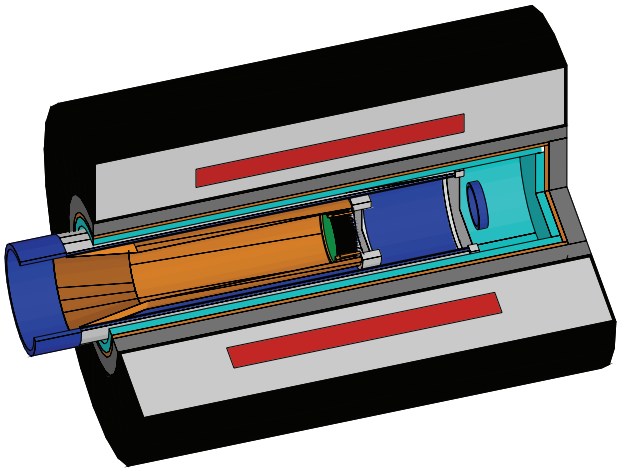

Figure 1.11-1. Drawing of the simulated detector design.

The largest contribution to the detector-related background comes from the feed-through insulators that allow the electronic signals to exit the highest vacuum region. Beta-decay electrons from these insulators are guided by the magnetic fields directly to the detector just like signal electrons. Cleaner materials must be found for these insulators.

Another large contribution is secondaries from cosmic muons. High energy muons pass through the detector leaving energy in the minimum ionizing peak around 120 keV. KATRIN's region of interest will fall between 15 and 50 keV, depending on the post-acceleration setting. In this region the dominant backgrounds from cosmic ray muons are secondary photons produced by interaction in the passive shield of copper and lead. Simulations show this component can be reduced by placing an active shield of plastic scintillator outside the passive shield.

Although the simulation geometry is not an exact replica of the current design, small changes in dimensions are not expected to change background estimates drastically. The electronics will need to be included and verification will be necessary, but the design seems to be within background specifications.

*Presently at Massachusetts Institute of Technology, Building 26-568, 77 Massachusetts Ave, Cambridge, MA 02139.

## 1.12 Electron gun for profiling silicon detectors for KATRIN

T. H. Burritt, P. J. Doe, G. C. Harper, J. A. Mitchell,* B. A. VanDevender, B. L. Wall and J. A. White

The monoenergetic electron source first developed in 2003[1] to profile electron backscattering with respect to incident angle of the large area silicon detectors to be used in the KATRIN experiment was modified in 2005[2] and 2006.[3] It has been modified to accommodate large (10-cm diameter) multi-pixel detectors and to measure the dead layer of these detector arrays. The apparatus uses an electron gun and an einzel lens to produce a tight, focussed electron beam of a few Hz to a few kHz.

Scanning a smaller, 10-mm square PIN diode detector it was found that the beam spot was larger than anticipated by the ion optics program SIMION[4] and, rather than a sharp, 2 mm diameter beam spot there appeared to be a 2 mm core with a halo that extended the beam diameter to 3.5 mm. We are attempting to remedy the problem by the approach shown in Fig. 1.12-1.

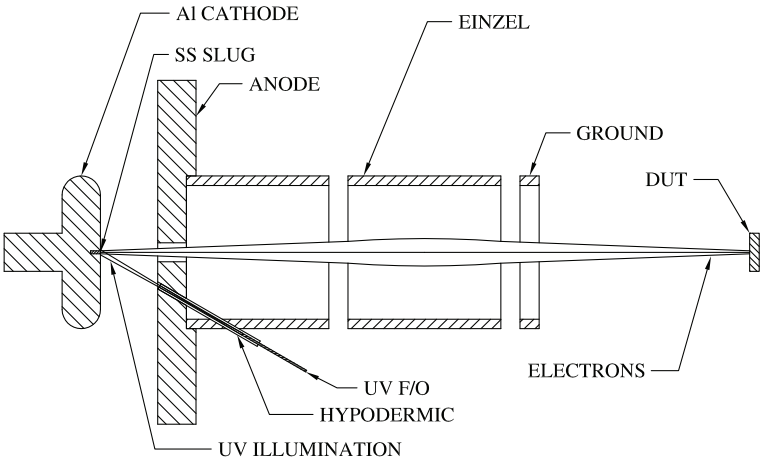


Figure 1.12-1. KATRIN monoenergetic electron gun modified cathode

It is intended that the gun produce low energy electrons by UV photoemission from a stainless steel surface. A UV grade silica fiber and hypodermic needle collimator direct photons from a mercury arc UV lamp onto a 1 mm diameter spot on the cathode emission surface. The electrons are accelerated through a potential that can be varied up to −30 kV. The electron beam is focussed to a spot on the device under test (DUT) 0.6 m from the emission surface by an einzel lens operating at about half of the accelerating potential. We now believe that there is enough internal reflection in the hypodermic needle collimator and scattering from its edges to produce the halo observed. As shown in the figure, the cathode is now made of aluminum with a 0.5-mm diameter slug of stainless steel pressed into the

*Presently at nanoMaterials Discovery Corp, 2121 N 35th St #201, Seattle, WA 98103.

[1]CENPA Annual Report, University of Washington (2003) 65.

[2]CENPA Annual Report, University of Washington (2005) 40.

[3]CENPA Annual Report, University of Washington (2006) 12.

[4]SIMION 3D, version 6.0, David A. Dahl, Idaho National Engineering Lab.

center. The aluminum oxidizes rapidly to form a thin film of $Al_2O_3$. This alumina film has a work function of 11 eV, substantially higher than the work function of stainless steel which is approximately 4 eV. With the UV wavelength used we believe that the electrons will only be emitted from the stainless steel slug. This modification has yet to be tested.

A radiative cooling system was tested on a 10 cm diameter silicon detector wafer made by the Washington Technology Center.[5] Five E-type chromel-constantan thermocouples were used to measure the temperatures of the DUT and the detector cooling ring. We were able to shock-cool the cooling ring to -100° C without damage to the wafer using cold nitrogen vapor produced by forcing gaseous nitrogen through the internal liquid nitrogen dewar which also serves as a vacuum cold trap. The wafer temperature equilibrated at about $-80°$ C uniformly across its surface after about 50 minutes.

New feedthrus were purchased for the recent tests. These include a quad BNC grounded feedthru and a quad E-type thermocouple feedthru. These have been installed, leak tested, and used. The stand for the translation table was rotated by about 2° to compensate for displacement of the electron beam caused by the bottom flange warping when the gun mounting flange was welded to it.

[5]Washington Technology Center, 300 Fluke Hall, Box 352140, Seattle, WA 98195-2140.

## 1.13 Development of an in-situ dead-layer measurement for the KATRIN detector

T. H. Burritt, P. J. Doe, C. Fredericks, H. Gemmeke,* G. C. Harper, M. A. Howe, A. W. Myers, R. G. H. Robertson, M. Steidl,* B. A. VanDevender, T. D. Van Wechel, B. L. Wall, S. Wüstling* and J. F. Wilkerson

In order to develop an in-situ technique to measure the dead-layer thickness of the KATRIN detector, we have measured the dead layer of a CANBERRA[1] 64 pixel PIN diode array using a technique that utilizes a variable energy electron beam. The results obtained using this "energy" method was then compared to the results obtained using the more conventional angle method described in Knoll.[2]

The energy method makes use of the fact that average energy loss in a material is characterized by the Bethe-Bloch function $\frac{dE}{dx}(E_{e^-})$ multiplied by the thickness $t$ of the material. Therefore, energy deposition in a detector can be modeled as the incident energy $E_{e^-}$ less the energy deposited in the dead layer. By varying the energy of incident electrons on a detector, we can compare the incident energy of the electrons with the energy collected in the detector. The plot of energy recorded by the detector (ADC bin) as a function of incident electron energy can be fitted to the equation:

$$E_{deposited} = C * (E - \frac{dE}{dx}T) \tag{1}$$

where C is an ADC bin to energy conversion parameter, $\frac{dE}{dx}$ is the energy dependent Bethe-Bloch function and T is the thickness of the dead-layer. Leaving T and C as free parameters, a value for the dead layer thickness can be obtained.

The dead-layer measurements were conducted in a stainless steel vacuum chamber[3] with an electron gun attached at its base.[4] The CANBERRA PIN diode array was mounted on a X-Y translation stage and a rotary table. This allowed us to change both the beam spot position and the incident angle. Each pixel of the array was connected to a voltage amplifier, the output of which was converted to a digital signal via a VME based ADC shaper card. The data readout was handled by the OS X based ORCA[5] program.

The comparison of the two methods shows an average difference of $10 \pm .3$ nm between them. (See Fig. 1.13-1). The source of this systematic discrepancy between the two methods is currently being investigated. However, even with this discrepancy the agreement between the two methods is sufficient for the energy method to be used in the KATRIN experiment.

*Forschungszentrum Karlsruhe, Postfach 3640, 76021 Karlsruhe, Germany.

[1] CANBERRA, 800 Research Parkway, Meriden, CT 06450. Available: http://www.canberra.com/

[2] G. Knoll, Radiation Detection and Measurement, 3rd ed. Wiley (2000).

[3] CENPA Annual Report, University of Washington (2005) 40.

[4] CENPA Annual Report, University of Washington (2006) 27.

[5] M. A. Howe, G. A. Cox, P. J. Harvey, F. McGirt, K. Rielage, J. F. Wilkerson and J. M. Wouters, Sudbury Neutrino Observatory Neutral Current Detector acquisition software overview, IEEE Transactions on Nuclear Science, 51:878-883 (2004).

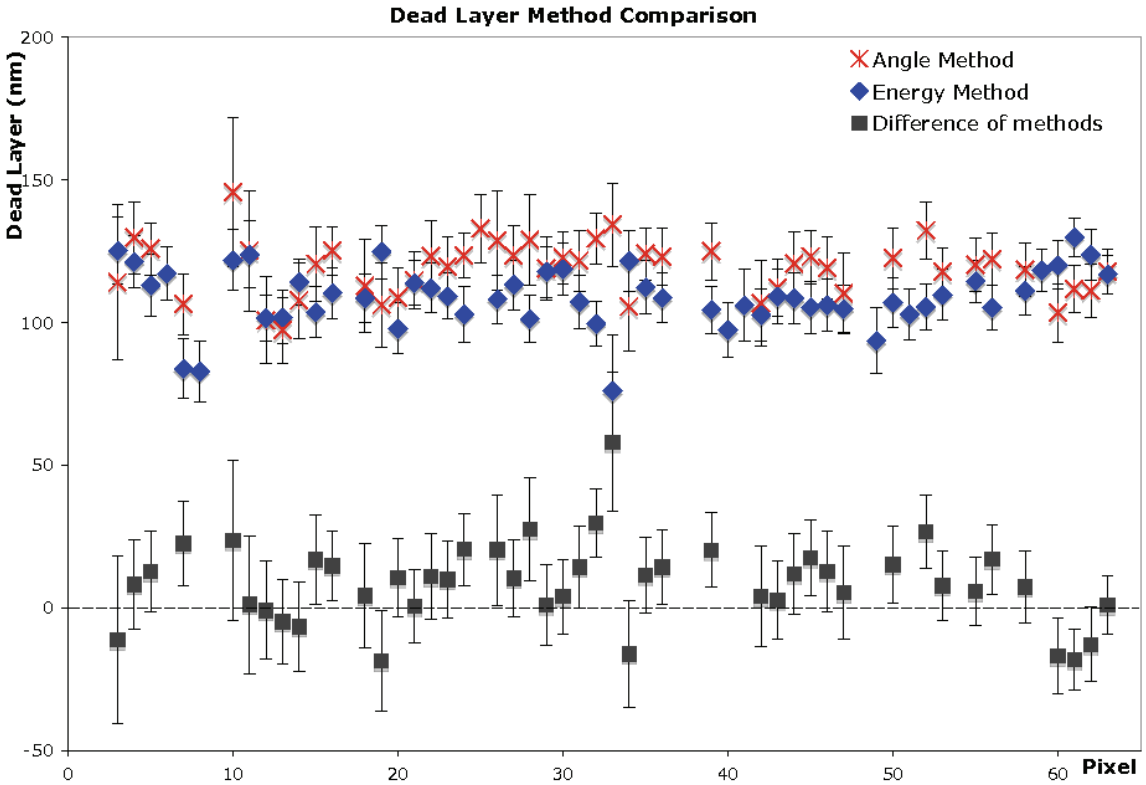


Figure 1.13-1. A comparison of the dead layer thickness of the 64 pixels obtained via the angle and energy methods

# Majorana

## 1.14 The Majorana neutrinoless double-beta decay experiment

J. F. Amsbaugh, J. A. Detwiler, P. Doe, A. García, M. Howe, R. A. Johnson, M. G. Marino, S. McGee, R. G. H. Robertson, A. G. Schubert, B. A. VanDevender and J. F. Wilkerson

Neutrinoless double-beta decay ($0\nu\beta\beta$) provides the physics community with the opportunity to build on our successes in understanding the neutrino and crafting a new standard model. Observation of $0\nu\beta\beta$ would demonstrate that neutrinos are Majorana particles, indicate that Lepton number is not conserved, and provide a measure of the effective Majorana mass of the electron neutrino. For the first time we can mount experiments that probe the neutrino mass region below the upper limits set by direct kinematical searches (tritium) and suggested by observational cosmology, while planning scaled approaches that can address the lower bounds of mass defined by neutrino oscillation experiments. Determining if neutrinos are Dirac or Majorana particles is one of the most important questions facing the physics community today. The Majorana experiment aims to answer this question.

Our proposed method uses the well-established technique of searching for $0\nu\beta\beta$ in high-purity Ge diodes that play both roles of source and detector. The technique is augmented with recent improvements in detector technology, and advances in controlling intrinsic and external backgrounds. Progress in signal processing from segmented and modified-electrode Ge-diode detectors offers significant benefits in rejecting backgrounds, and providing additional handles on both signals and backgrounds through multi-dimensional event reconstruction. Development of sophisticated Cu electroforming methods allow the fabrication of ultra-low-background materials required for the construction of next generation detectors. The Majorana collaboration is directing its efforts toward an R&D phase in which 50-100 kg of high-resolution intrinsic germanium detectors, most of which will be enriched to 86% in $^{76}$Ge, will be deployed in an ultra-low-background electroformed Cu cryostat. This R&D module will be located deep underground within a low-background shielding environment. This effort is aimed at demonstrating that backgrounds can be pushed low enough to justify a future ton-scale $0\nu\beta\beta$ experiment in $^{76}$Ge. The R&D will also address the choice of Ge detector technology, and cost and schedule drivers for a ton-scale experiment. A parallel European experimental effort in $^{76}$Ge $0\nu\beta\beta$ decay, the GERDA experiment, is proceeding with a technique in which bare Ge diodes are immersed in liquid cryogen that shields and cools the crystals but can also potentially be instrumented as a veto. The Majorana and GERDA collaborations have expressed intent to merge collaborations for a ton-scale experiment using the best technology demonstrated in the initial phase. The collaborations openly exchange information, and are cooperating on several fronts including the joint development of a Monte Carlo simulation framework, MaGe. These experiments will either conclusively establish the KKDC[1] claim of double-beta decay, or will significantly improve lifetime limits. A ton-scale experiment in $^{76}$Ge is potentially sensitive enough to address effective Majorana masses over most of the allowed parameter space for an inverted neutrino mass hierarchy. The goals of this effort are consistent with recent recommendations from the *DNP/DPF/DAP/DPB*

[1] H. V. Klapdor-Kleingrothaus *et al.*, Phys. Lett. B **586**, 198 (2004).

*Joint Study on the Future of Neutrino Physics*[2] and the conclusions on $0\nu\beta\beta$ reported by the Neutrino Scientific Assessment Group.

[2] S. J. Freedman and B. Kayser, physics/0411216 (2004).

## 1.15 Surface contamination simulations for the proposed Majorana neutrinoless double-beta decay experiment

J. A. Detwiler, R. A. Johnson, M. G. Marino, A. G. Schubert and J. F. Wilkerson

Previous-generation experiments looking for the neutrinoless double-beta decay($0\nu\beta\beta$) of $^{76}$Ge have set a lower limit on the half-life at $1.9 \times 10^{25}$ years. Next-generation experiments will increase their sensitivity to this very rare decay by substantially lowering signals from radioactive backgrounds. This report summarizes progress on understanding the effects of surface contamination backgrounds for high-purity germanium detectors within the Majorana neutrinoless double-beta decay experiment.

The thin dead layers on the $p^+$ contact of a HPGe crystal detector(typically $\sim 0.3-1.0\mu$m) allows for alpha radiation outside the detector to deposit energy within the active region of the crystal. Typical energies of alpha particles originating from the $^{238}$U and $^{232}$Th decay chains range from $\sim 4-9$ MeV. Depending on how much energy it loses in the dead layer of a crystal an alpha could deposit just enough energy in the active volume to mimic the signal from $0\nu\beta\beta$(2039 keV for $^{76}$Ge). Alpha radiation originating from the surfaces of detectors is therefore a possible source of background.

Surface contamination simulations are performed using MaGe, a C++ based simulation and analysis toolkit developed jointly between the Majorana and GERDA collaborations. The simulations consist of decays of radioactive isotopes on the surfaces of the proposed Majorana neutrinoless double-beta decay experiment. These simulations yield efficiencies for an initial decay to land near the $0\nu\beta\beta$ region of interest energy for $^{76}$Ge(2037-2041 keV). The simulated isotopes include the $^{238}$U and $^{232}$Th decay chains, with particular attention paid to the long-lived radon daughter $^{210}$Po and its 5.3 MeV alpha. Validation of the simulation is being pursued with the "WIPPn" detector. This detector has a distinctive peak at 5.3 MeV corresponding to the alpha from $^{210}$Po(figure Fig. 1.15-1). Further work is planned to incorporate pulse-shape analysis into MaGe. Pulse-shape analysis is expected to allow for higher discrimination of surface events, and is important to be included in a realistic simulation.

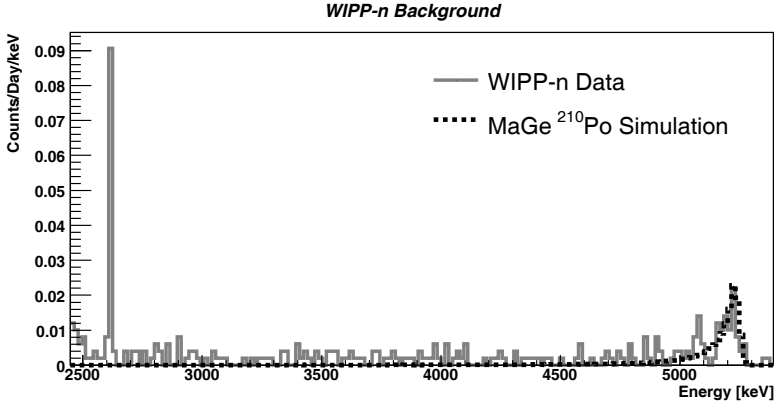


Figure 1.15-1. Comparison of the 5.3 MeV $\alpha$ peak from $^{210}$Po simulation with background data taken from the WIPPn detector.

## 1.16 Validation of cosmic-ray muon-induced physics within the GEANT4-based simulation and analysis package MaGe

J. A. Detwiler, R. A. Johnson, M. G. Marino, A. G. Schubert and J. F. Wilkerson

Understanding the background created by cosmic-ray muon-generated neutrons involves the simulation of their creation, propagation, and interaction with the detector as well as the verification of all associated code. New simulations have been performed modeling two relevant experiments to verify neutron production and propagation in GEANT4.

The NA55 experiment at CERN measured the double differential cross section for neutrons emitted at 45, 90 and 135 degrees from a 190 GeV muon beam incident upon three different materials: graphite, Cu, and Pb.[1] The shapes of the double-differential cross section for both simulation and experiment were compared and found to be roughly in agreement, though this agreement worsens at back-scattering angles (i.e. 135 deg). A comparison of total fluences is given in Table 1.16-1.

Table 1.16-1. Calculated and measured neutron productions for the NA55.

| Material | Exp. Fluence [n/$\mu$/g/cm$^2$] | Calc. Fluence [n/$\mu$/g/cm$^2$] | Ratio |
|---|---|---|---|
| Graphite | $6.8\times10^{-5}$ | $3.3\times10^{-5}$ | 2.1 |
| Copper | $1.2\times10^{-4}$ | $4.8\times10^{-5}$ | 2.5 |
| Lead | $3.5\times10^{-4}$ | $5.9\times10^{-5}$ | 5.9 |

An experiment performed at the Stanford Linear Accelerator Center (SLAC)[2] involved a 28.7 GeV electron beam incident upon an aluminum beam dump. The neutron time-of-flight and energy spectra were measured outside a steel shield and a concrete shield of variable width. A comparison between experiment and GEANT4 simulation indicated an over-attenuation of neutrons within concrete. A correction method was applied to mitigate this discrepancy. These results are presented in Fig. 1.16-1.

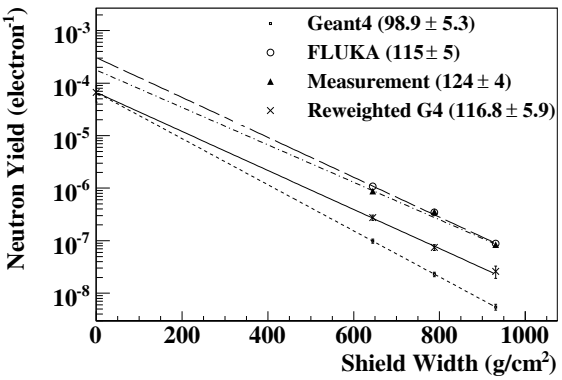


Figure 1.16-1. A comparison of calculated (GEANT4 and FLUKA) and measured total neutron fluence (E$\geq$ 6 MeV) for varying shield width. Exponential fits to all sets of points are included and the values of the characteristic length ($\lambda$) are noted in parentheses in units of g/cm$^2$.

[1] V. Chazal, *et al.* Nucl. Instrum. Methods A **490**, 334 (2002).
[2] S. Taniguchi, *et al.* Nucl. Instrum. Methods A **503**, 606 (2003).

## 1.17 Development of technologies for low-background experiments using the MEGA cryostat

J. A. Detwiler, R. A. Johnson, M. G. Marino, A. G. Schubert and J. F. Wilkerson

Low-background experiments such as those searching for neutrinoless double-beta decay or dark matter demand advances in current technologies to achieve their background goals. The MEGA cryostat is an electroformed-Cu cryostat located underground at the Waste Isolation Pilot Plant (WIPP) in Carlsbad, NM.[1] Work was completed to populate this cryostat with three working high-purity germanium (HPGe) crystals.

To record pulses from a HPGe detector suitable for pulse-shape analysis it is important to place front-end electronics near the detector. Any material placed near the detector creates a potential increase in background. A low-background front-end package (LFEP) has been developed to satisfy the requirements of background and signal readout.[2] Characterization of these LFEPs, including noise measurements and bandwidth determination, were performed. The LFEPs were deployed into the MEGA cryostat along with two new crystals to bring the total crystal population to four.

Tests were performed on the installed crystals including monitoring time required for sufficient cooldown (i.e. through the semi-conductor transition of Ge), measuring operating voltages and reading out pulses. To demonstrate the functionality of the crystals and LFEPs, test data were taken with and without a Th source. Pulses seen and a spectrum from the source run are shown in Fig. 1.17-1 and in Fig. 1.17-2.

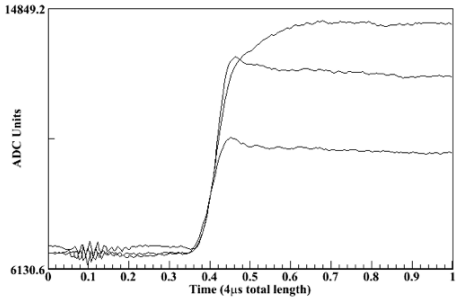


Figure 1.17-1. A triple coincidence from three working detectors in the MEGA cryostat.

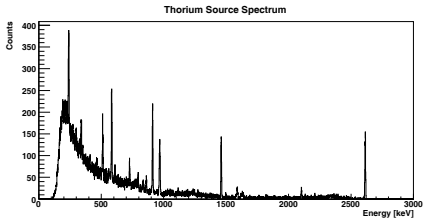


Figure 1.17-2. Spectrum from one channel taken during a Th source run.

[1] K. Kazkaz, *et al.* IEEE Trans. on Nucl. Sci. **51**, 1029 (2004).
[2] T. Hossbach and C. Aalseth, APS Meeting, Maui, HI, Sept 2005.

## 1.18 Low-energy neutron response of germanium detectors in MaGe/GEANT4

J. A. Detwiler, R. A. Johnson, M. G. Marino, A. G. Schubert and J. F. Wilkerson

The Majorana[1] and Gerda[2] collaborations jointly developed MaGe, a GEANT4[3]- and ROOT[4]-based simulation framework. This paper describes a simulation used to study MaGe's ability to model low-energy neutrons in germanium detectors. The simulation was based on an experiment performed at Los Alamos National Laboratory (LANL). Comparison between the simulation results and experimental data can be used to verify MaGe/GEANT4.

During the experiment, energy spectra were collected from each of the four n-type germanium crystals in a Canberra clover detector. The detector was surrounded by lead shielding, and an AmBe neutron and gamma source was located outside of the shield. A slab of polyethylene neutron moderator was placed within the lead shield between the source and detector.

The simulation results were generated with MaGe, using the GEANT4 software package to model the physics processes. ROOT was used to analyze the results. The AmBe source, clover detector, lead shield, and polyethylene moderator were modeled in the simulation.

A comparison between the experimental and simulated results appears in Fig. 1.18-1. The MaGe/GEANT4 package captures many of the features of the experimental energy spectrum. The results of the simulation provide an understanding of the strengths and deficiencies of the MaGe/GEANT4 package.

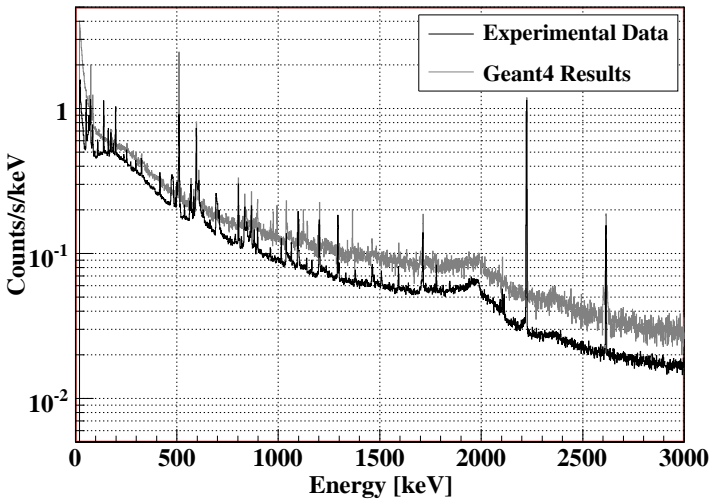


Figure 1.18-1. Comparison between experimental data and simulation results of energy spectra collected by the clover detector.

[1]White Paper on the Majorana Zero-Neutrino Double-Beta Decay Experiment.
[2]The Gerda Collaboration, http://www.mpihd.mpg.de/ge76/gerda_lngssc_mar06.pdf.
[3]S. Agostinelli, *et al.*, GEANT4 - A Simulation Toolkit, Nucl. Instrum. Methods A **506**, 250 (2003).
[4]R. Brun, *et al.*, ROOT - An Object Oriented Data Analysis Framework, Nucl. Instrum. Methods A **389**, 81 (1997).

## 1.19 LArGe, Liquid Argon Compton suppressed Germanium crystal

C. E. Aalseth,* J. F. Amsbaugh, P. J. Doe, J. L. Orrell,* R. G. H. Robertson and J. F. Wilkerson.

We have continued the development of the LArGe apparatus[1] to study background suppression in a high purity germanium crystal diode. The technique uses scintillation light from the surrounding liquid argon (LAr) created when a Compton-scattered gamma-ray escapes the crystal and electron scatters in the LAr. Our effort has been to finish the design and manufacture the new apparatus, which improves the efficiency of the Compton shield by increasing the surrounding LAr from 0.5 to 3 radiation lengths($X_0$).

A pressurized annular liquid nitrogen ($LN_2$) tank near the top of the dewar maintains the LAr in a liquid state. The dewar holds 780 kg of LAr and the $LN_2$ tank volume is 78 l. The crystal can be put in or removed from the LAr by a slide mechanism down the center of the dewar made of low background materials. An airlock is provided so the crystal can be replaced without contamination or loss of LAr. Also, the dewar can be cooled and filled with LAr without the delicate crystal in place. The degraded crystal previously used has been successfully refurbished. The front-end components of the preamplifiers are mounted close to the HPGe to optimize the noise performance.

Four hemispheric 20-cm photomultiplier tubes (PMTs) are mounted in the $LN_2$ tank's inner cylinder with their photocathodes in the LAr. The PMTs bias bases mount outside in air, and a 16-pin feed through assembly connects to each PMT. A blue LED[2] in the bottom provides typical PMT output pulses with $<$ 10-nsec rise time and 25-nsec width comparable to single photoelectron pulses of $<$ 7 nsec and 20 nsec. Three LEDs have been thermally cycled in $LN_2$ 20 times and kept cold for 2 weeks without degradation or failure. The LAr emits scintillation light peaked at 128 nm which is wavelength shifted by a non-metallic visible light reflector, ESR,[3] lining the sides and bottom of the dewar. The reflector was not coated with additional wavelength shifter due to concerns about adhesion, crystal contamination and the fact that the $X_0 = 0.5$ test setup[4] achieved a factor of 2 suppression. Except for the reflector, its support and the LED, all components mount to or hang from the top plate of the dewar. The top plate has lift points and several extra ports for future uses, viewports, et cetera.

Before the initial cooldown and fill, a few external cryogenic lines need to be made and the cold tests of the crystal mechanism and contacts need to be done. The device is illustrated in Fig. 1.19-1.

*Pacific Northwest National Laboratory, Richland, WA 98352.

[1] CENPA Annual Report, University of Washington (2006) 25.

[2] HLMP-CB15-R0xx.

[3] also known as VM2000, from 3M Corp.

[4] J. L. Orrell, C. E. Aalseth, J. F. Amsbaugh, P. J. Doe, T. W. Hossbach, July, 2006, submitted for publication to Nucl. Instrum. Methods A, nucl-ex/0610018.

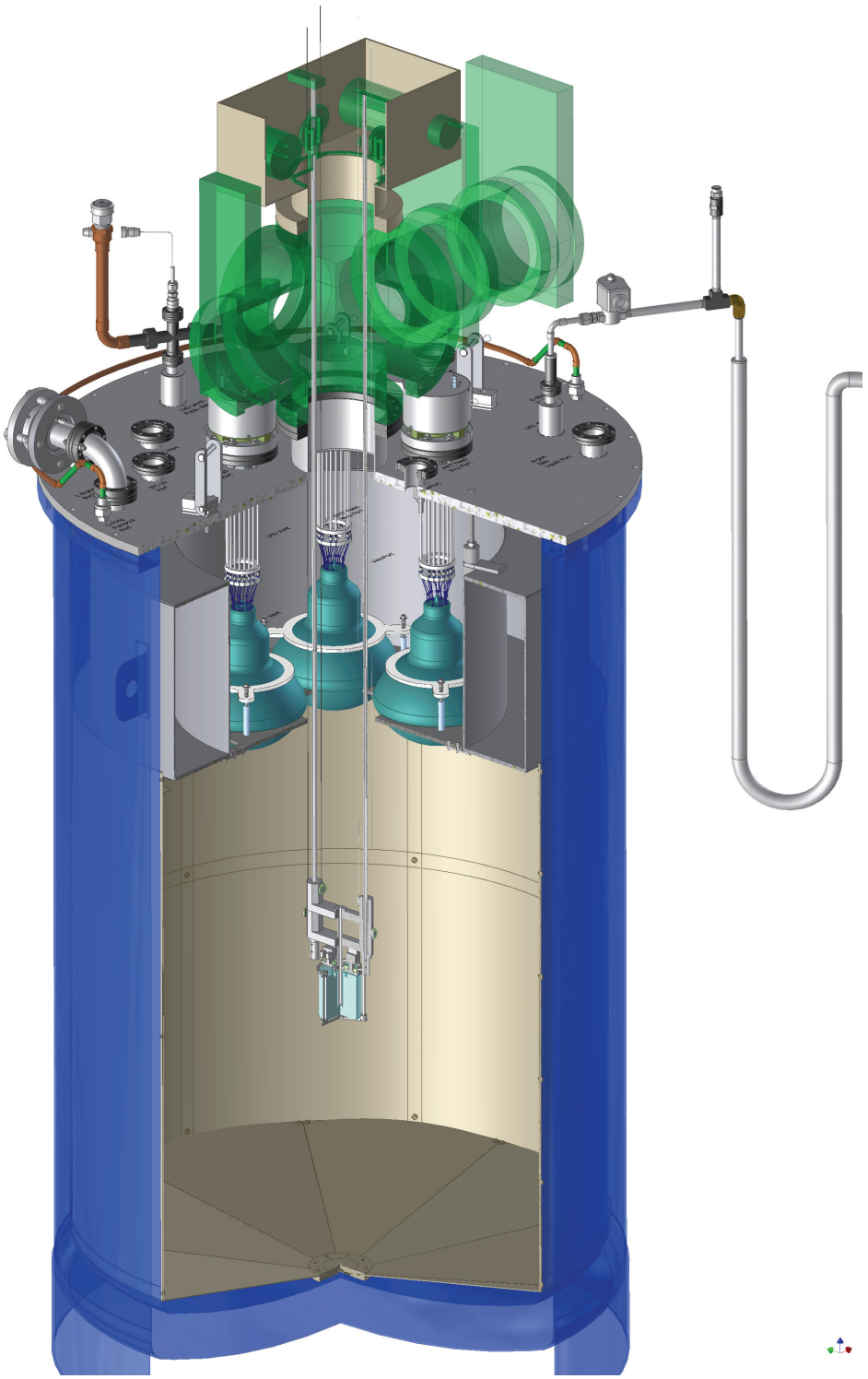

Figure 1.19-1. A three quarters section of second LArGe apparatus revealing the HPGe crystal, track mechanism, $LN_2$tank, PMTs, top manipulator chamber, and air lock.

## 1.20 Design, construction and operation of a small-scale radioactivity assay chamber

J. A. Detwiler, P. J. Doe, R. A. Johnson, W. R. Ketchum,* M. G. Marino, A. S. Reddy,†
A. G. Schubert, B. A. VanDevender and J. F. Wilkerson

A new low-background radiometric assay chamber has been built at CENPA, using two germanium detectors. The chamber should allow us to make initial determinations of the viability of candidate materials for use in low-background experiments (e. g., KATRIN and Majorana). The system will provide a testing ground for many issues relating to germanium detectors, such as detector handling issues, mounting techniques, and cryostat design considerations. The work described in this article was completed by undergraduate students as part of the Research Experience for Undergraduates program.

The two detectors are identical intrinsic germanium detectors manufactured by ORTEC. The active detector volumes are cylinders, 70.9 mm in length and 65.1 mm in diameter. Each of these is contained within an aluminum casing that is attached to a liquid nitrogen cryostat.

The assay chamber consists of both active and passive shielding. Two scintillator paddles actively shield the detector from cosmic rays and any nuclear events associated with them. If energy is deposited simultaneously in both paddles, a trigger is sent to the electronics system to veto any signal that simultaneously occurs in the germanium detectors. Signals occurring in the germanium that are not accompanied by a cosmic veto are read out by the ORCA data-acquisition system. Furthermore, the detectors are housed in a large lead structure to shield background radiation.

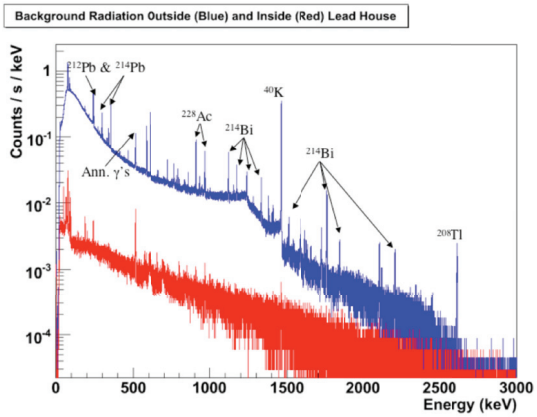


The figure shows a comparison of data taken with a single detector in the absence of a source, with the detector inside and outside of the lead house. In the background spectrum outside of the house, the energy resolution is about 1.0 keV at 1460.8 keV (the $^{40}$K line) and 1.5 keV at 2614.5 keV (the $^{208}$Tl line). We can see that the background is reduced by a factor somewhere between 10 and 100. This reduction could be enhanced by several modifications to the setup. Possible improvements to the shielding include the use of larger, more efficient scintillator paddles, an inner copper metal shield, and N2 gas pumping through the chamber.

*Presently at University of Oklahoma, 660 Parrington Oval, Norman, OK 73019-0390.
†Presently at North Dakota State University, 1301 12th Avenue North, Fargo, North Dakota 58105

# 2 Fundamental Symmetries and Weak Interactions

## Torsion Balance Experiments

### 2.1 Torsion balance search for spin coupled forces

E. G. Adelberger, C. E. Cramer and B. R. Heckel

We use a torsion pendulum containing $9.7 \times 10^{22}$ polarized electron spins to search for feeble long-range interactions that couple to a particle's intrinsic spin. Initial constraints on a coupling between electron spins and a possible Lorentz and CPT-violating background field fixed in space and between electron spins and unpolarized matter in the earth and sun, noted in last year's Annual Report, have recently been published.[1] Interpreted as a constraint on noncommutative geometries,[2] these results place an upper bound of $3 \times 10^{-58}$ $m^2$ (corresponding to an energy scale of $\approx 10^{13}$ GeV) on the minimum observable area in such geometries. Since then, we have eliminated a significant source of systematic error in lab-fixed signals, used the rotation of the earth to measure the pendulum's spin content, and initiated a search for forces coupling two polarized spins together.

The spin pendulum is inside a torsion-balance apparatus that sits on a turntable rotating about a vertical axis at a constant angular velocity. Consequently, its affinity for a preferred direction in space appears as a modulation of its angular position at the rotation frequency. The amplitude of this modulation is itself modulated both daily and annually as the orientation of the fiber axis changes with the earth's rotation and orbit around the sun. We have used these additional modulation frequencies to place tight constraints on couplings to astronomical sources and background fields fixed in space. Couplings to sources fixed in the lab frame are modulated only at the turntable frequency. When analyzing these signals, we found a significant non-zero signal with larger than statistical scatter. The signal can be understood as a gyrocompass effect: the pendulum's net angular momentum from the polarized electron spins couples to the Earth's rotation to produce a steady torque along the fiber axis twisting the spin dipole southward. To investigate the lab-fixed systematic error, we used a dummy pendulum with no significant gravitational moments and no spin dipole. We found a spurious signal associated with the orientation of the dummy pendulum with respect to the damper plates at the fiber attachment point. To eliminate this effect, we have installed a ball-in-cone fiber attachment scheme that allows us to change the angle of the pendulum with respect to the fiber. Tests with the ball-cone and dummy pendulum have shown that any residual systematic effects are unresolvable. With the ball-cone and spin pendulum in place, we have measured the gyrocompass effect and thus determined that the pendulum's angular momentum results from $9.7 \times 10^{22}$ polarized electron spins.

We are currently extending our exploration of spin-coupled forces to effects that depend on the relative orientation of two spins. Such forces could arise from the exchange of axion-like pseudoscalar particles or the Nambu-Goldstone bosons associated with the spontaneous

[1] B.R. Heckel *et al.*, Phys. Rev. Lett. **97**, 021603 (2006).
[2] I. Hinchliffe, N. Kersting and Y. L. Ma, Int. J. Mod. Phys. A**19**, 179 (2004). (hep-ph/0205040).

breaking of Lorentz symmetry. We have constructed kg-scale spin sources using $SmCo_5$ magnets with a soft iron return yoke. These sources are mounted approximately 30 cm from the spin pendulum, outside the torsion-balance apparatus, allowing us to probe interaction with ranges greater than 30 cm. In the coming year, we will construct smaller spin sources that can be placed closer to the pendulum to improve our sensitivity to these interactions at shorter ranges.

## 2.2 Tests of the gravitational inverse-square law below the dark-energy length scale

E. G. Adelberger, T. S. Cook, J. H. Gundlach, B. R. Heckel, C. D. Hoyle,*
D. J. Kapner† and H. E. Swanson

Theoretical speculations about new short-range phenomena arising from "large" extra dimensions,[1,2] more than 1 time dimension,[3] "fat gravitons"[4] and forces from string-theory scalar particles[5] have motivated our interest in studying gravity at the shortest accessible length scales. Furthermore, the measured[6] dark energy density $\rho_{\rm d} \approx 3.8$ keV/cm$^3$ corresponds to a distance $\lambda_{\rm d} = \sqrt[4]{\hbar c/\rho_{\rm d}} \approx 85$ $\mu$m that may represent a fundamental length scale of gravity.[7,8] We have a continuing program of developing instruments that probe the inverse-square law at ever shorter length scales. We recently completed and published[9] our inverse-square law test with the "42-hole" pendulum/attractor system that verified the inverse-square law at Yukawa length-scales down to 56$\mu$m. Our results, along with previous work,[10,11,12,13,14] are shown in Fig. 2.2-1. Our results constrain, at 95% confidence, the size of the largest extra dimension to be less than 44 $\mu$m, and require the dilaton mass to be greater than 3.5 meV. This experiment has essentially reached a practical limit of our "multihole" designs. We are now building two new inverse-square instruments, which are described in Sec. 2.9 and 2.10 of this Report.

*present address: Humboldt State University, One Harpst St., Arcata, CA 95521-8299.
†present address: Kavli Institute for Cosmological Physics, University of Chicago, Chicago IL 60637.
[1] S. R. Beane, Gen. Relativ. Gravit. **29**, 945 (1997).
[2] G. Dvali, G. Gabadadze, M. Kolanović and F. Nitti, Phys. Rev. D **65**, 024031 (2001).
[3] G. Dvali, G. Gabadadze and G. Senjanovíc, hep-ph/9910207 (1999).
[4] R. Sundrum, Phys. Rev. D **69**, 044014 (2004).
[5] E. G. Adelberger, B. R. Heckel and A. E. Nelson, Ann. Rev. Nucl. Part. Sci. **53**, 77 (2003).
[6] C. L. Bennet, *et al.*, Astrophys. J. Supp. Ser. **148**, 1 (2003).
[7] S. R. Beane, Gen. Relativ. Gravit. **29**, 945 (1997).
[8] G. Dvali, G. Gabadadze, M. Kolanović and F. Nitti, Phys. Rev. D **65**, 024031 (2001).
[9] D. J. Kapner, *et al.*, Phys. Rev. Lett. **98** 021101 (2007).
[10] C. D. Hoyle, *et al.*, Phys. Rev. D **70** 042004 (2004).
[11] R. Spero, *et al.*, Phys. Rev. Lett. **44**,1645 (1980); J. K. Hoskins, *et al.*, Phys. Rev. D **32**, 3084 (1985).
[12] J. C. Long, *et al.*, Nature **421**, 922 (2003).
[13] J. Chiaverini, *et al.*, Phys Rev. Lett. **90**, 151101 (2003).
[14] S. J. Smullin, *et al.*, Phys. Rev. D **72**, 122001 (2005).

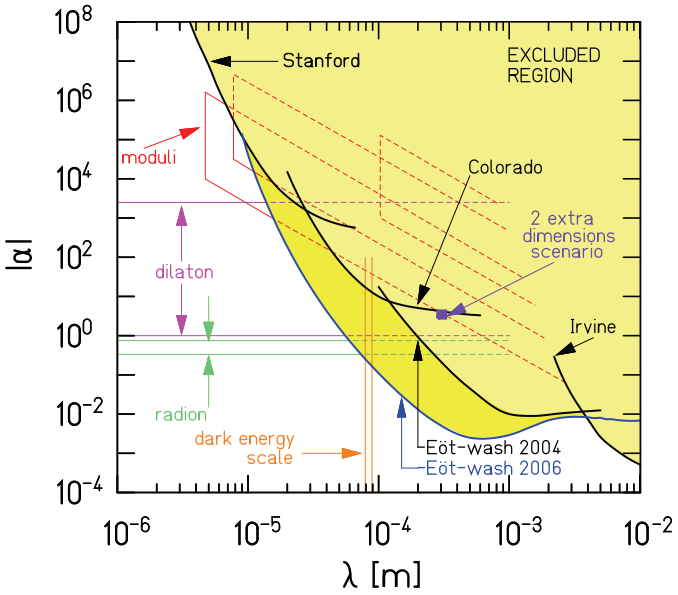


Figure 2.2-1. Constraints on Yukawa violations of the gravitational $1/r^2$ law. The shaded region is excluded at the 95% confidence level. Heavy lines labeled Eöt-Wash 2006, Eöt-Wash 2004, Irvine, Colorado and Stanford show experimental constraints from this work, Ref. 10, Ref. 11, Ref. 12 and Refs. 13 and 14, respectively. Lighter lines show various theoretical expectations summarized in Ref. 5.

## 2.3 Particle physics implications of our recent test of the gravitational inverse square law

E. G. Adelberger, B. R. Heckel, S. Hoedl, C. D. Hoyle,* D. J. Kapner† and A. Upadhye‡

Our recent test of the gravitational inverse-square,[1] summarized in the previous entry of this report, has interesting particle physics implications that were described a second publication.[2] We mention here two of the issues.

1). The PVLAS collaboration[3] studied the propagation of optical photons through a vacuum containing a strong transverse $B$ field and saw an effect they interpreted as evidence for a new spin-zero particle that, through a second-order process, mixes with the photon in a magnetic field. The sign of the observed rotation required the new particle to be a scalar (as opposed to pseudoscalar) boson,[4] and the magnitude required

$$\begin{aligned} 1.0 \text{ meV} &\leq m_\phi c^2 \leq 1.5 \text{ meV} \\ 1.7 \times 10^{-6} \text{ GeV}^{-1} &\leq g_{\phi\gamma\gamma} \leq 5 \times 10^{-6} \text{ GeV}^{-1} \ . \end{aligned} \tag{1}$$

This $\phi\gamma\gamma$ vertex generates, by a 2nd-order electromagnetic process, an effective scalar interaction between two protons, which to leading order is estimated to be[5] $g_S^p/(\sqrt{4\pi\hbar c}) \sim g_{\phi\gamma\gamma}(\alpha/\pi)m_p$ . This force must show up as a violation of the inverse-square law with a range of about 160 $\mu$m. Our limits on such deviations require $g_{\phi\gamma\gamma} \leq 1.6 \times 10^{-17}$ GeV$^{-1}$ , which is inconsistent with Eq. 1 by a factor of $\sim 10^{11}$.

2.) Chameleons, scalar fields that couple to themselves and to matter with gravitational strength,[6] were invented to escape the strong experimental bounds on very light scalar particles. Chameleon exchange leads to an effective potential density[7]

$$V_{\text{eff}}(\phi, \vec{x}) = \frac{1}{2}m_\phi^2\phi^2 + \frac{\gamma}{4!}\phi^4 - \frac{\beta}{M_{\text{Pl}}}\rho(\vec{x})\phi \ , \tag{2}$$

where $\gamma$ characterizes the strength of the self interaction, $\beta$ characterizes the coupling of the scalar field to matter, and $M_{\text{Pl}}$ is the reduced Planck mass. The "natural" values of $\beta$ and $\gamma$ are $\approx 1$. In the presence of matter with density $\rho$, a massless chameleon field acquires an effective mass so that only a small amount of material near the surface contributes to a long-range force.[6,7,8] For $\rho = 10$ g/cm$^2$ and $\beta = \gamma = 1$, this skin thickness is about 60 $\mu$m. Using the method outlined in Ref. 7, we calculated the expected chameleon signal in our apparatus. Our data strongly exclude a substantial region of parameter space around the natural values $\beta \approx 1$ and $\gamma \approx 1$. (See Fig. 2.3-1)

*present address: Humboldt State University, One Harpst St., Arcata, CA 95521-8299.
†present address: Kavli Institute for Cosmological Physics, University of Chicago, Chicago IL 60637.
‡Department of Physics, Princeton University, Princeton, NJ 08544.

[1] D. J. Kapner, *et al.*, Phys. Rev. Lett. **98**, 021101 (2007).
[2] E. G. Adelberger, *et al.*, Phys. Rev. Lett. **98**, 131104 (2007).
[3] E. Zavattini, *et al.*, (PVLAS Collaboration), Phys. Rev. Lett. **96**, 110406 (2006).
[4] E. Zavattini, *et al.*, INFN-LNL-213 (2006).
[5] E. Massó and C. Rizzo, hep-ph/0610286.
[6] J. Khoury and A. Weltman, Phys. Rev. Lett. **93**, 171104 (2004).
[7] A. Upadhye, S. S. Gubser and J. Khoury, hep-ph/0608186 (2006).
[8] B. Feldman and A. E. Nelson, hep-ph/060307.

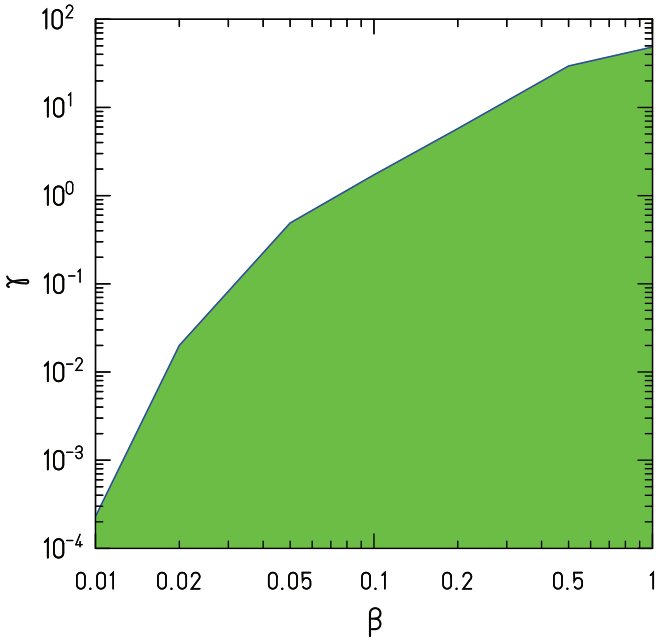


Figure 2.3-1. $2\sigma$ constraints on the chameleon parameter $\beta$ as a function of $\gamma$ from the Kapner *et al.* data. The shaded area is ruled out at 95% confidence.

## 2.4 A new limit on a P- and T-violating force

E. G. Adelberger, B. R. Heckel, H. Hess, S. A. Hoedl and H. E. Swanson

Our torsion pendulum search for an axion-like particle offers a significant improvement over the most recent such measurement.[1] The axion is the result of the hypothesized Peccei-Quinn symmetry and is a favored cold dark matter candidate. Its mass is constrained by the known flat geometry of the universe to be heavier than 1 $\mu$eV, and is constrained by the neutrino flux from SN1987A to be lighter than 10000 $\mu$eV.[2] Note that microwave cavity searches probe for light axions ($m_a \sim 1\mu$eV) and have sufficient sensitivity to see the expected cosmological axion flux.[3] A torsion-pendulum based search is possible because the axion mediates a macroscopic pseudo-scalar potential ($\propto \Theta_{QCD}$) between polarized and unpolarized fermions. By observing the motion of a planar torsion pendulum (source of unpolarized fermions) positioned near the pole faces of an energized ferromagnet, we can observe such a force.

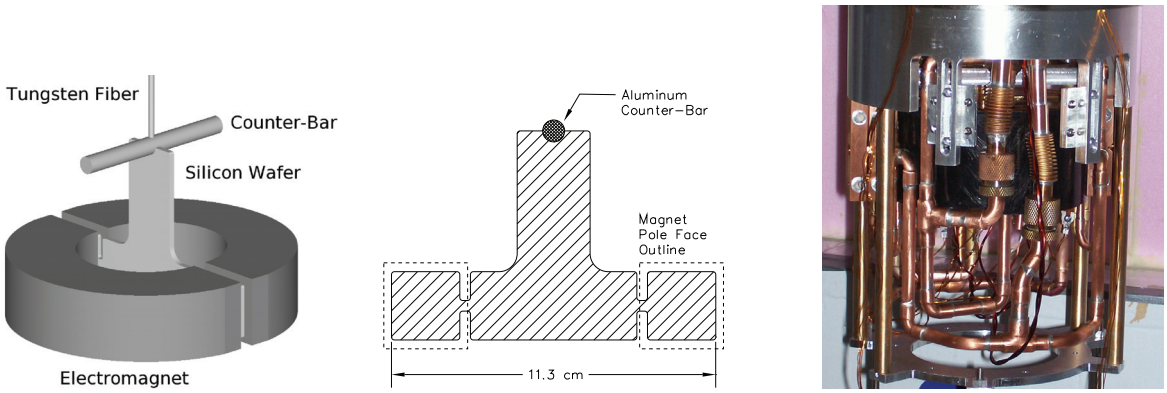


Figure 2.4-1. A scale diagram of one of our pendulums positioned in between the magnet pole faces; A face-on view of the pendulum; A picture of our axion-pendulum apparatus showing the magnet and cooling lines.

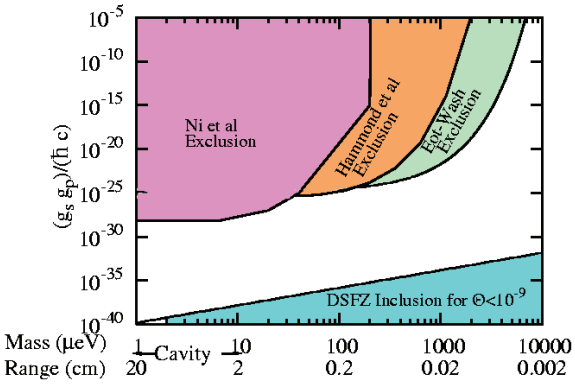


Figure 2.4-2. Our expected exclusion bounds compared with recent experimental searches and the expected coupling for $\Theta_{QCD} < 10^{-9}$.

In the past year, we have completed the construction of our apparatus and tested its performance with two different pendulums. We are presently in the processes of identifying and mitigating systematic errors of the second pendulum design. Once these systematic errors are controlled, we believe the apparatus will be able to put a limit on a macroscopic parity and time violating force which is 100 trillion times more restrictive than Hammond *et al.* for an axion mass of 2 meV, although this is not sensitive to conventional axion models.

[1] G. D. Hammond *et al.*, Phys. Rev. Lett. **98**, 081101 (2007).
[2] G. Raffelt hep-ph/0611350
[3] L. D. Duffy *et al.*, Phys. Rev. D **74**, 012006 (2006).

## 2.5 Laboratory test of Newton's second law in the limit of small accelerations

K.-Y. Choi, J. H. Gundlach, S. Schlamminger and C. D. Spitzer

Newton's second law $F = ma$ is one of the most fundamental equations of classical physics. Its validity at low acceleration scales is generally assumed despite the lack of experimental tests. Interest in violations of $F = ma$ for low accelerations has been spurred by Milgrom[1] in 1983. He proposed a change of Newton's second law to explain the observed flatness of galactic rotation curves. In this so-called **MO**dified **N**ewtonian **D**ynamics (MOND), Newton's second law becomes $F = ma^2/a_0$ for accelerations of $a << a_0$. Newton's second law is recovered in case of $a > a_0$. Milgrom showed that with $a_0 = 1.2 \times 10^{-10}$ ms$^{-2}$ a reasonable fit to the observed rotation curves for many galaxies could be achieved. Other observations accentuate the need to test Newton's second law at small accelerations. The Pioneer spacecrafts 10 and 11 exhibit an unmodeled acceleration of $a_P = 9 \times 10^{-10}$ ms$^{-2}$ towards the sun at distances larger than 15 AU, and the Hubble acceleration, given as a product of the speed of light and the Hubble constant, is $a_H = 7 \times 10^{-10}$ ms$^{-2}$.

We used a torsion balance to test Newton's second law for small acceleration. At small excursions from its equilibrium position a torsion pendulum is subject to small accelerations. Consequently, the validity of Newton's second law can be tested by measuring the natural frequency of a torsion pendulum as a function of its amplitude. A violation of $F = ma$, similar to the one proposed by Milgrom, would lead to an increase of the natural frequency for smaller amplitudes.

Fig. 2.5-1 shows the acceleration averaged over the active pendulum as a function of force derived from Hooke's law.

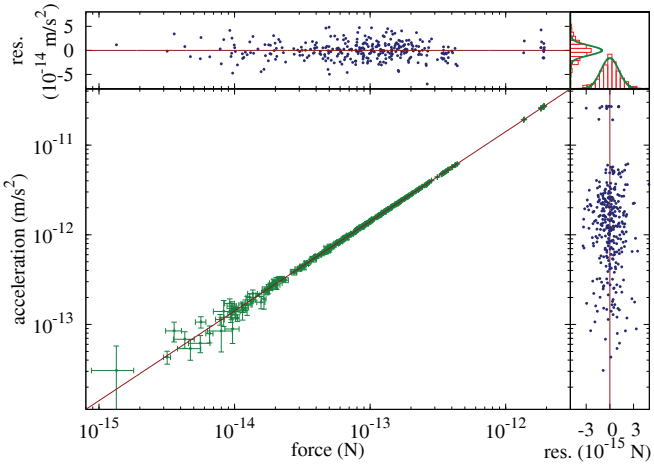


Figure 2.5-1. The measured acceleration as a function of force. The right and top panels show the residuals.

We find the data to be in good agreement with Newton's second law down to accelerations as small as $5 \times 10^{-14}$ ms$^{-2}$. This is three orders of magnitude smaller than a previous experiment.[2]

MOND requires accelerations in all dimensions to be small, a condition which cannot be found on Earth, and hence our test does not directly constrain MOND. However, our test sets constraints on any theoretical formalism by requiring it to reproduce our result.

[1] M. Milgrom, Astrophys. J. **270**, 365 (1983).
[2] A. Abramovici and Z. Vager, Phys. Rev. D **34**, 3240 (1986).

## 2.6 Rotating torsion balance test of the weak equivalence principle for beryllium and titanium

E. G. Adelberger, K.-Y. Choi, J. H. Gundlach, S. Schlamminger and T. A. Wagner

The equivalence of gravitational and inertial mass exists as a fundamental assumption in General Relativity. However, attempts to create a theory including both gravity and the standard model typically violate the equivalence principle.[1] To test the equivalence principle, we used a rotating torsion balance to measure the differential acceleration between different composition test masses. The test masses were arranged in a dipole configuration on the pendulum, so that a signal would occur at the rotation frequency of the apparatus. We measured the difference in acceleration for beryllium and titanium to the North $\Delta a_{N,Be-Ti} = (-0.8 \pm 3.0) \times 10^{-15}$ ms$^{-2}$ and to the West $\Delta a_{W,Be-Ti} = (-1.3 \pm 3.4) \times 10^{-15}$ ms$^{-2}$. We are now repeating our measurement with beryllium and aluminum test masses.

By analyzing our measurement with respect to different sources, we set limits on the violation of the equivalence principle at ranges from one meter to infinity. Using our earth fixed result, we constrain the parameter $\eta_{Be-Ti} = \Delta a/a = (0.35 \pm 1.31) \times 10^{-13}$. The galaxy provides an additional interesting source, since approximately one quarter of the total acceleration of the solar system toward the center of the galaxy is caused by dark matter.[2] We find no difference in the acceleration due to dark matter between beryllium and titanium, giving $\eta_{DM,Be-Ti} = (0 \pm 6) \times 10^{-5}$.

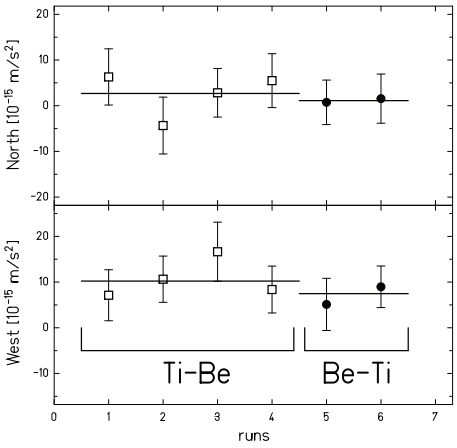


Figure 2.6-1. The two components of the measured acceleration, corrected for tilt and gravity gradients, with respect to a zero mark on the pendulum frame. A violation of the equivalence principle would appear as a difference in the means (lines) of the two data sets.

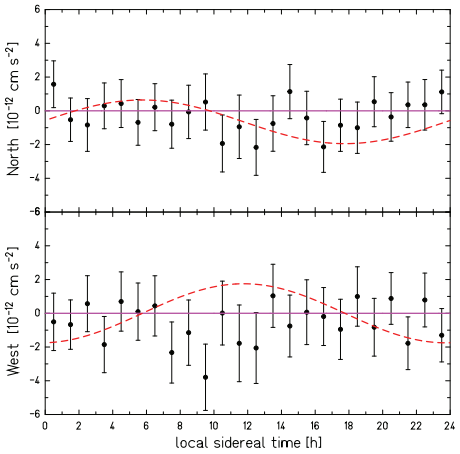


Figure 2.6-2. The averaged acceleration in the North and West direction as a function of sidereal time. The dashed line represents a space fixed hypothetical signal of $20 \times 10^{-15}$ ms$^{-2}$. The solid line is the best fit of $\Delta a = (0.0 \pm 3.0) \times 10^{-15}$ ms$^{-2}$.

[1] T. Damour, Class. Quantum Grav. **13**, A33 (1996).
[2] G. L. Smith, *et al.*, Phys. Rev. D **61**, 22001 (2000).

## 2.7 Development of a pendulum to test short range spin-spin interactions

E. G. Adelberger, B. R. Heckel and W. Terrano

Spin-0 Goldstone bosons generically produce new spin-coupled forces[1,2] that would not be observable between ordinary, unpolarized bodies.[3] Several torsion pendulums designed to investigate such interactions are already in operation.[4] We have been developing a new design that is specifically optimized to study spin-spin interactions between electron spins for ranges down to a millimeter.

To this end, we will build a 10-fold symmetric pendulum of alternating high (Alnico) and low ($SmCo_5$) spin density wedges as illustrated in Fig. 2.7-1. By carefully matching the magnetizations, we can build a complete magnetic circuit, so that the magnetic flux is contained within the ring to minimize spurious magnetic forces. Using a similarly constructed ring as an attractor, we will operate at separations of around 1 cm. This will allow us to look at relatively short range forces compared to earlier experiments. Even for infinite range forces, the advantageous geometry should allow us to improve on the current experimental limits for the couplings of new forces by four orders of magnitude, since dipole-dipole interactions typically have a $1/r^3$ potential.

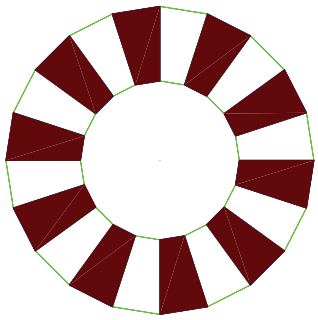

Figure 2.7-1. Drawing of 10 fold symmetric pendulum plate. Dark regions correspond to high spin content, (Alnico) and light regions correspond to low spin content($SmCo_5$).

[1] J. E. Moody and F. Wilczek, Phys. Rev. D **30**, 130 (1984).
[2] N. Arkani-Hamed, H. C. Cheng, M. Luty and J. Thaler, arXiv:hep-ph 0407034.
[3] D. Chang, R. N. Mohaputra, and S. Nussinov, Phys. Rev. Lett. **55**, 2835 (1985).
[4] CENPA Annual University of Washington (2006) 21.

## 2.8 Continued progress toward improved torsion fibers

J. H. Gundlach, C. A. Hagedorn, S. E. Pollack and S. Schlamminger

The thermal torque noise present in any torsion balance represents a fundamental limit of its sensitivity. The noise is proportional to $\sqrt{\kappa/Q}$, where $\kappa$ is the fiber's torsion constant, and $Q$ is its mechanical quality factor. Thus, in an effort to minimize this parameter we continue our investigation of the properties of different torsion fiber materials. We have examined quartz, fused silica, metallized silica and quartz, tungsten, annealed tungsten, and carbon fibers.

In the past year, we have improved our measurement technique, observed the effect of gas pressure on the $Q$ of our torsion pendulum, observed the amplitude dependence of $Q$ in tungsten fibers, characterized the effect of annealing tungsten on $Q$ and breaking strength (our fibers' breaking strength decreases with annealing), tested very high tensile strength carbon fibers, and begun exploring the possibility of laser-drawing quartz fibers. In addition, we have gained further experience in depositing thin chromium coatings onto our quartz fibers, finding that 1–2 nm coatings seem to be thinnest coatings we can utilize while maintaining measurable conductivity along the length of the fiber. The carbon fibers we have investigated have exceptionally high strength and small torsion constants but also have comparatively small $Q$s.

More recently, we have undertaken a careful assessment of the properties of the 13-$\mu$m tungsten fiber used in our LISA test apparatus. By cautiously annealing the fiber to successively higher temperatures, we have been able to develop a far greater understanding of the interrelationship between $Q$ and annealing temperature. This knowledge has been put to use in the LISA balance itself. In addition, we found that the ambient magnetic field in the apparatus must be controlled and minimized in order to reach superior $Q$s.

In the future, we intend to put an uncoated quartz fiber into the LISA apparatus to test charge management techniques. If charge management proves successful, we expect to focus our efforts on improved fiber fabrication techniques to manufacture very uniform bare quartz fibers. We will continue our investigation of tungsten and continue to explore the exotica such as carbon and other fibers.

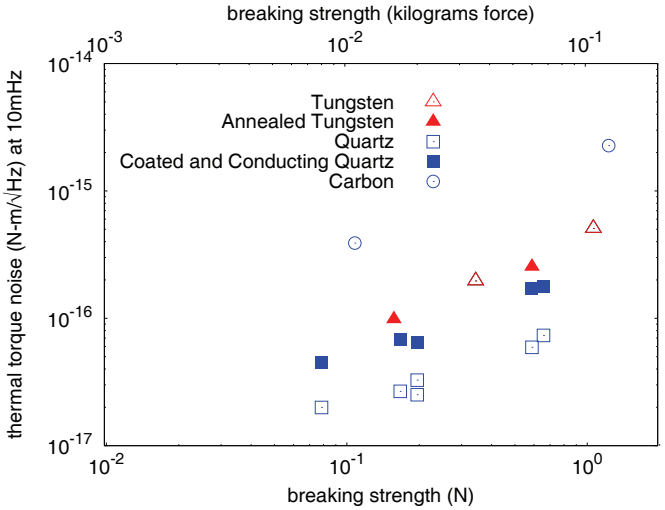


Figure 2.8-1. Graphical summary of our $Q$ studies. All fibers were between 10 and 50 cm long.

## 2.9 New short range test of Gauss' law for gravity

J. H. Gundlach, C. A. Hagedorn, K. K. Krause, S. E. Pollack and S. Schlamminger

We have begun the construction of a new experiment designed to test Newton's inverse square law of gravitation at length scales less than 100 microns. In contrast to our group's current inverse square law test, the new experiment will utilize a parallel plate geometry that enables a nearly-null test of the inverse square law over its full range of operation.

Our experiment hinges on the fact that, if Newton's law/Gauss' law holds, the gravitational field of an infinite sheet of matter is uniform. We will use our torsion balance to compare the strength of the gravitational field at different separations from an "infinite" sheet. The field mass and the torsion pendulum will be physically and electrically isolated by a thin tightly-stretched metal membrane.

The heart of our apparatus will consist of a "step pendulum" constructed from titanium sheet with platinum inlays and an "infinite sheet" attractor constructed from a titanium sheet with a platinum foil attached to its front face. We can better approximate the gravitational field of an infinite sheet of mass through the addition of a rim on the attractor's backing sheet. We will move the attractor toward and away from the pendulum on a flexure translation stage fabricated by the Physics shop and characterize its motion with a capacitance bridge whose development is nearly complete. The thin foil that isolates the pendulum from the attractor will be held by a drumhead-like stretching apparatus. The twist of the pendulum will be read via an autocollimator and the pendulum controlled by electrostatic feedback. The entire torsion balance will be enclosed in a 42"×30" diameter vacuum bell jar to minimize gas effects and improve thermal isolation. The entire apparatus will be placed in an insulating enclosure and precautions will be taken to keep the apparatus free of dust. The instrument is designed to be sensitive to violations of the inverse square law at distances as small as 20 microns at gravitational strength.

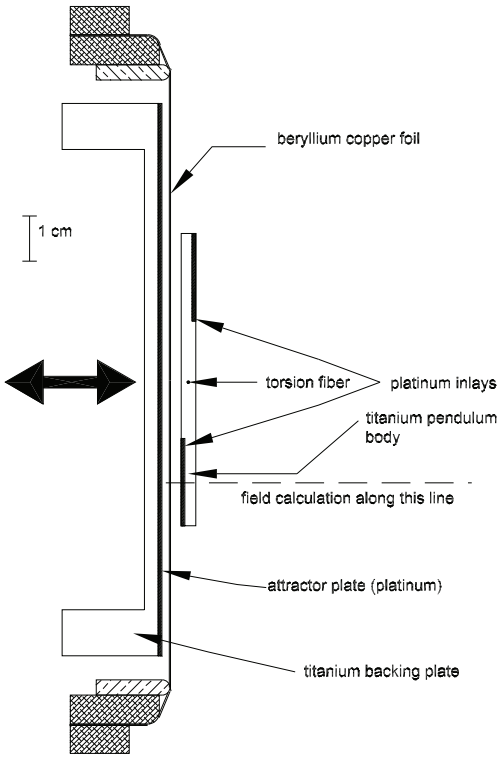


Figure 2.9-1. Diagram of the heart of our apparatus. The horizontal scale is exaggerated to highlight key features.

Our new test is complementary to the experiment presently underway, as the experiments respond differently to many systematic effects. The parallel-plate geometry is fairly insensitive to measurement errors in many critical experimental parameters. In addition, a simple variation of this experiment will allow us to set stringent new limits on inverse square law violations at ranges from millimeters to centimeters.

## 2.10 Wedge Pendulum: A new test of the gravitational inverse-square law

E. G. Adelberger, T. S. Cook, B. R. Heckel, C. D. Hoyle,* D. J. Kapner† and H. E. Swanson

The Wedge Pendulum[1] we have been developing for the last nine months is nearly ready to take data. The development has involved many technologies that are new to us, and as such this has been a time of much trial and error.

One of the critical technologies to be mastered was glueing the pendulum foil to its substrate. We require an adhesive that provides structural stability, good vacuum properties, produces a final pendulum that is flat and "well behaved." In other words, the glue cannot creep or squish into the open spaces of the wedges as this would create headaches for computationally modeling the system. Our current solution is to use Dow Integral E100 adhesive film. This product has shown to meet the above requirements when cured in a well controlled environment. We purchased a digitally controlled vacuum oven to ensure process control for the glueing.

The other focus of development has been on an improved turntable for our attractor. We have built a new bearing assembly that includes a high resolution optical angle encoder and an on-board drive motor. This system will allow us to monitor the attractor angle to far greater precision than ever before as well as to feedback our drive system for more constant rotation. The motor we are currently testing employs piezo electrics to provide the rotation torque and is therefore free of any magnets. It is also vacuum compatible. Driving this motor in a smooth manner is the challenge we are currently tackling.

We hope to clear the final technological hurdles in constructing our instrument and should enter the data taking phase in a few months.

*Presently at Humboldt State University, Arcata CA, 95521
†Presently at Kavli Institute for Cosmological Physics, University of Chicago, Chicago IL, 60637
[1]Nuclear Physics Laboratory Annual Report, University of Washington (2006) 32.

## 2.11 Investigations of small thermal gradient and electrostatic effects for LISA*

J. H. Gundlach, C. A. Hagedorn, S. E. Pollack and S. Schlamminger

We are investigating small forces between closely spaced conducting surfaces for the Laser Interferometer Space Antenna (LISA).[1] Fluctuations in the thermal gradient across each of the LISA electrode housings and proof masses cause fluctuations in the differential radiation pressure on the proof masses as well as fluctuations in the differential outgassing rates of the proof masses and housings. In addition, variations in the radiometer effect due to thermal gradient fluctuations contribute to acceleration noise of the proof mass limiting LISA's low frequency sensitivity to gravitational waves. Using heaters embedded in our split copper plate[2] we have measured the thermal-to-torque transfer function which is a proxy for the amount of acceleration noise expected from these thermal gradient effects. Our results were presented at the recent Sixth International LISA Symposium and have been published in the proceedings from that meeting.

The electrode housings and the proof masses of LISA form a collection of capacitors used in position determination for the drag-free operation of each satellite. Fluctuations in the electric potential between the proof masses and each of the electrodes will lead to acceleration disturbances of the proof masses which again hinder the low frequency sensitivity. We measure the electric surface potential difference between our pendulum and split copper plate by varying the electric potential on the copper plate and measuring the induced torque change on the pendulum. Some of our more recent results are shown in the figure below. We are in the process of refining our measurement procedure to reduce the apparent measurement noise and reach the LISA goal of $10\,\mu\mathrm{V}/\sqrt{\mathrm{Hz}}$ above 0.1 mHz.

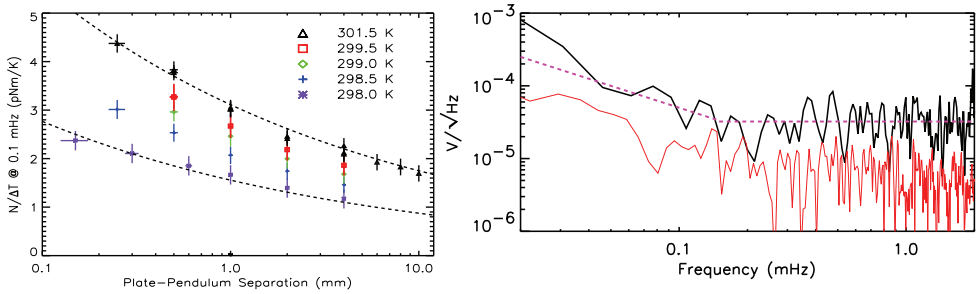


Figure 2.11-1. **Left:** Thermal-to-torque transfer function at 0.1 mHz as a function of the separation between the copper plate and pendulum. Data at a variety of mean plate temperatures are shown. The dashed lines are power laws of $d^{-1/4}$. The distance dependence appears to follow this power law independent of the mean plate temperature.
**Right:** Measured surface potential fluctuations using the method described in the text. The red (thin) trace is the voltage noise on the split copper plate measured electronically. The dashed fit rises as $1/f$ below 0.1 mHz and has a level of $30\,\mu\mathrm{V}/\sqrt{\mathrm{Hz}}$.

*Not supported by DOE CENPA grant.

[1] http://lisa.jpl.nasa.gov

[2] S. E. Pollack, S. Schlamminger, and J. H. Gundlach, AIP Conference Proceedings 873, New York (2006) 158.

## 2.12 Initial results from the APOLLO lunar-laser ranging experiment*

E. G. Adelberger, C. D. Hoyle,† H. E. Swanson and the APOLLO collaboration

Fundamental properties of gravity, including the Strong Equivalence Principle and $\dot{G}/G$, are best probed by the shape of the lunar orbit. The APOLLO (Apache POint Lunar Laser-ranging Operation)[1] project will measure this shape with unprecedented precision by detecting pulsed laser light (532 nm) returned from retroreflectors on the lunar surface. We aim for an order of magnitude improvement upon current measurements that characterize the lunar orbit at the 4 mm level.[2] During the last year we have had much success in pursuing this goal.

Since our last report[3] we have successfully performed differential measurements of the round-trip travel time of photons sent from the observatory to the lunar retroreflectors as compared to those returned from a corner cube mounted on the telescope itself. We have effectively received returns from all four functioning lunar retroreflector arrays as summarized in Table 2.12-1. With this data we calculated the lunar distance for many separate observing runs and created "normal points" that we compare to a model of the lunar orbit created at the Jet Propulsion Laboratory (JPL). We have achieved our goal of a one-way distance uncertainty of one millimeter for several normal points, which are taken over a large portion of the lunar cycle.

| Lunar Retroreflector | Number of Photons | Number of Normal Points |
|---|---|---|
| APOLLO 11 | 4429 | 12 |
| APOLLO 14 | 1771 | 8 |
| APOLLO 15 | 21945 | 28 |
| Lunokhod 2 | 102 | 2 |
| Total | 28247 | 50 |

Table 2.12-1. APOLLO results from the period April 2006 - January 2007. During this period we had 71 observing sessions (24 others were canceled due to weather). We observed as many as nine lunar returns in a single pulse as well as a peak rate of roughly 0.8 photons/pulse. We see a sustained rate on APOLLO 15 of about 0.35 photons/pulse and have acquired all four retroreflectors in a single observing session. Note that the rate discrepancy can be explained because the APOLLO 15 array is larger than the others.

Other improvements over the last year include many software and hardware upgrades. In addition, our laser was professionally serviced in June, 2006 and is performing at a much improved level as far as power level and dropouts are concerned.

A full analysis to search for new physics based on the orbit shape determined from the normal points is currently underway. In the upcoming months we plan to investigate systematic effects and refine our analysis techniques to obtain first publication-quality results.

*Not supported by DOE CENPA grant

†Present address: Humboldt State University, One Harpst St., Arcata, CA 95521-8299.

[1] T. W. Murphy, *et al.*, Nucl. Phys. B, **134**, 155 (2004).
[2] J. G. Williams, S. G. Turyshev, and D. H. Boggs, Phys. Rev. Lett., **93**, 261101 (2004).
[3] CENPA Annual Report, University of Washington (2006) 37.

## Weak Interactions

### 2.13 NSAC - the data acquisition and control system for the parity non-conserving neutron spin rotation experiment

H. E. Swanson

Neutron-spin angle rotations resulting from passing through material in the target region of the polarimeter apparatus are measured as described in previous annual reports.[1] NSAC is the data acquisition program written at CENPA used to control magnetic fields, position targets in the neutron beam, and acquire data. This all happens according to a preprogrammed sequence loaded into the program. Neutrons exiting the polarimeter are detected in a $^3$He ion chamber. For each polarimeter configuration, the ion chamber currents are integrated and digitized. These currents giving the neutron flux along with the configuration information constitute the raw data for the experiment, which are saved to a disk file. At the end of each sequence, parity non-conserving neutron-spin angles and many other diagnostic quantities are calculated and their mean values over the run and standard deviations displayed. The sequence is continuously repeated until the run is ended by the experimenter. Plots of the data analysis results from each completed sequence are displayed by selecting from a new drop down menu of analysis monitors. Other additions to the program are as follows:

Neutron-spin angles calculated from the asymmetry in neutron flux between the two polarities of output coil currents are shown in real time for the East and West sides of the experiment. The displays show running mean values since last reset and are useful in aligning the vertical axes of the precession fields.

A stand alone version of the NSAC program is now available that reads data files taken at NIST and displays raw data and data analysis plots. It also generates simulated neutron data which is useful in learning to use the program. This is available as a self extracting file that installs on any MS Windows computer.

After the completion of each run, data files are uploaded to a secure server at CENPA where they are available to all members of the collaboration.

Currently a room temperature target insert is being used to checkout the operation of the polarimeter prior to installation of the cryogenic target. A new control subroutine was added to NSAC for this target.

The program can now determine the polarization product of the polarizer-analyzer pair. The sequencer requests user input for various tilts of the input coil and measures the resulting changes in spin angle. A file showing the calculated polarization products for each data channel is then written.

[1] CENPA Annual Report, University of Washington (2004) 1.

## 2.14 Parity non-conserving neutron spin rotation experiment

C. Bass,* K. Gan,† B. R. Heckel, D. Luo,* D. Markoff,‡ A. Micherdzinska,* H. P. Mumm,§ J. Nico,§ A. Opper,† W. M. Snow* and H. E. Swanson

The cryogenic target has successfully completed cool down tests at Indiana University. Liquid helium hold time is about 2.5 days. Liquid helium has been moved between target chambers using an externally applied differential pressure. In addition earlier problems with the centrifugal pump seizing up at liquid nitrogen temperatures were fixed by increasing clearances. Delivery is expected at NIST in June 2007.

In the initial testing of the neutron detector we used an empty insert filled with Helium gas and acquired data with our data acquisition system. To further test the sequencing part of the system we built a room temperature target insert from unused parts of the previous spin rotation apparatus. Certain materials e.g. Lanthanum, Tin, and Bromine are known to have large parity odd spin rotation effects. The idea is to measure the neutron's spin angle rotation in passing through targets made of these materials. Pneumatic pistons that shuttle the targets from side to side are located near the center of the old Liquid Helium target positions and thus the scattering geometry is similar. Moving these targets between positions is analogous to pumping the liquid Helium between chambers in the cryogenic target. In the case of liquids such as the Bromine compound, thin walled aluminum boxes containing quartz vials would be used. We achieve statistical significance in about a weeks running with these targets and the measurement could be part of a dissertation for one of the students. The apparatus, except for the cryogenic target insert, was installed on the beam line in 2006, and we have been successfully taking data with the room temperature target since installation.

A coil wound around the outer magnetic shield is used in a feedback loop with an internal fluxgate magnetometer to maintain the axial field in the target region below few micro Gauss.

In all our measurements to date we observe systematic contributions to the PNC observables consistent with attenuation differences in the two targets. We suspect leakage fields from a damaged input coil result in small precessions of the spin from vertical that are dependent on the neutron's position within the beam and its wavelength. We measure a dependence of the neutron-spin angle on wavelength and also see a difference in flux attenuation by the targets for different wavelengths. For lanthanum and tin the Bragg edge is within the wavelength distribution of the beam and we see these scattering effects. For the other targets the attenuation we observe is inversely proportional to the neutron's velocity as expected.

Currently we are investigating the input coil problems and intend to correct them before taking more data with neutrons.

*Department of Physics, Indiana University Cyclotron Facility, 2401 Milo B. Sampson Lane, Bloomington, IN 47408.

†The George Washington University, Department of Physics, Corcoran 105, 725 21st St, NW, Washington, DC 20052.

‡Triangle Universities Nuclear Laboratory, Duke University, TUNL Building, Science Drive, Room 414, P.O. Box 90308, Durham, NC, 27708.

§NIST Center for Neutron Research, 100 Bureau Drive, Stop 8461, Gaithersburg, MD 20899-8461.

## 2.15 Nuclear reactions of $^{32}$Ar in Si

E. G. Adelberger, M. Bhattacharya,* A. García, D. Melconian and S. Triambak

As described in an earlier report,[1] the $ft$ value of the $0^+ \rightarrow 0^+$ $\beta$-delayed proton decay of $T = 2$ $^{32}$Ar can be used to test isospin symmetry-breaking calculations needed to extract $V_{ud}$ from nuclear $\beta$ decay. The experiment involved stopping $\approx 53$ MeV/u $^{32}$Ar ions in a Si detector, after passing through 1.07 mm of Si and 310 $\mu$m of aluminum. One of the systematics contributing to the uncertainty in the $ft$ measurement was due to the possibility that the Ar ion underwent a transmuting nuclear reaction before stopping in the Si detector. In that case, we might mis-identify the event as a good $^{32}$Ar.

Good agreement (to within 10%) between models is seen when calculating the total reaction cross section, and we are confident that 1.5% of the incoming $^{32}$Ar ions should react before stopping. The difficulty is that our system discriminates against some reaction channels but not against others. For example, if $^{32}\text{Ar} \rightarrow {}^{31}\text{Cl} + p$, then the proton would have enough energy to penetrate the implantation detector and register in a following ("4$^{\text{th}}$") Si detector which would veto the event. If, however, the reaction involved a neutral particle, like $^{32}\text{Ar} \rightarrow {}^{31}\text{Ar} + n$, then it would not leave energy in the 4$^{\text{th}}$ detector and so would not be vetoed. It is therefore important to know the *partial* cross sections, which are much harder to calculate.

Indeed, very little agreement is seen between the models in this case. However, we have shown that we can reasonably reproduce both the magnitude and shape of the energy spectrum in the 4$^{\text{th}}$ detector in our simulations since qualitatively all heavy charged decay products produce a similar signal. Furthermore, by comparing the calculated branching ratio with different cuts on the event selection, we also found reasonable agreement between data and simulation in the estimated fraction of reacted events.

We estimate the systematic on the $ft$ measurement by considering the various partial cross section values which still reproduce the energy spectrum of the 4$^{\text{th}}$ detector. This resulted in a 0.2% change in the number of incoming ions that are still $^{32}$Ar when stopped in the implantation detector. We assume 100% uncertainty in this value to be conservative considering the wild variations in predictions of the partial cross sections. The result is a 0.20% uncertainty in the $ft$ value, which is on par with the uncertainty in the number of proton decays observed. Both of these are currently below the 0.4% uncertainty due to the efficiency of the HPGe detector; however, the $^{32}$Cl experiment (see Sec. 4.2 and 4.3) will provide a better *in situ* calibration and make this uncertainty negligible.

*Present address: Brookhaven National Lab, P.O. Box 5000, Upton, NY 11973-5000.

[1] CENPA Annual Report, University of Washington (2006) 53.

## 2.16 $^{100}$Tc electron-capture branching ratio with a Penning Trap

S. K. L. Sjue, A. García, A. Algora,* S. A. Hoedl, D. Melconian, H. Penttilä,†
H. E. Swanson, S. Triambak, and the IGISOL Collaboration

A reliable theory to calculate the neutrinoless-double-beta decay ($0\nu\beta\beta$) matrix element is necessary to interpret the results of $0\nu\beta\beta$ experiments. The mass-100 system offers a stringent test for nuclear models with five experimental observables as constraints: two-neutrino-double-beta decay to the ground state and to two excited states, the beta decay from $^{100}$Tc to $^{100}$Ru, and the electron-capture decay of $^{100}$Tc to $^{100}$Ru. Of these five decay rates, the electron-capture branch of $^{100}$Tc is the least well known. Experiments with $^{100}$Mo are under way to search for neutrinoless-double-$\beta$ decay ($0\nu\beta\beta$).[1] The electron-capture branch also determines the efficiency of $^{100}$Mo as a possible solar neutrino detector.

To measure the branching ratio for the electron-capture decay $^{100}$Tc(e,$\nu_e$)$^{100}$Mo, it is necessary to measure two numbers: the total number of decays and the number of electron captures. The electron-capture branch is small ($< 0.01\%$) compared to the $\beta$-decay $^{100}\text{Tc}\rightarrow \text{e}^- + \overline{\nu}_e + ^{100}\text{Ru}$ ($> 99.99\%$), so to better than 0.1% precision the number of $\beta$-decays is equal to the total number of decays. The number of electron captures follows from the number of x-rays emitted by the daughter, $^{100}$Mo. Difficulties with this measurement include the continuous low-energy background from the $\beta$-decay, x-rays from $^{100}$Ru that are very close in energy to the $^{100}$Mo x-rays, and possible contamination from isotopes produced via reactions other than $^{100}$Mo(p,n)$^{100}$Tc, such as $^{100}$Mo(p,2n)$^{99}$Tc.

To deal with these difficulties, we are using the IGISOL Penning Trap and a specially-designed scintillator. Our scintillator design (See Fig. 2.16-1.) couples to the vacuum system after the trap, provides a deposition target for the $^{100}$Tc ions very close to a Ge detector to maximize efficiency for x-ray detection, and gives nearly $4\pi$ steradians of solid-angle coverage to veto the continuous low-energy background from $\beta$-decays.

We had a preliminary run in Jyväskylä last November to confirm that our design and experimental plans would work. Because of the scintillator's small implantation aperture, our apparatus provided the most stringent test of their post-Penning Trap beam tuning to date; yet the excellent beam emittance form the Penning Trap provided us with $^{100}$Tc ions at a rate of 1.2(1) kHz at the end of the scintillator. Fig. 2.16-2 shows a comparison of the HPGe spectra with and without scintillator veto.

Currently, we are working on hardware at CENPA to minimize backgrounds and maximize our x-ray resolution. Recently we found and removed the cause of anomalies in our gamma-ray spectra that caused problems with data taken previously. Given a 1.2 kHz deposition rate, a $\beta$-veto efficiency of 80%, and assuming the previous measurement[2] of $BR_{EC} = 1.8(9)\times10^{-5}$, we expect to measure the electron-capture branch with a precision of

*IFIC CSIC-University, Valencia, Valencia, Spain.
†University of Jyväskylä, Jyväskylä, Finland.

[1] Phys. Rev. Lett. **95**, 182302 (2005); Phys. Rev. Lett. **85**, 2917 (2000).

[2] García *et al.*, Phys. Rev. C **47**, 2910 (1993).

15% or better at Jyväskylä this August.

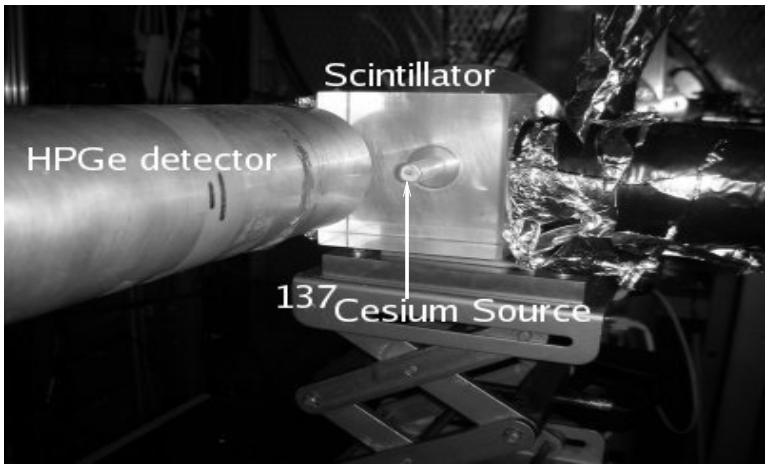


Figure 2.16-1. This picture shows the scintillator at the end of the beamline in Jyväskylä with a $^{137}$Cs calibration source inside it.

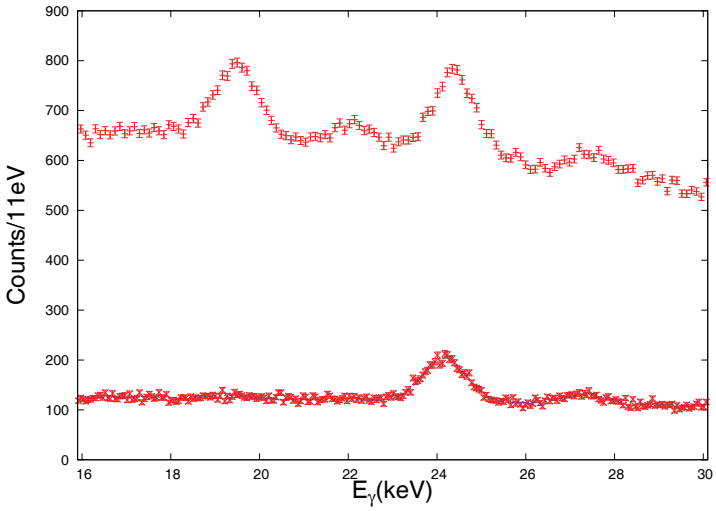


Figure 2.16-2. These are x-ray spectra before and after veto with the scintillator. The 19.2-keV Ru K$\alpha$ peak and continuous $\beta$-background from $^{100}$Tc$\rightarrow$e$^-$ + $\overline{\nu}_e$+$^{100}$Ru are drastically attenuated, which will help to resolve the 17.4 keV $^{100}$Mo K$\alpha$ that should come with better statistics. The Indium K$\alpha$ peak at 24 keV remains as a result of $\beta$-fluourescence of Indium within the detector. The actual experiment will use a detector without Indium.

## 2.17 Status of the ultra-cold neutron $A_\beta$ experiment at Los Alamos

A. García, S. A. Hoedl, D. Melconian, A. L. Sallaska, S. K. L. Sjue and the UCNA collaboration

Recent re-evaluations of $V_{ud}$ and especially $V_{us}$ have resolved the long-outstanding $\approx 2\sigma$ discrepancy in the unitarity test of the Cabbibo-Kobayashi-Maskawa (CKM) mass-mixing matrix.[1] This $3\times3$ matrix parameterizes the rotation between the weak and mass eigenstates of the quark families, and must be unitary if the Standard Model is complete. The most sensitive test is in the top row, *i.e.* whether $V_{ud}^2+V_{us}^2+V_{ub}^2$ is unity or not. Any deviations could point to new physics, such as right-handed currents and possible supersymmetric models; even with no deviation, the $10^{-4}$ precision of the unitarity test can be used as a stringent constraint on these models. The largest element by far is the effective coupling constant $V_{ud}$, and as such has the biggest impact in the unitarity test. $V_{ud}$ is most-precisely extracted from measurements of the comparative half-lives, or $ft$-values, of superallowed $0^+ \rightarrow 0^+$ $\beta$ decays.

Currently, theoretical uncertainties dominate the precision to which $V_{ud}$ can be extracted from these decays. Being a much simpler system compared to complex nuclei, neutron $\beta$ decay does not suffer from large theoretical uncertainties; however the precision of the experimental data must be improved for it to compete with $0^+ \rightarrow 0^+$ transition measurements. It is the goal of the Ultra-Cold Neutron Asymmetry (UCNA) collaboration to improve the measurement of the $\beta$-asymmetry parameter ($A_\beta$) which, when combined with the neutron lifetime, will provide a complementary measurement of $V_{ud}$ with a precision that is comparable to that of the superallowed decays.

In 2006, the UCNA collaboration made significant progress in developing the experiment:

- **production** – We have re-designed the source insert-and-flapper system to accommodate a larger open area for accepting UCN from the $SD_2$ source, and are currently installing a further improved version. We achieved longer source lifetimes by improving the coating of materials in the insert. Higher proton beam currents from LANSCE were shown to linearly increase UCN production, with no saturation effects seen yet.
- **transport** – Using careful on-line tests of our diamond-like coated quartz guides, we have improved the overall transmission of UCN from the source to the decay volume
- **$\beta$ detection** – near the end of the running period in 2006, we observed neutron decay in our $\beta$ detectors at a rate of 2 Hz with a signal-to-noise ratio of 5. We are working to improve vetoing of backgrounds from $\gamma$s and cosmic rays.

Implementing the above improvements is expected to be completed by the start of the 2007 run, resulting in an expected increase of $100\times$ more UCN in the decay volume. Our polarizer and spin-flipper have been tested off-line and will be tested on-line this year. We expect that we will make a 2% measurement of the $\beta$ asymmetry parameter in 2007.

[1] Marciano and Sirlin, Phys. Rev. Lett. **96** 032002 (2006), and the Particle Data Group's 2006 recommended values for $V_{us}$ and $V_{ub}$ (`http://pdg.lbl.gov`).

## 2.18 Characterization of ultracold neutron detectors for use in the UCNA experiment at LANL

A. García, S. A. Hoedl, D. Melconian, A. L. Sallaska and S. K. L. Sjue

Over the past year, we have completed the analysis of the ultracold neutron detector characterization experiment conducted at the Institut Laue-Langevin in Grenoble, France. Our detectors consist of silicon surface barrier detectors coupled with LiF or $^{10}$B-vanadium foils to convert the neutrons into detectable charged particles. The foils, previously described in detail,[1] must have a low nuclear potential in conjunction with a large neutron capture cross section. A very important feature of the foils is the cutoff velocity, below which the neutrons are reflected and cannot reach the detector. A gravitational spectrometer experiment was carried out at the ILL and was subsequently modeled with Monte Carlo simulations to quantitatively determine this cutoff velocity. In addition, elastic proton backscattering measurements were performed at the UW to accurately determine the foil densities, which are an input to the simulations via the detector efficiency.

The concept behind the gravitational spectrometer was to change the detector height in order to provide different gravitational barriers to UCN, thereby altering the shape of the velocity distributions at the detector. Our results are shown in Fig. 2.18-1, which plot the overall count rate as a function of detector height, in addition to the Monte Carlo results which will be discussed.

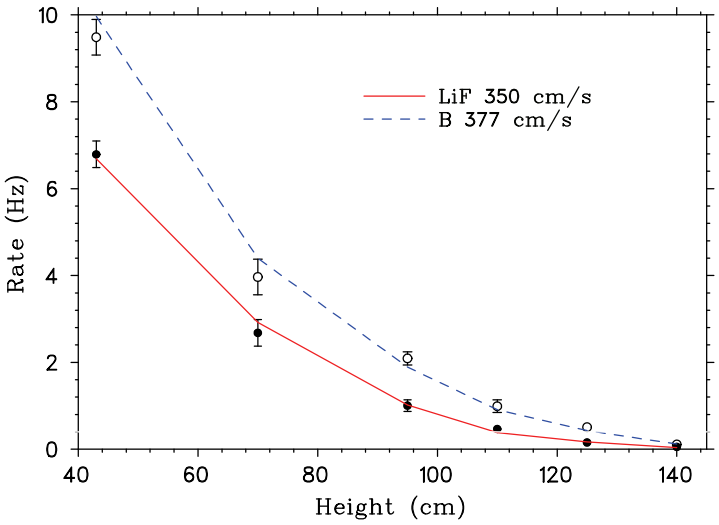


Figure 2.18-1. LiF and B/V data points with Monte Carlo results displayed as curves.

The goal of the analysis was to reproduce the data with a simulation of the neutron transport with an *assumed* cutoff velocity for each detector. In order to determine the values of various simulation parameters, data taken from a helium detector were used as

[1] CENPA Annual Report, University of Washington (2005) 8.

a calibration. The simulations moved the neutrons through the system, by combining the algebraic expression for the geometry (cylinders, grids, baffles) with the kinematic equations of motion to determine where and when the neutron's trajectory intersected the guide. Then it was decided whether the neutron escaped or reflected. The input parameters for the simulation were 1) guide specularity, 2) reflection and absorption, 3) a model for detector efficiency, 4) initial angular distributions and velocity distributions, 5) probability for diffusive scatters, 6) transport through materials, and 7) areal foil density.

Foil densities are crucial parameters in the comparison between Monte Carlo simulations and data. Along with the neutron absorption cross sections, they are inputs to the detection efficiency. Elastic backscattering measurements were performed with 1- and 3-MeV protons in order to determine the densities of the foils more accurately. Two 500=$\mu$m Canberra PIPS detectors were placed each at 150 degrees with respect to the proton beam and were shielded from multiple scatters in our 24-inch cylindrical chamber. Using the information from the calculated scattered proton energy, the peaks in the spectrum could be identified, and the densities could be determined given the known cross sections.

A 90 $\mu$g/cm$^2$ thick carbon foil served as a calibration to determine our solid angle accurately. The proton beam energy had to be high enough for the energy loss in the target not to exceed the energy difference between peaks. This implied running at energies where the cross sections have a non-Rutherford component. Therefore, there is an associated, small uncertainty with determining the solid angle due to the uncertainties in the cross sections found in the literature. The measured solid angle for our system yielded density results of 13.3$\pm$3.3 $\mu$g/cm$^2$ for boron and $(6.4^{+1.3}_{-1.1})x10^2$ $\mu$g/cm$^2$ for LiF.

Using the parameters set by the helium calibration and the average value for the surface densities, the cutoff velocities of the foils were determined. First, for the LiF foil, the normalization for each simulation data set was found by minimizing the $\chi^2$. This value of the $\chi^2$ was then plotted as a function of cutoff velocity for each simulation. In order to determine the real value of the cutoff velocity, these points were fit to a parabola whose minimum yielded the final value. For the LiF foil, this value was 350 $\pm$ 14 cm/s. Using the normalization from the simulation yielding the final LiF cutoff, the same procedure was applied to determine the boron and vanadium foil's cutoff velocity. This same normalization was used to maintain the experimentally given relationship between LiF and boron data sets. The boron and vanadium foil's final cutoff is 377 $\pm$ 4 cm/s.

Both of the determined cutoffs for the LiF foils and for the boron and vanadium foils are above the values calculated from their scattering lengths. In the spectra from elastic proton scattering for the LiF foil, oxygen is the dominant contaminant. However, the boron foil's spectra shows not only oxygen but carbon as well. The amount of these contaminants is consistent with the quantity needed to increase the cutoff as observed. Reasons for this contamination include cracking carbon onto the foils during implantation, as well as insufficient vacuum. Clearly, an extremely low vacuum during fabrication, as well as minimizing other sources of contamination, is crucial.

## Quantum Optics

### 2.19 A test of quantum nonlocal communication*

J. G. Cramer, W. G. Nagourney, and S. Mzali†

"Quantum entanglement," a phrase first coined by Erwin Schrödinger,[1] describes a condition of the separated parts of the same quantum system in which each of the parts can only be described by referencing the state of other part. This is one of the most counterintuitive aspects of quantum mechanics, because classically one would expect system parts out of speed-of-light contact to be completely independent. Thus, entanglement represents a kind of quantum connectedness in which measurements on one isolated part of an entangled quantum system have non-classical consequences for the outcome of measurements performed on the other (possibly very distant) part of the same system. This quantum connectedness that enforces the measurement correlation and state-matching in entangled quantum systems has come to be called quantum nonlocality.

Nonlocality was first highlighted by Albert Einstein and his coworkers Boris Podolsky and Nathan Rosen in their famous EPR paper.[2] They argued that the nonlocal connectedness of quantum systems requires a faster-than-light connection that appears to be in conflict with special relativity. Despite this objection, quantum nonlocality has been demonstrated in many quantum systems. In the physics community it is now generally acknowledged to be implicit in the quantum formalism as applied to entangled systems.

The question we are investigating is whether quantum nonlocality is the private domain of nature, or whether it can be used in experimental situations to send signals from one observer to another. A number of authors[3] have presented "proofs" that such nonlocal observer-to-observer communication is impossible within the formalism of standard quantum mechanics. However, it has recently been pointed out[4] that at least some of these "proofs" ruling out nonlocal signaling are tautological, assuming that the measurement process is local and thereby building the final conclusion of no signaling into their starting assumptions. Standard quantum mechanical Bose-Einstein symmetrization has been raised as a counter-example, shown to be inconsistent with initial "proof" assumptions. Therefore, the possibility of nonlocal communication in the context of standard quantum mechanics seems to remain open and appropriate for experimental testing. We have undertaken such an experimental test, because it represents an unusual opportunity to address very fundamental issues of quantum mechanics with a relatively simple table-top experiment.

The experiment, shown in Fig. 2.19-1, is presently under development in the UW Laser Physics Facility in the basement of the Physics-Astronomy Building. It tests for the possi-

*not supported by DOE CENPA grant.

†UW undergraduate.

[1] E. Schrödinger, *Proc. of Cambridge Philos. Soc.* **31**, 555 (1935); **32**, 446 (1936).

[2] A. Einstein, B. Podolsky, and N. Rosen, Phys. Rev. **47**, 777 (1935).

[3] P. H. Eberhard, Nuovo Cimento B **38** 75 (1977), ibid. B **46**, 392 (1978); G. C. Ghirardi, A. Rimini, and T. Weber, Lett. Nuovo Cimento **27**, 293 (1980).

[4] K. A. Peacock and B. Hepburn, *Proc. of Meeting of Society of Exact Philosophy* (1999), quant-ph/9906036.

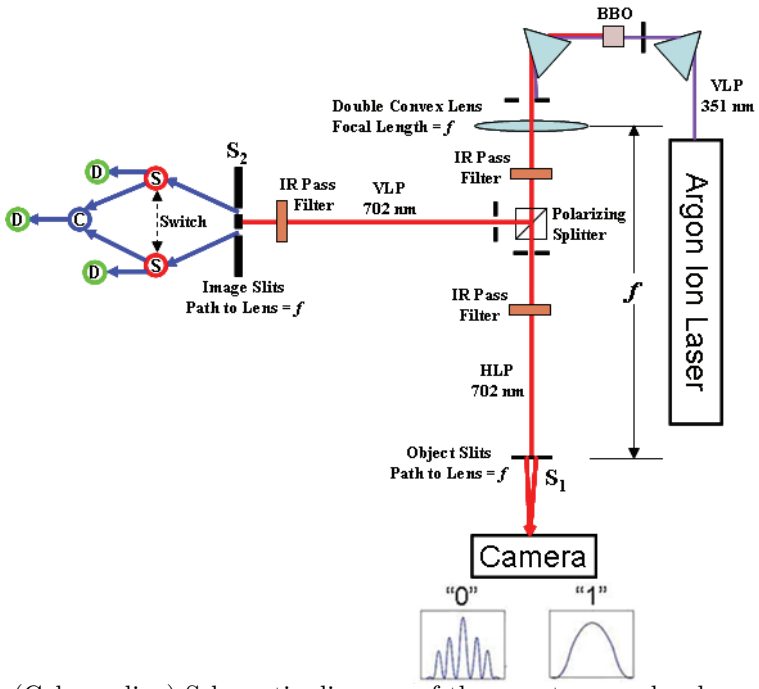


Figure 2.19-1. (Color online) Schematic diagram of the quantum nonlocal communication test setup

bility of nonlocal communication. It is synthesis of the ideas embodied in the Ghost Interference experiment of the Shih group[5] and the Ph.D. thesis experiment of Birgit Dopfer.[6] An argon-ion laser producing vertically polarized 351 nm UV light pumps a beta barium borate (BBO) crystal, producing two 702 nm infrared photons that are collinear with and momentum-entangled with the pump beam by the process of Type II collinear spontaneous downconversion. The pump beam is deflected away from the entangled photon pairs by refraction in a prism, and the entangled photons, one linearly polarized vertically (VLP) and the other linearly polarized horizontally (HLP), are sent in separate directions by a polarizing splitter. A lens of focal length $f$ is placed in the path after the BBO crystal and before the polarization splitter, so that both entangle photons pass through the lens. A pair of slits at $S_1$ is placed at a path length $f$ beyond the lens in the path of the HLP photons, which are transmitted by the splitter. Because of the momentum entanglement, an image of slit system $S_1$ will be formed by the VLP photons reflected by the splitter at a path length $f$ beyond the lens at position $S_2$. We note that Dopfer has already demonstrated such slit imaging with a slightly different optical arrangement.

At the image position of each slit at $S_2$ we place an optical fiber, as shown. The fibers conduct the light to an optical switch, at which the light is either sent directly to two avalanche photodiode detectors (providing which-way information about which S1 slit the photon entered), or alternatively is routed to an optical combiner and then detected by a third avalanche

[5]D. V. Strekalov, A. V. Sergienko, D. N. Klyshko, and Y. H. Shih, Phys. Rev. Lett. **74**, 3600 (1995).

[6]B. Dopfer, Ph.D. Thesis, University of Innsbruck, Christoph-Probst-Platz, Innrain 52, 6020 Innsbruck, Austria,(1998).

photodiode, so that waves passing through both slits can contribute constructively to the detection event.

A quantum sensitive CCD camera is used to measure distributions for the HLP photons and is expected to produce distributions like those shown at the bottom of Fig. 2.19-1. If the switch transmits light to the outer detectors, detection provides information on the slit through which the photon's entangled twin has passed, since momentum entanglement correlates the slit positions of the two photons. In this case, the camera should record the broad diffraction pattern labeled "1". On the other hand, if the switch is in the position leading to the combiner and middle detector, waves passing through both slits contribute coherently to the detection, no which-way information is available, and the camera should record the structured interference pattern labeled "0" in Fig. 2.19-1. Effectively, by changing the switch one is forcing the VLP entangled photon to behave like particles when which-way information is provided and like waves when it is not. The interference or diffraction patterns observed in the other arm of the experiment by the camera for the HLP photons depend on whether this photon is nonlocally forced into particle-like or wave-like behavior by the measurements performed on its entangled twin. The nonlocal connection would become communication.

Observing such a change in the photon distribution at the camera as a result of the fiber switching would thus constitute a direct demonstration of nonlocal communication and would falsify the no-signal "proofs" mentioned above. We note that such nonlocal communication will perhaps be prevented by the complementary relation that exists between wave coherence at the slits and momentum entanglement of the downconverted photons.[7] The goal of the experiment is to find the best compromise between entanglement and coherence, to see whether nonlocal communication is indeed possible and if not, to understand in detail the physical mechanisms that prevent it.

At present, this experiment is still under construction. We are making tests at the UW Laser Physics Facility with a 300 mW argon-ion UV laser, a tilted BBO crystal, and a cooled CCD camera to observe and optimize the downconversion process. The avalanche photodiodes, associated electronics, optical switches, fibers, and high-quality filters needed for the final configuration shown in Fig. 2.19-1 are not yet available, but we hope to obtain them soon.

[7] A. F. Abouraddy, *et al.*, Phys. Rev. A **63** 063803 (2001).

# 3 Nuclear Astrophysics

## 3.1 Precision measurements of the $^3$He($\alpha$,$\gamma$)$^7$Be cross section

T. A. D. Brown, A. M. Crisp,* P. Ellerbroek, M. Fredrickson, D. Melconian, A. L. Sallaska, S. K. L. Sjue, K. A. Snover, D. W. Storm, S. Triambak, P. Morse and D. Zumwalt

During the last year measurements of the $^3$He($\alpha$,$\gamma$)$^7$Be cross section have been successfully made at six different energies between $\overline{E}_{CM}$ = 425 keV and $\overline{E}_{CM}$ = 1234 keV. The set-up and preliminary work for these measurements are described in previous annual reports.[1,2]

Two different methods have been used to determine the cross section of the $^3$He($\alpha$,$\gamma$)$^7$Be reaction: measurement of the prompt $\gamma$-ray yield and measurement of the $^7$Be activity. The prompt $\gamma$-rays were measured during the irradiation of a gas cell target[2] using a 100 % efficient Ge detector. The $^7$Be nuclei produced in the reaction implant themselves into a OFHC copper backplate. Upon completion of the irradiation, the backplate was removed and the resulting $^7$Be activity was measured using a second Ge detector. For the purposes of catching any back-scattered $^7$Be nuclei, a tantalum liner was used in the cell during irradiation and was removed and counted with the copper backplate. The $^7$Be activity was measured for typically 2 - 4 weeks (depending on beam energy), giving a statistical error of under 3 % .

| $E_{beam}$ (MeV) | Ni foil thickness ($\mu$m) | Gas pressure (Torr) | $\overline{E}_{CM}$ (MeV) | $t_{Irr}$ (hrs) |
|---|---|---|---|---|
| 3.5 | 1.065 | 200 | 1.234 | 12 |
| 2.6 | 1.072 | 200 | 0.799 | 19 |
| 2.35 | 1.065 | 100 | 0.701 | 23 |
| 2.1 | 1.065 | 100 | 0.581 | 23 |
| 1.9 | 0.955 | 100 | 0.517 | 29 |
| 1.7 | 0.937 | 100 | 0.425 | 115 |

Table 3.1-1. Run parameters for each $^3$He($\alpha$,$\gamma$)$^7$Be measurement. The irradiation time ($t_{Irr}$) indicates the length of time data was taken with $^3$He in cell.

Table 3.1-1 describes the beam energy, nickel foil thickness (used as the cell entrance window), gas pressure and irradiation time used for each measurement. For the purposes of determining the beam background contribution under the $\gamma_0$ peak, gamma-ray spectra were measured using $^4$He in the cell before and after gamma-ray measurements were taken with $^3$He. In order to verify the reliability of our beam current integration, the measurement at $E_{beam}$ = 3.5 MeV was repeated using a smaller beam collimator size. The charge collection on the gas cell was also checked by insulating the cell from the adjoining extension tube,[2] and measuring the currents induced in the cell and the tube during irradiation. Both of these tests have suggested that our current integration is good.

In the case of each of the above measurements, the cross section obtained from the analysis of the prompt $\gamma$-ray yield is within 5 % of the value obtained from the analysis of the $^7$Be activity. We are currently undertaking a cross section measurement at $E_{beam}$ = 1.5 MeV and intend to make one or two further measurements at lower energies.

*Florida State University, FSU Physics, 315 Keen Building, Tallahassee, FL 32306-4350.

[1]CENPA Annual Report, University of Washington (2006) 45-48.

[2]CENPA Annual Report, University of Washington (2005) 52-54.

## 3.2 E0 emission in $\alpha$ + $^{12}$C fusion at astrophysical energies[1]

G. Baur,* K. A. Snover and S. Typel†

One of the most important reactions in nuclear astrophysics is $^{12}$C + $\alpha \rightarrow ^{16}$O capture. Stellar evolution and nucleosynthesis calculations[2] indicate the total S-factor for this reaction must be close to 170 keV b at a center-of-mass energy $E_{c.m.} = 0.3$ MeV, the center of the Gamow window. The results of many experiments over more than three decades, extrapolated to the Gamow window, show that single-photon emission is dominated by E1 and E2 decay to the $^{16}$O ground-state, with approximately equal intensity and a combined S-factor S(0.3) approaching the value quoted above.[3] Capture to excited final states in $^{16}$O is not negligible. Rolfs[4] has speculated that E0 emission may also be important. If so, it would have escaped observation in $^{12}$C + $\alpha \rightarrow ^{16}$O capture measurements since they were made by detecting the emitted $\gamma$-rays, and the $e^+e^-$ pairs produced by E0 emission would not result in a sharp gamma line near the transition energy.

E0 emission in $^3$He + $^4$He fusion has been shown to be negligible.[5] However, in $^{12}$C + $\alpha \rightarrow ^{16}O_{g.s.}$ there are several factors that may enhance the relative importance of E0 emission at astrophysical energies: 1) E0 emission occurs by s-wave capture, whereas E1 and E2 emission arise from p-wave and d-wave capture, respectively; 2) E1 emission is isospin-inhibited; and 3) the higher transition energy results in larger E0/E1 and E0/E2 phase-space factor ratios.

In low-energy $^3$He + $^4$He fusion, E0 and E2 direct capture occur between the same initial and final states (p-waves), and as a result the direct capture radial matrix elements cancel in the cross section ratio. In $^{12}$C + $\alpha \rightarrow ^{16}O_{g.s.}$, however, the radial matrix elements are different since the initial states are different. In analogy with Eq. 11 of ref. 5 we obtain

$$\frac{\sigma_{E0}}{\sigma_{E2}} = \frac{4\pi}{5}\frac{f_{E0}}{f_{E2}}\frac{|R_{00}|^2}{|R_{02}|^2}, \tag{1}$$

where $R_{l_f l_i}$ is the radial integral of $r^2$ between the initial continuum state with orbital angular momentum $l_i$ and the final bound state with $l_f = 0$, and the quantities $f_{EL}$ contain the coupling constants, statistical and phase space factors.

We estimate $|R_{00}|^2/|R_{02}|^2 = P_0/P_2 = 18$ at $E_{c.m.} = 0.3$ MeV, where $P_{l_i}$ is the Coulomb penetrability evaluated at $R = 1.3(A_1^{1/3}+A_2^{1/3})$ fm = 5 fm. This yields 4.3 x $10^{-3}$ for the direct (i.e., nonresonant) E0/E2 cross section ratio at 0.3 MeV.

This estimate for $|R_{00}|^2/|R_{02}|^2$ assumes the capture takes place at the nuclear radius and is not affected by the nuclear interaction between $^{12}$C and the $\alpha$ particle in the continuum.

[1] G. Baur, K. A. Snover and S. Typel, nucl-th/0701027v2.

*Forschungszentrum Jülich, Institut für Kernphysik, D-52425 Jülich, Germany
†GANIL, Bd. Henri Becquerel, BP 55027, F-14076 Caen Cedex 05, France

[2] T. A. Weaver and S. E. Woosley, Phys. Rep. **227**, 65 (1993).
[3] J. W. Hammer *et al.*, Nucl. Phys. A **768**, 353c (2005).
[4] Various unpublished conference talks, including NIC XIII (2004).
[5] K. A. Snover and A. E. Hurd, Phys. Rev. C **67**, 055801 (2003).

However, at low collision energies the effective radius may be larger, due to the importance of extranuclear capture, which would reduce $|R_{00}|^2/|R_{02}|^2$. In addition, the total E2 capture cross section in the Gamow window is dominated by the tail of the subthreshold 6.92 MeV $2^+$ state, and this effect is also not included above.

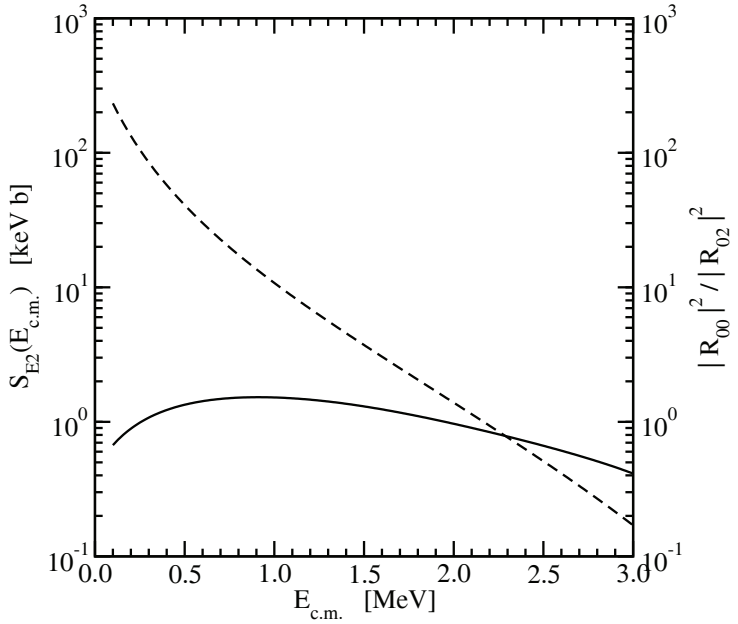


Figure 3.2-1. Dashed curve and left scale: E2 S-factor; solid curve and right scale: E0/E2 radial matrix element ratio; vs. $E_{c.m.}$.

We have improved on the above estimate by carrying out potential model calculations of E0 and E2 emission in $^{12}$C + $\alpha \rightarrow ^{16}$O$_{g.s.}$. We used a real Woods-Saxon potential, with depths for the $l_f = 0$ final (bound) state and for the $l_i = 0$ and 2 initial (continuum) states that bind the $0_1^+$, $0_2^+$ and $2_1^+$ states, respectively, at the correct energies. The results are shown in Fig. 3.2-1. Our calculated E2 S-factor is within a factor of 2 of the measured E2 S-factor below $E_{c.m.} = 2$ MeV, and has $S_{E2}(0.3) = 85$ keV b, in agreement with the value 81 $\pm$ 22 keV b obtained by Hammer *et al.*[3] from an extrapolated R-matrix fit to E2 data. We obtain $|R_{00}|^2/|R_{02}|^2 = 1.1$ for the ratio at 0.3 MeV, as shown in Fig. 3.2-1. Taking $S_{E2}(0.3)$ = 80 keV b, this corresponds to

$$S_{E0}(0.3) = 0.02 \text{ keV b}. \tag{2}$$

Tails of higher lying $0^+$ resonances as well as the tail of the isoscalar Giant Monopole Resonance contribute negligibly at 0.3 MeV. E0 emission to excited final states in $^{16}$O is negligible due to the small phase space factor. Two-photon emission is also negligible. Thus we conclude that electromagnetic processes other than single-photon emission do not contribute significantly to the astrophysical rate for $^{12}$C + $\alpha$ fusion.

## 3.3 Motivation for Measuring the $^{22}$Na(p,$\gamma$)$^{23}$Mg Reaction Rate

T. A. D. Brown, A. García, A. L. Sallaska, K. A. Snover and D. W. Storm

$^{22}$Na is a long sought after and elusive cosmic ray gamma emitter, which has not been detected outside the galactic bulge. However, if found, it would provide pointers to a *localized* gamma ray source due to its short lifetime ($T_{1/2} = 2.6$ y, $E_\gamma = 1.275$ MeV), which precludes significant spreading. Some nucleosynthesis models indicate that $^{22}$Na should be produced prolifically in novae. Nova outbursts are triggered by the accretion of gas from a nearby star onto a degenerate white dwarf. Due to the high density of the white dwarf and its subsequently strong gravitational field, the accreted particles have very high velocities, raising the surface temperatures on impact. When this temperature rises enough to stimulate nuclear reactions, copious amounts of energy are violently released. The main component of the accreted gas is hydrogen, which is sparse on a white dwarf whose hydrogen has previously been converted to heavier elements such as carbon and oxygen. This fresh hydrogen provides the catalyst for a series of new reactions which occur much more rapidly than those with other light nuclei. During a nova outburst, an outer layer of the star is ejected, containing a variety of heavier, newly synthesized elements, theoretically including $^{22}$Na.

Some evidence for existence of terrestrial $^{22}$Na originates from the discovery of pure $^{22}$Ne in the Orgueuil meteorite in 1972[1]. This meteorite contained a ratio of $^{22}$Ne/$^{20}$Ne $\geq 0.67$, which is stunning since the terrestrial abundance yields a ratio of only 0.10. Because $^{22}$Na decays into $^{22}$Ne, it is highly probable that this ratio is excessively large due to formerly present $^{22}$Na that somehow made its way from novae into meteorites. With the aid of orbiting gamma ray observatories such as the INTEGRAL satellite, it would be possible to detect $^{22}$Na from its signature 1275 keV gamma ray if its abundances are high enough. This observation would severely constrain nucleosynthesis models involving $^{22}$Na.

The abundance of $^{22}$Na is dramatically influenced by its destruction via the reaction $^{22}$Na(p,$\gamma$)$^{23}$Mg. Recently, a new level in $^{23}$Mg has been discovered[2] that could have a direct impact on this rate, which could eliminate this discrepancy between nucleosynthesis models and observation. If the resonance strength

$$\omega\gamma = \frac{(2J(^{23}\mathrm{Mg})+1)\Gamma_p\Gamma_\gamma}{(2J(^{22}\mathrm{Na})+1)(2J(p)+1)\Gamma}$$

is high enough ($\omega\gamma \geq 4$ meV), it would be the dominant contribution to the rate at novae temperatures. Therefore, it is highly desirable to measure this resonance strength.

[1] S. Seuth, et. al., Nucl. Phys. A **514** (1990) 471.
[2] Jenkins, *et al.*, Phys. Rev. Lett. **92**, 031101 (2004).

## 3.4 Technical developments of the $^{22}$Na(p,$\gamma$)$^{23}$Mg experiment

T. A. D. Brown, A. García, A. L. Sallaska, K. A. Snover and D. W. Storm

Since the summer of 2006, the $^{22}$Na(p,$\gamma$)$^{23}$Mg experiment has rapidly begun to take physical form, culminating in the complete refurbishment of the 0 degree beamline. This experiment consists of two parts: one involves the fabrication of the radioactive $^{22}$Na targets, which will be performed by our collaborators at TRIUMF; the other consists of measuring the new resonance as well as improving the errors ($\approx$ 50 %) on previously measured neighboring resonances. This will be performed on the newly constructed beamline at the University of Washington.

Most of the work at this university this year revolved around designing and building this beamline. The previous beamline was completely taken apart and had all of its reusable components thoroughly cleaned. New beam supports were erected in order to have more flexibility with the positioning of the two quadrupole magnets. Simulations were performed to optimize focusing of the beam, indicating that both magnets needed to be moved approximately four feet upstream. This necessitated moving the upstream magnet to the other side of the shielding wall between the experimental hall and the accelerator. Beam components that are also being reused include a cold trap, a cryogenic vacuum pump, several gate valves, a beam scanner, and a set of steerers. A second set of steerers, along with a rastering device, were both fabricated solely for this experiment. The construction of the beamline is complete up to the target chamber. The box is currently being designed at TRIUMF and is being manufactured in our machine shop. In addition, a new vacuum valve control box was constructed and installed, as well as a power transfer module to switch power for beamline components, such as the steerers, from one beamline to another. This also enables manipulation of the various magnets from the control room.

Penelope simulations have been performed in order to optimize the shielding around the two 100% Germanium detectors, located at $\pm$55 degrees to simplify the total cross section determination. The shielding must balance between minimizing the 1275 keV gammas from the radioactive target while maximizing the transmission of 5 MeV gammas of interest from the new resonance. The ratio of detection efficiency for the 5 MeV resonance gammas to 1275 keV gammas is not very sensitive to different configurations of shielding materials, which include lead, copper, and plastic. There must, however, be some type of shielding to reduce the 511 keV gammas, and minimize the rate our detectors see, which is limited to $\sim$ 20 kHz. To that end, 2 cm of lead followed by 5 cm of copper has been chosen with the detectors 21.5 cm from the target.

Another important form of shielding is from cosmic rays. In order to test the utility of such shielding, a experiment was set up with existing plastic scintillators and PMTs to use in anticoincidence with a signal from a 50% Germanium detector. Fig. 3.4-1 demonstrates the ability to reject cosmic rays as a function of energy for several runs.

At the 5-MeV energy of interest to $^{22}$Na(p,$\gamma$)$^{23}$Mg, nearly 80% of cosmic rays were rejected, which clearly demonstrates the benefits of installing this shielding.

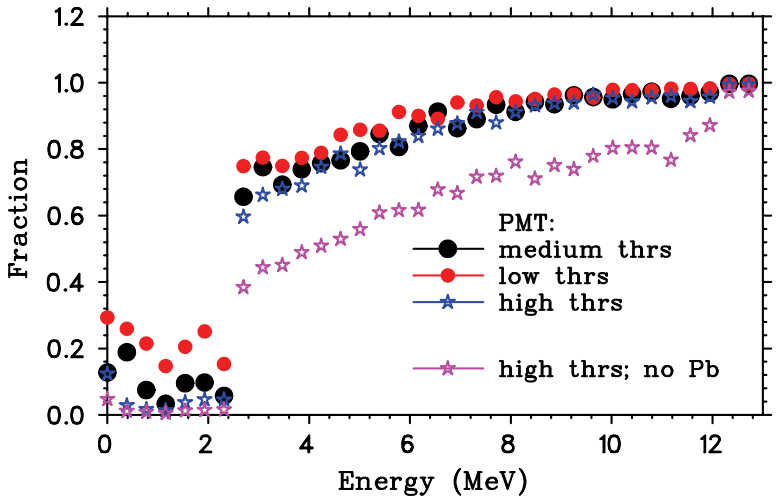


Figure 3.4-1. Fraction of Cosmic Rays rejected.

In addition to $^{22}$Na targets, we will also use $^{23}$Na targets to understand our system without the danger of radioactivity. Several targets have already been fabricated in the off deck beamline of the tandem with an energy of 30 keV and an average current of 75 nA on either copper or carbon substrates. To test our ability to produce these targets, we performed elastic proton backscattering in the 24" chamber to extract their densities. Fig. 3.4-2 illustrates the spectrum from 1-MeV protons on target with a 90 $\mu$g/cm$^2$ carbon backing. The sodium peak is cleanly resolved and yields a density of 0.65 $\mu$g/cm$^2$.

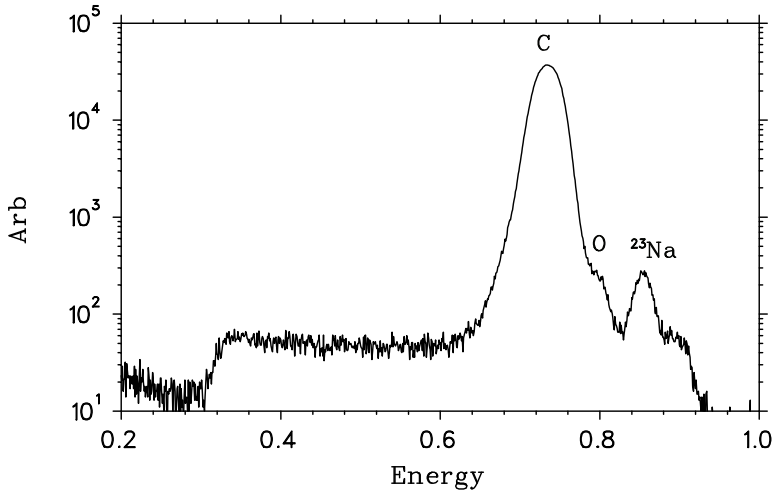


Figure 3.4-2. 1-MeV proton backscattering spectrum.

# 4 Nuclear Structure

## 4.1 Investigation of states in $^{33}$Cl using $^{32}$S$(p,\gamma)$

O. Biesel, A. García, D. Melconian, M. Mella* and S. Triambak

The energy calibration of the $\beta$-delayed proton spectrum from $^{33}$Ar is carried out using the excitation energies in $^{33}$Cl determined from $^{32}$S$(p,\gamma)$ resonances. This energy calibration plays an important role in determining the $e^+ - \nu$ correlation from $^{32}$Ar $\beta$-decay.

We obtained the excitation energies of states in $^{33}$Cl (that were used for the calibration of the $\beta$-delayed protons from $^{32}$Ar via $^{32}$S$(p,\gamma)$ resonances. The states were produced by impinging protons at different energies on S targets of varying thicknesses. The corresponding de-excitation $\gamma$-rays were registered using a 50% efficient HPGe detector at 0° to the beam. The $\gamma$-ray energy calibration was obtained using a $^{56}$Co source, known $^{27}$Al$(p,\gamma)$ lines and precise Monte Carlo simulations. Our measured excitation energies agree with previous measurements with much improved precision.

In addition, we determined the width of the $J^\pi = 3/2^+$ state in $^{33}$Cl at $E_x = 3971$ keV and solved a discrepancy that was previously reported.[1] The width of the resonance was determined by measuring the excitation function around the resonance using a thin S target. The target consisted of $\approx 200$Å of $Sm_2S_3$ on a $\approx 300$ $\mu$g/cm$^2$ thick Au foil. It was mounted in the target chamber such that most of the beam passed through the Au foil and deposited itself on a water cooled, 0.5 mm thick Au backing. This minimized local heating of the target to avoid tails in the excitation function due to diffusion. Our measured width had an upper limit of $\Gamma \leq 0.3$ keV, which was in significant disagreement with the previously measured value. Figure Fig. 4.1-1 shows the excitation function around the $E_x = 3971$ keV state. For comparison, we also show the excitation function around the $E_x = 3979$ keV resonance which has a narrow width.[2]

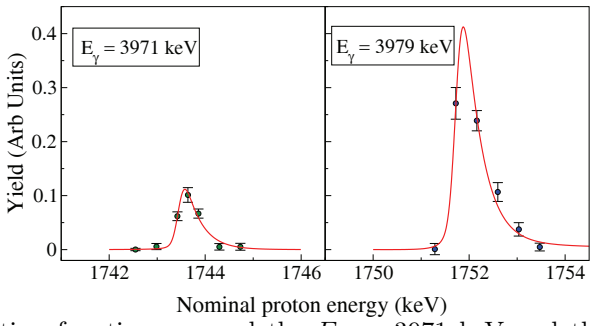


Figure 4.1-1. Excitation functions around the $E_x = 3971$ keV and the $E_x = 3979$ keV resonances.

As by-products of this work, we also determined the relative $\gamma$ branches from the state at $E_x = 3971$ keV which were found to be in significant disagreement with the previously measured values.

*Presently at Department of Physics and Astronomy, Dartmouth College, 6127 Wilder Laboratory, Hanover, NH 03755-3528.

[1] CENPA Annual Report, University of Washington (2006) 55.

[2] M. M. Aleonard *et al.*, Nucl. Phys. A **257**, 490 (1976).

## 4.2 Measurement of the absolute $\gamma$ branches in the decay of $^{32}$Cl

C. Bordeanu, A. García, J. C. Hardy,* V. E. Iacob,* D. Melconian, N. Nica,*
H. I. Park,* G. Tabacaru,* L. Trache,* S. Triambak, R. E. Tribble* and Y. Zhai*

The largest final systematic uncertainty in the measurement of the $ft$ value of $^{32}$Ar[1] arises from the uncertainty in the HPGe $\gamma$ efficiency. The $\gamma$ decay of $^{32}$Cl covers the same range of energies, and since $\approx 10\%$ of the time it is a daughter product of $^{32}$Ar, a precise knowledge of these branches will provide us with an *in situ* calibration of our HPGe detectors. Our goal in this experiment is to measure the absolute $\gamma$ branching ratios of $^{32}$Cl to $\pm 1\%$, thereby reducing the dominant systematic in our measurement of the $ft$ value of $^{32}$Ar by a factor of five.

The experiment was done at the Cyclotron Institute at Texas A&M University using their fast-tape transport system at the end of the MARS beamline. The data analysis is almost finished; all that remains is to check summing corrections. Preliminary analysis indicates that, except for the ground state $\beta$ branching ratio, we will reduce uncertainties in all of the other $\beta$ and $\gamma$ branching ratios by about an order of magnitude. The ground state branch is difficult to measure because there are no $\gamma$ rays to observe, and so one needs to precisely understand background contamination levels. We are able to measure this branch to about the same precision as was previously measured and find consistent results. These preliminary results (*i.e.* all but summing corrections completed) yield the decay scheme shown in Fig. 4.2-1. See also Sec. 4.3 for implications of this work.

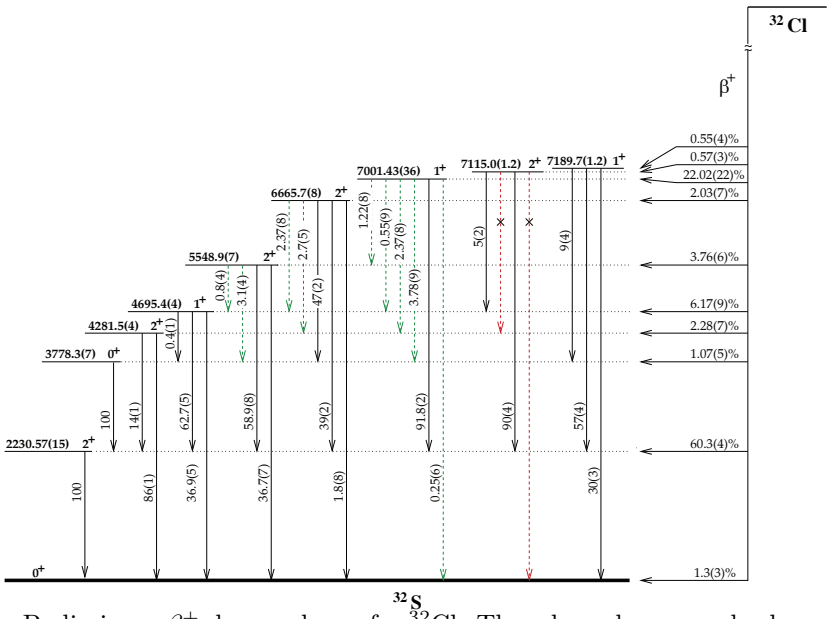


Figure 4.2-1. Preliminary $\beta^+$ decay scheme for $^{32}$Cl. The $\gamma$ branches are only shown if there is a $> 2\sigma$ signal.

*Cyclotron Institute, Texas A&M University, MS #3366, College Station, TX 77843-3366.

[1]CENPA Annual Report, University of Washington, (2006) 53.

## 4.3 Delayed $\gamma$ branches from $^{32}$Ar $\beta$-decay

E. G. Adelberger, M. Bhattacharya,* A. García, A. Komives,† D. Melconian, H. E. Swanson and S. Triambak

The $ft$ value for the $0^+ \rightarrow 0^+$ superallowed $\beta$-decay of $^{32}$Ar provides a useful test of theoretically calculated isospin symmetry breaking corrections[1] for nuclear beta decays. These corrections are important for precise tests of CKM unitarity, which are important to put limits on new scenarios such as the presence of right-handed currents and supersymmetric extensions to the Standard Model.

The accuracy of the $ft$ value for the $0^+ \rightarrow 0^+$ decay of $^{32}$Ar is currently limited by the rather large uncertainty in the superallowed branch ($\approx 13\%$). We are presently in the final stages of data analysis to obtain the branch with sub-percent precision from an experiment at Michigan State University. The superallowed branch is determined by measuring with high precision the absolute $\beta$-delayed proton and $\gamma$ branches following the superallowed decay. These branches were determined by implanting a known number of $^{32}$Ar nuclei in a stack of Si detectors surrounded by an array of HPGe detectors and counting the subsequent decays. We have already determined the superallowed proton branch to 0.1%. In order to determine the superallowed $\gamma$ branch (which is $\approx 6\%$ of the total superallowed branch), an accurate efficiency calibration of the HPGe detectors and a thorough understanding of the systematic uncertainties is required. The $\gamma$-detection efficiency calibration is obtained using the known $\gamma$-ray intensities[2] from the $\beta$ decay of the daughter $^{32}$Cl nuclei that do not decay via proton emission.

We are presently investigating sources of possible systematic uncertainties in the determination of the absolute superallowed $\gamma$ branch using PENELOPE Monte Carlo simulations. These include the effects of coincidence summing of $\gamma$-rays, the $\gamma - \gamma$ angular correlations and detector solid angle, which need to be carefully accounted for to obtain an accurate determination of the superallowed $\gamma$ branch.

Preliminary analysis indicates that the experimentally determined isospin-breaking correction is found to be

$$\delta_C^{\mathrm{Exp}} = (3.8 \pm 0.6)\% \ , \tag{1}$$

which can be compared to the theoretically calculated value of [3]

$$\delta_C^{\mathrm{Theo}} = (2.0 \pm 0.4)\% \ . \tag{2}$$

This is the first such measurement for a $T = 2$ decay, which can be extended to other cases to place CKM unitarity tests on a secure footing.

*Present address: Brookhaven National Lab, P.O. Box 5000, Upton, NY 11973-5000.
†DePauw University, 602 S. College Ave. , Greencastle, IN 46135-0037.
[1] CENPA Annual Report, University of Washington (2006) 53.
[2] See §4.2.
[3] B. A. Brown, private communication.

# 5 Relativistic Heavy Ions

## 5.1 Summary of event structure research

T. A. Trainor

The main subject of this program is study of the colored medium produced in RHIC heavy ion (HI) collisions. The structure and sources of minijet (low-$Q^2$ parton fragments) correlations have been extensively studied. We find that a large amount of structure associated with initial-state parton scattering survives to kinetic decoupling, but is strongly modified for more-central A-A collisions. We observe that minijet structure in $p_t$ correlations follows a simple $\log(\sqrt{s_{NN}})$ trend down to a threshold at 12 GeV. Claims of complete thermalization in RHIC collisions should therefore be re-examined. We now move to studies of azimuth multipole moments, of which the quadrupole moment is conventionally identified with "elliptic flow." We precisely separate the quadrupole component from the minijet component *via* 2D angular autocorrelations for the first time. The general topics we report are

- Accurate centrality determination for all A-A collisions
- Comprehensive survey of number correlations in A-A collisions
- Correlations of identified particles in A-A collisions
- Comprehensive study of azimuth multipole structure attributed to "flows"
- Distinction between "flows" and "nonflow" using 2D angular autocorrelations
- The energy and centrality dependence of azimuth multipoles
- The relation of "elliptic flow" to hydrodynamics
- The relation of minijets and parton dissipation to the reaction plane

Our centrality determination methods permit accurate centrality measurement from N-N collisions to $b = 0$ central A-A collisions with uncertainty at the percent level. That opens the most peripheral 20% of A-A centrality to study for the first time at RHIC. The onset of collectivity in peripheral collisions is now accessible to measurement. The identified-particle studies anticipate installation of the STAR time-of-flight barrel in the near future. Using TPC dE/dx we are limited to low-$p_t$ particles, but much structure has already emerged. We have initiated a study of azimuth multipole moments, among which the quadrupole moment is identified with elliptic flow. Accurate measurements with 2D angular autocorrelations precisely separate "nonflow" (minijets) from "flow" and reveal energy and centrality systematics of "elliptic flow" which appear to be inconsistent with a hydrodynamic picture. Another new initiative is study of minijets in relation to the reaction plane: how is low-$Q^2$ parton dissipation related to the transverse matter distribution?

## 5.2 Accurate centrality determination in A-A collisions down to single N-N collisions

D. J. Prindle and T. A. Trainor

The centrality (impact parameter) dependence of A-A collisions provides essential information about collision dynamics. At a basic level we want to know to what extent an A-A collision differs from a linear superposition of some reference number of N-N (nucleon-nucleon) collisions. The difference represents collective A-A dynamics, the main purpose of the RHIC experimental program. Until recently, the 20% most-peripheral A-A collisions were abandoned from the RHIC program by *fiat* because of the perception that centrality errors in that region are unmanageable. We have reversed that unfortunate situation with novel techniques.

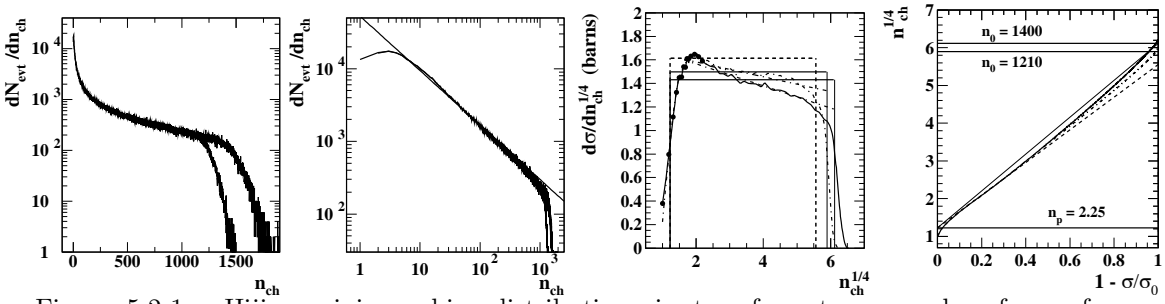


Figure 5.2-1. Hijing minimum-bias distributions in two formats, power-law form of minimum-bias distributions on $n_{ch}^{1/4}$, running integrals of the minimum-bias distributions.

In Fig. 5.2-1 (left panels) we show minimum-bias distributions on multiplicity for the Hijing Monte Carlo. The important feature is the power-law trend in the second panel $\propto n_{ch}^{-3/4}$ (line). The power-law trend immediately implies that the minimum-bias distribution plotted on $n_{ch}^{1/4}$ should be almost uniform. That expectation is confirmed in the third panel. The solid curve is quench-on, the dash-dot curve quench-off Hijing. The upper half-maximum points of those distributions correspond to central A-A ($b = 0$), thereby providing an accurate correspondence between A-A geometry and a physical observable for central collisions.

In the fourth panel we show running integrals of the distributions in the third panel on fraction of total cross section in the form $1 - \sigma/\sigma_0$. For 100% event efficiency the two Hijing curves (solid, dash-dot) coincide for peripheral collisions with a *participant-scaling* hypothesis ($n_{ch} = n_{NN} \cdot n_{part}/2$) represented by the dashed line. Requiring the same correspondence in data leads to accurate centrality determination for peripheral collisions, even if the measured minimum-bias distribution on $n_{ch}$ is severely distorted due to triggering and event-reconstruction inefficiencies. A correspondence can be made between the running integrals of the observable $n_{ch}$ and the geometry parameter $n_{part}/2$ (participant-pair number derived from a Glauber simulation) by adjusting the effective fraction of total integrated cross section to match the running integrals, an extrapolation constraint. We find that the constraint permits accurate centrality definition for all reconstructed events. This new capability allows us to isolate N-N collisions from the A-A minimum-bias sample to serve as a reference for unraveling A-A collision dynamics. We observe that the physics of RHIC A-A collisions evolves rapidly over the full centrality range from N-N to $b = 0$.

## 5.3 Precision Glauber-model parameterizations and particle production in A-A collisions

D. J. Prindle and T. A. Trainor

The centrality problem in A-A collisions has two parts: 1) relate an observable such as $n_{ch}$ in some detector acceptance to the fraction of total cross section $\sigma/\sigma_0$, and 2) relate the fraction of total cross section to the geometry of the A-A collision *via* a Monte Carlo simulation. The fraction of total cross section is a dummy parameter in that process. Using the power-law form of the minimum-bias distribution $\propto n_{ch}^{-3/4}$ we have made great strides in improving the accuracy of centrality determination at RHIC. This article relates to the second aspect above.

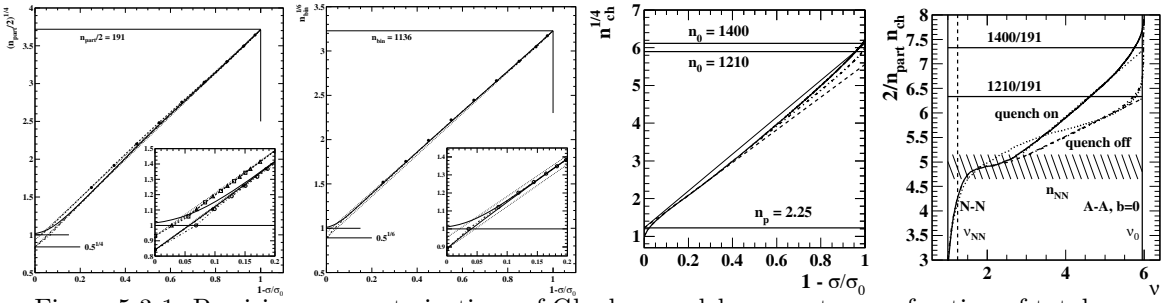


Figure 5.3-1. Precision parameterizations of Glauber-model parameters on fraction of total cross section, running integrals of Hijing minimum-bias distributions, the centrality dependence of particle production going to the correct asymptotic limit ($\sim 5$) for N-N collisions ($\nu = 1$).

We observe that the power-law form of the minimum-bias distribution on participant-pair number $(n_{part}/2)^{1/4}$ is almost perfectly uniform from the lower endpoint $(n_{part,p}/2)^{1/4}$ to the upper endpoint $(n_{part,0}/2)^{1/4}$, except for a small sinusoidal component. The running integral of that distribution provides the desired connection between $n_{part}$ and $\sigma/\sigma_0$. In Fig. 5.3-1 (first panel) we show several running integrals and points from the same relation defined by bin averages (STAR collaboration). We have argued that the lowest curve in the main panel and inset is correct for most data. The differences lie mainly in what is adopted as the lower endpoint $n_{part,p}/2$, and that choice depends on the definition of a participant nucleon. Based on simulations we conclude that the correct choice is $n_{part,p}/2 \sim 1/2$, whereas the conventional choice at RHIC is $n_{part,p}/2 \sim 3/4$. The second panel relates the number of binary collisions to fractional cross section $n_{bin}$ *vs* $\sigma/\sigma_0$. That relation is unambiguous.

In the third panel we show data from Hijing as an example of relating observable $n_{ch}$ to the fractional cross section, the accuracy greatly improved by imposing an extrapolation constraint on peripheral data in relation to participant scaling (dashed curve). The fourth panel shows the two parts of the centrality problem brought together. The centrality measure is $\nu = 2n_{bin}/n_{part}$, which has the great advantage that errors in centrality determination cancel to a great extent in that ratio. The particle production is measured by $2/n_{part} \cdot n_{ch}$. If the Glauber parameters are not properly registered to the observable $n_{ch}$ large systematic errors ($\rightarrow 50\%$) can enter the ratio. In the present case systematic errors are negligible, and the ratio goes asymptotically to the known N-N multiplicity $\sim 5$ in two units of $\eta$ for $\nu \rightarrow 1$. The dotted curve shows the result of omitting the sinusoid from the $n_{part}/2$ parameterization.

## 5.4 Charge-independent angular autocorrelations in Au-Au collisions at $\sqrt{s_{NN}} = 62$ and 200 GeV

M. Daugherity*, D. T. Kettler, R. L. Ray* and T. A. Trainor

The STAR collaboration has accumulated a large event sample of Au-Au collisions at $\sqrt{s_{NN}} =$ 62 and 200 GeV. We have completed a two-particle correlation analysis of those data with optimized analysis methods. The result is 2D (joint) angular autocorrelations of like-sign (LS) and unlike-sign (US) charge-pair combinations, further combined to charge-independent (CI) and charge-dependent (CD) combinations corresponding to isoscalar and isovector correlations respectively. The autocorrelations are distributions on difference axes $\eta_\Delta = \eta_1 - \eta_2$ and $\phi_\Delta = \phi_1 - \phi_2$, shown in Fig. 5.4-1 along with 2D model fits.

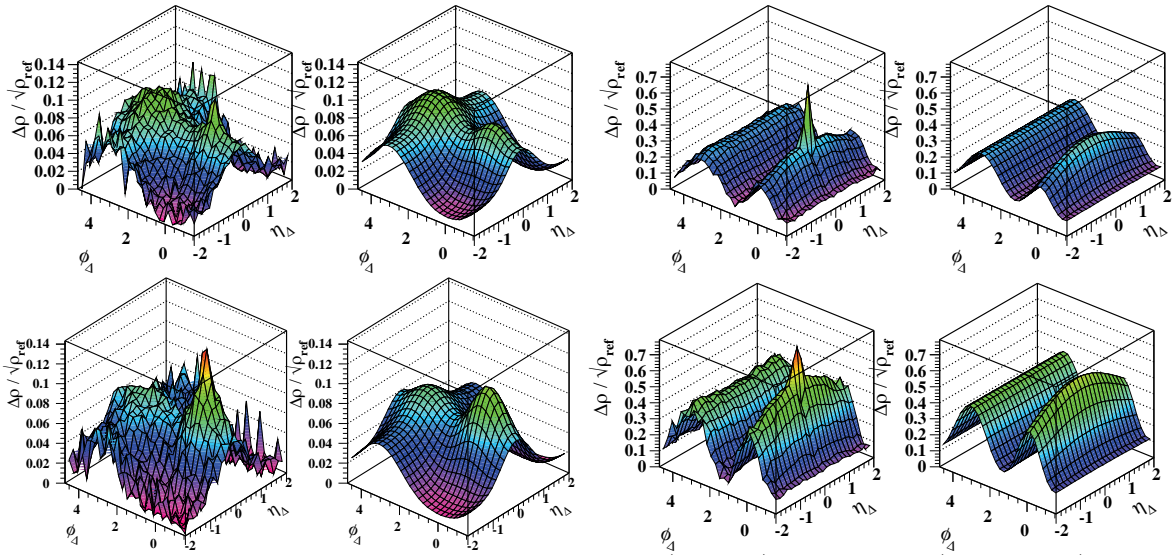


Figure 5.4-1. CI joint angular correlations for 62 GeV (top row) and 200 GeV (bottom row) Au-Au collisions and for 90-100% central collisions (left pairs) and 5-10% central collisions (right pairs). Each pair of histograms consists of data on the left and model fit on the right.

The 2D model fits consist of several components: 1) a same-side ($\phi_\Delta < \pi/2$) 2D gaussian (jet cone), 2) a 1D gaussian on $\eta_\Delta$ ("string fragmentation," most obvious in peripheral collisions at left), 3) a dipole component $\propto \cos(\phi_\Delta)$ (momentum conservation and away-side jet ridge), 4) a quadrupole component $\propto \cos(2\phi_\Delta)$ ("elliptic flow"), 5) a narrow 2D peak at the origin dominated by electron pairs from photon conversions (not shown in the model histograms but included in fits). Those data represent a qualitatively new level of accuracy in correlation measurement, both in histogram structure and centrality accuracy. The left-hand histograms represent the most peripheral Au-Au centrality bin (90-100%), equivalent to N-N collisions. Centrality is accurate to $< 2\%$ from N-N collisions to $b = 0$ Au-Au collisions. The energy and centrality systematics from those fits provide qualitatively new information about minijet energy dependence, azimuth multipoles, the relation of the azimuth quadrupole (so-called elliptic flow) to hydrodynamics and other possible mechanisms, the relation of low-$Q^2$ partons to the reaction plane, parton dissipation in the medium and QCD medium properties.

*University of Texas at Austin, Department of Physics, College of Natural Sciences, 1 University Station C1600, Austin, TX 78712.

## 5.5 Particle identified two particle correlations: techniques

D. Prindle and T. A. Trainor

In relativistic heavy ion collisions there is often a distinction made between probes, usually rare high-momenta particles, and the medium, the vast majority of particles produced in the collision. Instead of looking for modifications of the characteristics of probes and inferring properties of the medium we have developed techniques that allow us to study the medium more directly. Measuring autocorrelations of unidentified charged particles we have made observations such as signatures of local charge conservation[1] and the recoil of the medium from high-$p_t$ particles.[2] Now that we can identify most low-momentum particles via dE/dx in the STAR TPC it seems natural to consider the possibility of observing production mechanisms of strangeness and baryon number. For example, we might be able to see signatures local strangeness and/or baryon conservation

As detailed previously,[3] we first reject all particles within $1\sigma$ of the expected $e^{\pm}$ dE/dx value for their measured momenta. Tracks within $2\sigma$ of the expected dE/dx value for $\pi^{\pm}$, $K^{\pm}$ or p ($\bar{p}$) and more than $2\sigma$ away from the other bands are identified as $\pi^{\pm}$, $K^{\pm}$ or p ($\bar{p}$) respectively. We also exclude the relativistic rise region from consideration. Roughly half of all measured particles are identified as $\pi^{\pm}$. About 5% of all measured particles are identified as $K^{\pm}$ and another 5% as p ($\bar{p}$). The momentum range covered is below the range in which we observe mini-jet phenomena and we do not expect to observe useful $(y_t, y_t)$ correlations in this range. Thus we limit our measurements to joint autocorrelations on $(\eta_\Delta, \phi_\Delta)$ for number and $p_t$.

With unidentified charged particles we typically look at pair correlations among only particles of the same charge sign (LS, Like Sign) or among pairs with opposite sign (US, Unlike Sign). The physics seems to be reasonably separated according to linear combinations of those referred to as charge dependent (CD = LS - US) and charge independent (CI = LS + US). With identified particles we can additionally look at correlations such as $\pi - \pi$ and covariances such as $\pi - K$. Correlations such as HBT are expected to show up only in the LS for the same particle species. Other types of correlations, such as Coulomb attraction/repulsion, should show up in both LS and US but in different ways.

The extension of our framework to identified-particle analysis was straight forward for number correlations. One choice we have not settled yet is whether to continue using pseudo-rapidity or to switch to real rapidities since we are measuring particle masses. During our first pass we used pseudo-rapidity to compare more easily with our previous measurements.

For $p_t$ correlations we have the complication that each particle species has a different mean $p_t$. With unidentified particles we had a single mean $p_t$ but for identified particles we need to measure the mean $p_t$ for each of the populations.

[1] CENPA Annual Report, University of Washington (2004) 53.
[2] CENPA Annual Report, University of Washington (2005) 77.
[3] CENPA Annual Report, University of Washington (2006) 74.

## 5.6 Identified-particle two-particle correlations: observations

D. Prindle and T. A. Trainor

We have made a first pass through some of the AuAu 200 GeV and CuCu 62 GeV data to see what sort of correlations of identified particles can be studied via autocorrelations on $(\eta_\Delta, \phi_\Delta)$ of number or $p_t$. In addition we have run some Hijing simulations where mis-identified particles are not a problem.

Some observed correlations are not included in Hijing. For LS $\pi\pi$ pairs the data show very strong correlations in both number and $p_t$ due to HBT. HBT is extensively studied with specialized techniques and is mostly a background for us. Most LS, US and CI correlations with enough statistical power show a strong centrality-dependent $\cos(2\phi_\Delta)$ term. Since we can exclude structures that are localized on $\eta_\Delta$ we may be able to make interesting flow measurements for identified particles. Another correlation that is not included in Hijing is Coulomb attraction/repulsion. Examples of this are shown in panels 1 and 2 of Fig. 5.6-1. We see there are fewer LS but more US $\pi$K pairs at small separation angles than one would expect in the absence of final state Coulomb interactions. These correlations are also studied with specialized techniques and may be just background for us.

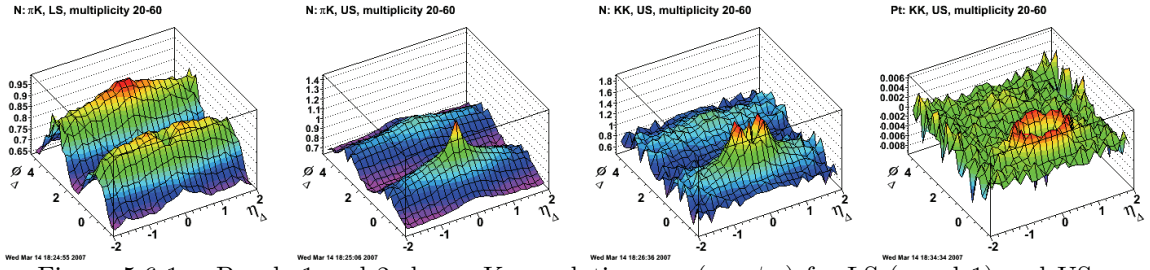


Figure 5.6-1. Panels 1 and 2 show $\pi$K correlations on $(\eta_\Delta, \phi_\Delta)$ for LS (panel 1) and US (panel 2). These show Coulomb repulsion and attraction at small angles. Panel 3 shows $K^+K^-$ number correlations and panel 4 shows $K^+K^-$ $p_t$ correlations on $(\eta_\Delta, \phi_\Delta)$. These are evidence of an object fragmenting and locally producing strangeness.

One unexpected correlation in Hijing as well as data is observed in the US KK pairs, shown in panels 3 and 4 of Fig. 5.6-1 for number correlations and $p_t$ correlations. In the number correlations there is a near-side peak on a $\cos(2\phi_\Delta)$ structure. The peak has a suppression at small angle difference (although there is a narrow one-bin spike at very small separation angles due to mis-identified $e^+e^-$ pairs). The $p_t$ correlations do not have an obvious $\cos(2\phi_\Delta)$ structure and the near-side peak is more of a ring. Our hypothesis for these structures is an object that fragments into a $K^+K^-$ pair. In the rest frame of that object the kaons will be back to back, with a characteristic momentum $j_t$. After boosting to the lab frame and choosing a random decay angle we see the projection of this sphere in the number correlations. For the $p_t$ correlations, if the decay angle is perpendicular to the direction of observations, the momenta of the kaons will be positively correlated. On the other hand if the decay angle is along the observation direction the kaon momenta will be anti-correlated. While not as striking as in $K^+K^-$ pairs it appears that similar types of fragmentation are observable in other pairs.

## 5.7 Forward-backward correlations in relation to angular autocorrelations

T. A. Trainor

The correlation measurement method known as "forward-backward" (FB) correlations has a long history in high-energy nuclear physics. It was used to establish that quarks carry quantum numbers for instance, a form of *long-range* correlations (LRC) (extending across the kinematic limits on rapidity). More recently, FB correlations have been applied to heavy ion collisions to search for LRC as evidence for multiple parton scattering and a dense QCD medium. The measurement method is based on Pearson's normalized covariance obtained for multiplicity fluctuations in bins on $\eta$ symmetrically placed in forward and backward hemispheres (hence, FB), defined as $b \equiv \overline{(n_f - \bar{n}_f)(n_b - \bar{n}_b)}/\sqrt{\sigma^2_{n_f}\,\sigma^2_{n_b}}$. Evidence for LRC is obtained by the procedure $LRC \equiv b_{AA} - x\,b_{NN}$, where $x$ is an arbitrary factor and $b_{AA}$ is determined for several A-A centralities. That procedure resulted in tentative identification of a correlation structure with minimum at $\eta_\Delta = 0$ ($\eta_\Delta$ measures the $\eta$ interval between F and B bins symmetric about $\eta = 0$). However, $b$ is simply related to correlation measure $\Delta\rho/\sqrt{\rho_{ref}}$, and the claim of LRC is inconsistent with published measurements using the latter quantity.

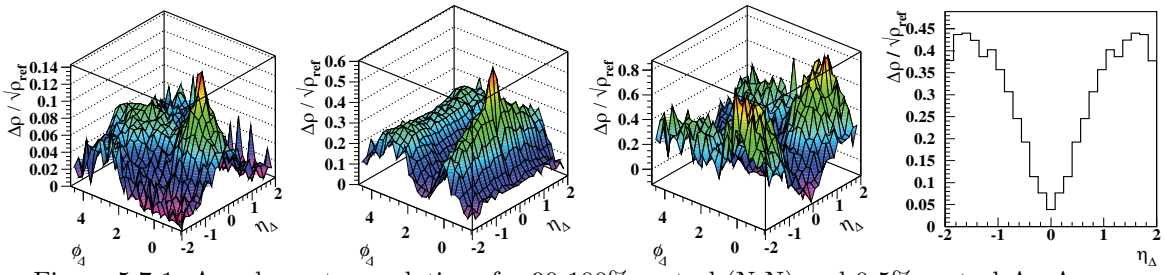


Figure 5.7-1. Angular autocorrelations for 90-100% central (N-N) and 0-5% central Au-Au collisions at 200 GeV, the difference $(\nu_{NN} \sim 1)H_{AA} - (\nu_{AA} \sim 6)H_{NN}$ of those histograms, and a 1D projection of that difference histogram onto $\eta_\Delta$.

The relation is $\Delta\rho/\sqrt{\rho_{ref}} \sim b/\epsilon_\eta\epsilon_\phi$, where for a typical 1D FB analysis the bin-width factor is $\epsilon_\eta\epsilon_\phi \sim 0.2 \times 2\pi \sim 1$. In Fig. 5.7-1 (left panels) we show 2D angular autocorrelations relevant to a typical FB analysis. Due to the relation just cited the 1D projections *by averaging* of those distribution onto $\eta_\Delta$ should be equal to the $b$ distribution within an $O(1)$ factor. In the third panel we show the result of subtracting the N-N distribution times 6 from the central Au-Au distribution. The fourth panel shows the projection by averaging of the third panel onto $\eta_\Delta$, quantitatively very similar to FB distributions claiming to demonstrate LRC.

However, the structures in the left two panels are well studied and precisely modeled with simple functions. Thus, the structures in the right two panels can be identified as to origin. In the third panel the depression at $\eta_\Delta = 0$ uniform on $\phi_\Delta$ is just the positive 1D gaussian on $\eta_\Delta$ in the first panel, which is "string" fragmentation, or more likely longitudinal gluon $\rightarrow \pi^+$-$\pi^-$ reflecting the gluon $k_t$ distribution and charge conservation. The additional positive same-side structure ($\phi_\Delta < \pi/2$) is $\eta$ *broadening* of the same-side minijet peak previously observed and published. The broadening is here manifested by subtracting the unbroadened N-N peak from the center of the A-A peak. All structure in the right two panels results ironically from SRC – short-range correlations from longitudinal or transverse single-parton fragmentation.

## 5.8 Monte Carlo simulations of correlation structures

D. T. Kettler and T. A. Trainor

We have used two-particle correlations extensively as a tool to study the physics of heavy ion collisions. However actual heavy ion collisions are complicated processes with many potential sources of correlation. In order to probe the response of two-particle correlation functions to a known input it is useful to have simple, well-understood simulations that produce specific correlations. In this case, the goal is not to have a detailed simulation of the physics of heavy ion collisions—which are quite complex and outside the scope of this project—but rather to understand qualitatively how specific features would be represented in our analysis so that we can better model and interpret the results.

We explore three different types of correlation signal with these Monte Carlo simulations. First there are minijets described by two or more particles distributed according to a two-dimensional gaussian probability function about the jet center. The number of particles in a minijet is determined according to a Poisson distribution. The correlation from minijets alone is shown in the first panel. The second source of correlation comes from flow terms. Both $v_1$ and $v_2$ terms can be described, though $v_1$ is typically set to zero. These terms are implemented by first randomly selecting a true reaction plane and then biasing the distribution of single particles and minijet centers by sinusoids. The correlation from elliptic flow alone is shown in the second panel.

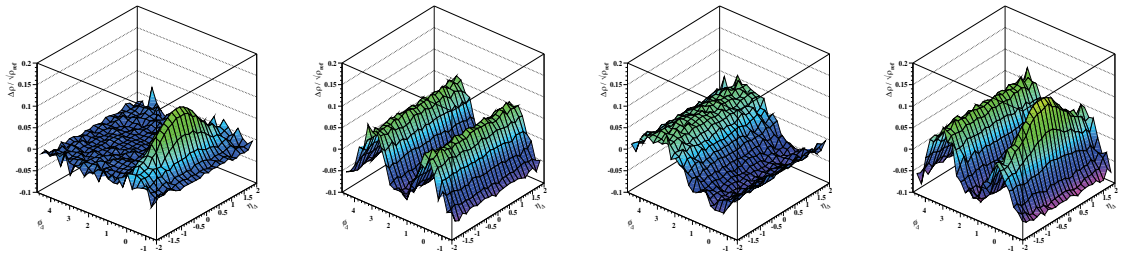

Figure 5.8-1. Monte Carlo results for different types of correlation signals

The third source of correlations is motivated by exploring the effects of momentum conservation. The details of the collision are not modeled, and there are many different ways to conserve momentum, so it is necessary to explore a number of different algorithms and compare them to data. For instance, if we assume that most events are dominated by back-to-back scattering of partons we could generate single particles and minijets in roughly back-to-back pairs. A more general approach is to give each particle a momentum and keep a running total of the momentum of the system as particles are added. The magnitude and direction of that momentum can then be used to bias the probability distribution for the next particle. This is the approach that was taken to produce the plot in the third panel. The simple $\cos(\phi_\Delta)$ curve that results agrees with the data.

The fourth panel is a combined plot of all correlations, which is qualitatively similar to real data.

## 5.9 Reaction-plane-dependent correlations

D. T. Kettler and T. A. Trainor

It is possible to measure the elliptic flow parameter $v_2$ directly from fits to two particle autocorrelations without determining a reaction plane. However, that does not mean that estimating a reaction plane is never useful. To study minijet structures relative to the reaction plane we must calculate reaction-plane-dependent correlations.

A standard $(\phi_1, \phi_2)$ correlations analysis has no structure on the $\phi_\Sigma$ axis, as it is constructed from many events with different orientations relative to the detector. An example is shown in the first panel based on a Monte Carlo. Now, what happens if we plot $(\phi_1 - \psi_2, \phi_2 - \psi_2)$, where $\psi_2$ is the estimate of the reaction plane determined from $\vec{Q}_2 = \sum_{i=1}^{n} r_i \vec{u}(2\phi_i)$? These results are very sensitive to how the reaction plane is estimated. The second panel shows the 'ideal' result for a Monte Carlo simulation using the true reaction plane and the same parameters as for the first panel.

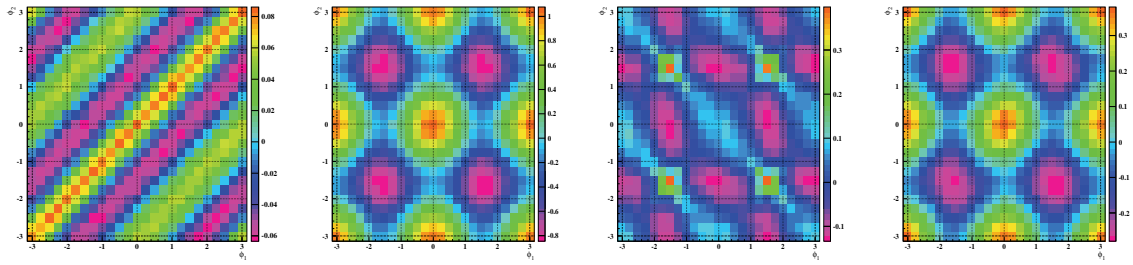

Figure 5.9-1. $(\phi_1, \phi_2)$ correlations

We take as a necessary but not sufficient criterion for a reaction-plane estimation algorithm that for uncorrelated data the $(\phi_1 - \psi_2, \phi_2 - \psi_2)$ plot should have no correlations induced by the reaction-plane estimation algorithm itself. The standard method to deal with such unwanted correlations when calculating $v_2$ is to calculate a different reaction plane for each particle in an event with that particle removed. When constructing a full two-particle $(\phi_1 - \psi_2, \phi_2 - \psi_2)$ correlation we find that this approach is not sufficient. Panel three shows the result of randomly generated uncorrelated data subject to that algorithm.

We find that the only way to avoid such artificial correlations is to exclude tracks that were used in the estimation of the reaction plane from the two-particle correlation. In other words, an event is split into two random subevents and the reaction plane is estimated within one subevent and the correlation is calculated within the other subevent. That approach satisfies the criterion that for uncorrelated data there are no artificial correlations introduced. However it can also have the effect of reducing the observed correlation strength. Further study is needed. Results using that technique with the same Monte Carlo parameters as the first two panels are shown in the fourth panel.

## 5.10 Distinguishing elliptic flow from "non-flow" in heavy ion collisions

D. T. Kettler and T. A. Trainor

A large effort has been devoted by the RHIC community to the study of elliptic flow for the purpose of confirming that thermalized QCD matter has been created. By elliptic flow is meant the azimuth correlation $\langle\cos(2[\phi-\Psi_r])\rangle$ of particles relative to the A-A reaction-plane angle $\Psi_r$ defined by the impact parameter and the collision axis. In the *standard method* of flow analysis particles are related to an estimate of the reaction plane called the event plane (inferred from the particles themselves). Various strategies are introduced to eliminate a systematic error notionally referred to as "autocorrelations" resulting from self-pair contributions. The result is a system of flow measurements with large systematic uncertainties due to uncontrolled statistical bias and contributions from physical mechanisms other than "flow" called "nonflow." Alternatively, the quadrupole component of azimuth correlations can be obtained from 2D angular autocorrelations (legitimate mathematical entities, not a systematic error). By so doing, ambiguities between "flow" and "nonflow" are eliminated.

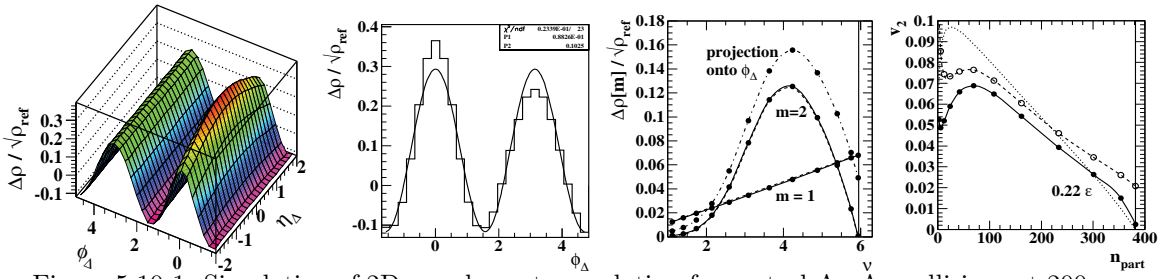


Figure 5.10-1. Simulation of 2D angular autocorrelation for central Au-Au collisions at 200 GeV, projection of that distribution onto $\phi_\Delta$ with fit, summary of multipole amplitudes from 2D model fits to simulated data (solid curves) and 1D projections (dash-dot curve), the same results for $m = 2$ (quadrupole) plotted in the conventional flow context.

In Fig. 5.10-1 (first panel) we show a model of a 2D angular autocorrelation (plus statistical noise) consistent with RHIC data for central Au-Au collisions. In the second panel the projection by averaging of that distribution onto difference axis $\phi_\Delta$ is shown, with a 1D sinusoid fit equivalent to a standard event-plane flow analysis. In the third panel we summarize trends from RHIC data (solid curves) used to construct model distributions, and the corresponding 2D fit results (dashed curves). The agreement is excellent. In contrast, the 1D fit results corresponding to conventional flow analysis (dash-dot curves) return large systematic deviations. The plotting format of the third panel is a pair of optimized measures: the quadrupole component of the density ratio $\Delta\rho[2]/\sqrt{\rho_{ref}}$ and mean participant path length $\nu$. Each can be transformed to a conventional measure as shown in the fourth panel. That plot compares well to published flow data, confirming that conventional flow analysis incorporates a large fraction of "nonflow" (known in other contexts as minijets) into the flow measurement. Attempts to reduce the systematic error by alternative analysis strategies, such as four-particle cumulants, are based on strong model assumptions favorable to the hydrodynamic hypothesis, and therefore cannot be determining. In contrast, analysis of angular correlations based on 2D autocorrelations eliminates to a large extent unwanted cross-talk among several dynamical mechanisms.

## 5.11 Energy and centrality dependence of elliptic flow in Au-Au collisions

D. T. Kettler and T. A. Trainor

Measurement of elliptic flow is seen as an essential means to demonstrate that heavy ion collisions at RHIC produce thermalized QCD matter. In the conventional picture if elliptic flow (azimuth quadrupole moment) as measured by Fourier amplitude $v_2$ becomes proportional to the initial-state configuration-space eccentricity $\epsilon$ with increasing collision energy and A-A centrality that trend would indicate that a hydrodynamic limit has been achieved. Thus, it is important to obtain accurate measurements of this phenomenon on energy and centrality. We have recently achieved a new level of accuracy by inferring azimuth multipole structure from 2D angular autocorrelations.

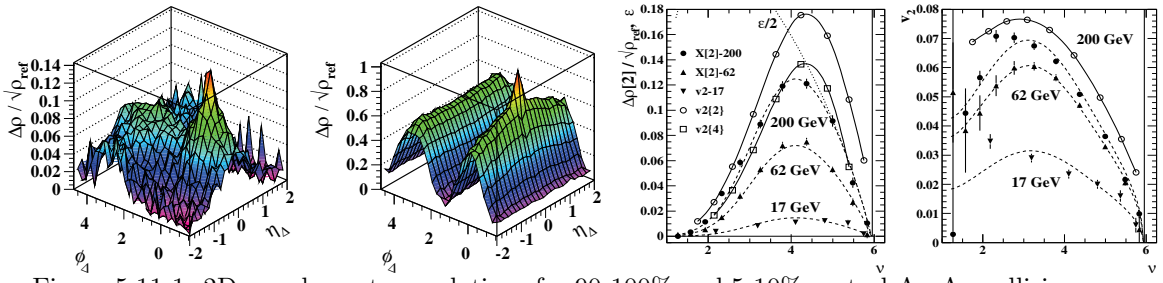


Figure 5.11-1. 2D angular autocorrelations for 90-100% and 5-10% central Au-Au collisions at 200 GeV, inferred quadrupole amplitudes *vs* centrality measure $\nu$ for three collision energies, and the same data converted to conventional flow measure $v_2$.

In Fig. 5.11-1 (left panels) we show angular autocorrelations for 90-100% central and 5-10% central Au-Au collisions at 200 GeV. Similar data were obtained for 62 GeV. Those data were fit with a five-component 2D model, of which one element is azimuth quadrupole term $\cos(2\phi_\Delta)$ with $\phi_\Delta = \phi_1 - \phi_2$. The amplitude of the quadrupole term in the 2D fit is $\Delta\rho[2]/\sqrt{\rho_{ref}} \equiv V_2^2/2\pi\bar{n}$, with $V_2^2/\bar{n} \equiv \bar{n}v_2^2$ defining an unbiased version of conventional flow measure $v_2$. In the third panel we show the amplitude of the quadrupole term *vs* mean participant path-length $\nu$ (number of encountered nucleons) for the present analysis (X[2]-200, 62), a conventional flow analysis ($v_2\{2\}$) and a *four-particle cumulant* analysis ($v_2\{4\}$) based on strong model assumptions. We also include data from the NA49 experiment at $\sqrt{s_{NN}} = 17$ GeV ($v_2$-17). The initial system eccentricity $\epsilon$ is plotted as the dotted curve. In the fourth panel we plot the corresponding values of conventional flow measure $v_2$, also *vs* centrality measure $\nu$.

The results in the third panel provide new insight into the physics of the quadrupole moment. The energy dependence of this quantity, in contrast to $v_2$, is simply given by the trend $\propto \log(\sqrt{s_{NN}}/12\text{ GeV})$, a trend also observed for $p_t$ fluctuations and correlations known to be driven predominantly by minijets. The centrality dependence also has a particularly simple form: $1/\epsilon\,\Delta\rho[2]/\sqrt{\rho_{ref}} \propto \text{erf}([\nu - \nu_0]/\xi_\nu) + 1$, with the shape parameters *independent of collision energy*. The dashed curves in the right panels are derived from those relations. The data are inconsistent with the hydro expectation $v_2 \propto \epsilon$. The simple systematics of these data should prompt a theoretical re-examination of the physics of quadrupole structure.

## 5.12 Is "elliptic flow" a hydrodynamic phenomenon?

T. A. Trainor

It has long been assumed that the azimuth quadrupole term $\langle\cos(2\phi_\Delta)\rangle$ with $\phi_\Delta = \phi_1 - \phi_2$ is associated with a hydrodynamic response to early pressure in asymmetric (noncentral) A-A collisions. In the conventional elliptic flow scenario, in peripheral collisions $v_2/\epsilon$ ($\epsilon$ measures the configuration-space participant eccentricity) should be $\propto 1/S\,dn_{ch}d\eta$, with $S$ the weighted system cross-section area. That so-called LDL (low-density limit) parameter estimates the mean number of collisions of a particle degree of freedom (parton or hadron). For more central collisions it is assumed that the trend $v_2/\epsilon \to$ constant would indicate saturation at a hydrodynamic limit.

With those assumptions comes the conclusion that large elliptic flow exhibiting a certain centrality trend can signal formation of a thermalized QCD medium. Experimental $v_2$ data obtained to date at RHIC have been interpreted in that way. However, with the recent acquisition of more accurate quadrupole moment measurements over a broader centrality range with a model-independent correlation measure there is reason to question those conclusions.

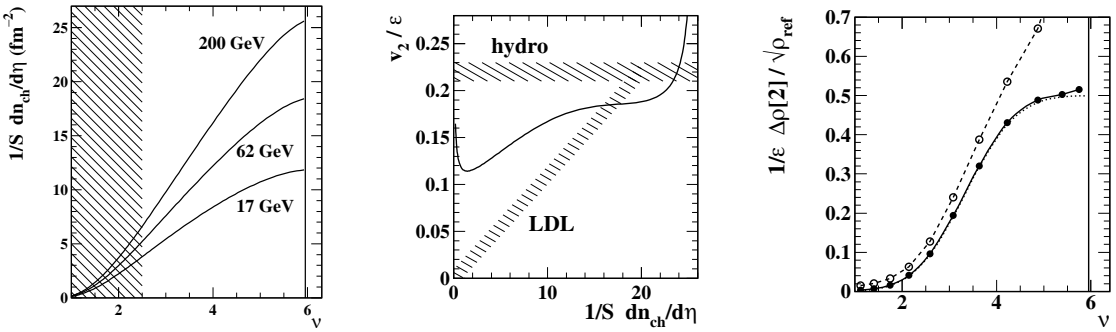


Figure 5.12-1. Relation of LDL parameter $1/S\,dn_{ch}/d\eta$ to mean participant path-length $\nu$ for three collision energies, theoretical expectations for low-density and hydrodynamic trends of $v_2/\epsilon$ contrasted with a summary of recent measurements at 200 GeV, the same trends sketched in a different plotting format for data from 2D autocorrelations (solid curve) and conventional flow measurements (dashed curve).

In Fig. 5.12-1 (left panel) we show the relation between the LDL parameter and centrality measure $\nu$ used in our analysis for three collision energies. Aside from the change in magnitude due to the $n_{ch}$ factor the parameters are nearly proportional, both estimating mean collision numbers. The hatched region is typically omitted from flow measurements due to large systematic errors in $v_2$ and centrality there. In the second panel is the plotting format used to demonstrate asymptotic approach to the hydrodynamic limit (horizontal hatched region) from the low-density limit (diagonal region). Superposed on those expectations is a sketch of accurate quadrupole moment measurements from 200 GeV data. There is strong disagreement with the conventional expectation. The values are large for peripheral collisions (left end) and pass rapidly through the hydro band for central collisions, showing no tendency to saturate at a fixed value. The plotting format in the fourth panel derived from the same data reveals an unanticipated simplicity: a simple error function on $\nu$. That result hints at an underlying mechanisms which is simple but not strictly hydrodynamic.

## 5.13 "Flow" phenomena in nuclear collisions and Brownian motion

D. T. Kettler and T. A. Trainor

There is a close analogy between Brownian motion and the azimuth structure of nuclear collisions. The long history of Brownian motion and its mathematical description can thus provide critical guidance for the analysis of particle distributions. Brownian motion (more generally, random motion of particles suspended in a fluid) was modeled by Einstein as a diffusion process. Fig. 5.13-1 (first panel) shows several steps in a random walk in which the displacements may vary in length. The displacement vectors are plotted in the second panel with the tails at a common origin. In the third panel we show a collision event in the STAR TPC with many particle trajectories. The systems are mathematically equivalent, the TPC data measuring *quasi*-random walk in transverse momentum space: there may be correlations among the walker displacements which we want to measure.

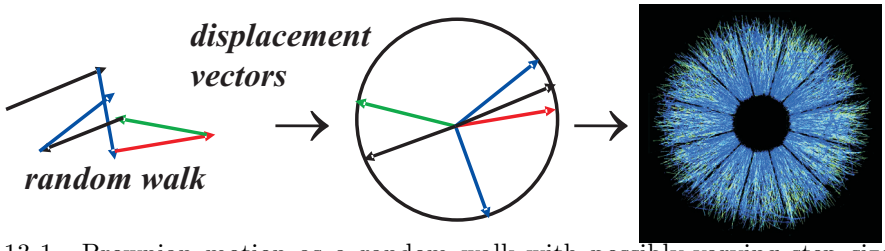


Figure 5.13-1. Brownian motion as a random walk with possibly-varying step size, the displacement vectors of the random walk, and a track distribution in the STAR TPC.

We now consider the close analogy between Einstein's theory of Brownian motion and the measurement of azimuth multipoles in nuclear collisions. Just as $\vec{R}$ is the vector total displacement of a quasi-random walker in 2D configuration space, $\vec{Q}$ is the vector total displacement of a quasi-random walker (event-wise particle ensemble) in 2D momentum space. After $n$ steps the squared displacements are

$$\begin{aligned} R^2 = n^2\,\delta t^2\,v_x'^2 &= n\,\delta t\,4D + n(n-1)\,\delta t^2\,v_x^2 \\ Q^2 = n^2\,p_x'^2 &= n\,\langle p_t^2\rangle + n(n-1)p_x^2. \end{aligned} \tag{1}$$

$4D\delta t$ is the increase in area per step of a random walker in 2D configuration space, with $D$ the diffusion coefficient. $\langle p_t^2\rangle$ is the increase in area per step (per particle) of a random walker in 2D momentum space, playing the same role as the diffusion coefficient. The RHS first term in the first line is the subject of Einstein's 1905 Brownian motion paper. The RHS second term in the second line is the subject of flow analysis (and other correlations) in nuclear collisions. The fractal dimension of a random walk is $d_f = 2$, and the appropriate measure of rate of size increase is the diffusion coefficient (rate of area increase). In contrast, the correlation term represents a deterministic trajectory with nominal dimension 1. The appropriate measure of size increase is linear speed. For quasi-random walks the dimension is not well-defined, and the concept of speed is ambiguous. Attempts to measure the linear speed of Brownian motion in the nineteenth century failed because of the fractal structure of random walks. The same mathematics leads to severe bias in conventional flow measurements for peripheral collisions.

## 5.14 Opacity and chiral symmetry restoration in heavy ion collisions at RHIC: the DWEF model

J. G. Cramer, and G. A. Miller*

Many of the "signals" from analysis of Au+Au collisions at RHIC suggest that a quark gluon plasma (QGP) has been created in the initial stages of the collision. A major problem with such interpretations has been that a QGP scenario would require a large source that has expanded for a long time before freeze out and has a long duration for emission of pions. On the other hand, analysis of RHIC data using HBT interferometry has been interpreted as indicating a relatively small unexpanded source with a very short pion emission duration.

In an effort to understand the origins of this problem, we have taken a new approach to RHIC physics. We have attempted to describe the transport of pions starting at chemical freeze-out within the hot dense medium of the collision, including the effects of opacity, refraction, and wavelike behavior, by using quantum wave mechanics and the nuclear optical model, as reformulated for the "Bjorken tube" collision geometry. We have produced a relativistic quantum mechanical description of the collision medium that includes collective flow as well as pion absorption and refraction in a complex potential. We use conventional "hydro-inspired" emission function, but we interpret it as describing the production of pions at chemical (rather than kinetic) freeze-out. We combine this with pion distorted waves produced by solving the Klein-Gordon wave equation for pions propagating in the post-collision medium. The wave functions are generated using the Numerov algorithm and are used to calculate multidimensional overlap integrals providing predictions of pion momentum spectra and HBT radii. This work has been reported in two previous CENPA Annual Reports and a Physical Review Letters publication.[1]

Last fall we discovered a serious numerical problem within our previous calculations. To obtain the wave functions needed for the calculations, we had solved the Klein-Gordon equation with Runge-Kutta integration using integration routines inherited from older well-tested pion codes. The step-size stability of the calculations had been carefully checked for variation of the HBT radii values, and a "stable" step size of 0.017 fm was used in all searches. However, we discovered recently that the slope of the predicted pion momentum spectrum depended on subtle cancelations among wave functions that were strongly dependent to the integration step size used in wave equation solution. Consequently, the spectrum slope progressively decreased with decreasing step size, with an extremely small step size (0.001 fm or less) required for spectrum slope stability. Calculations with such a small step size require many computation hours to make a single prediction, would invite problems with roundoff errors, and are not useful in parameter searches. The consequence of this problem was that the fit parameter values obtained in previous searches were incorrect because of an unphysical bias that favored large values of the emission temperature and flow. This problem was eliminated by using the more numerically stable and convergent Numerov algorithm to solve the wave equation. This procedure provided fast and reliable predictions at integration step sizes around 0.02 fm.

*supported by the UW Nuclear Theory DOE Contract.

[1] J. G. Cramer, G. A. Miller, J. M. S. Wu, and J-H. Yoon, Phys. Rev. Lett. **94**, 102302 (2005).

The STAR data[2,3] was refitted, leading to the new results that we present here. The new best-fit parameters derived from Levenberg-Marquardt least-squares fits to the STAR 200 GeV Au+Au data are: $T_0$ =156.58 MeV, $\eta_f$ =1.310, $\Delta\tau$ =2.110 fm/c, $R_{WS}$ =11.867 fm, $a_{WS}$ =1.277 fm, w$_0$ =0.0760 fm$^{-2}$, $w_2$ =0.856 +$i$0.116, $\tau_0$ =9.01 fm/c, and $\Delta\eta$ =1.049. The chemical potential was not searched, but rather set to the pion mass, i.e., $\mu_\pi$ =139.57 MeV. The Kisslinger parameter $\epsilon$ was set to zero. For this fit to the data, as shown in Fig. 5.14-1 and Fig. 5.14-2, the $\chi^2$ is 89.63, and the $\chi^2$ per degree of freedom is 4.07. We note that the emission temperature preferred by the fit, $T_0$ = 156.58 MeV, is significantly smaller than that of previous reports, because the slope problem mentioned above has been corrected. The new emission temperature roughly corresponds to estimates of the chemical freeze-out temperature.

With the new version of the DWEF fitting code available, we are continuing to investigate the extension of the model to lower energies and the HBT correlations of other particle species. In particular, we will perform new fits on the NA49 pion spectra and HBT radii over a range of energies.

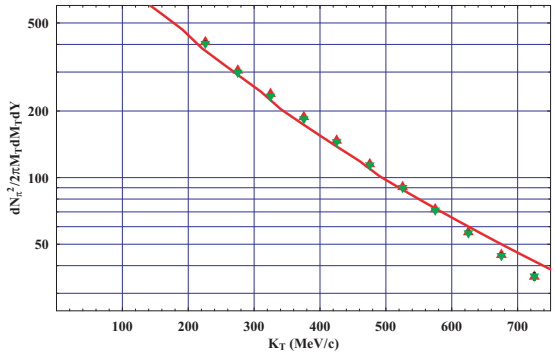


Figure 5.14-1. (Color online) Pion momentum spectrum. Data from ref. 2: $\nabla$ (green) $\Rightarrow \pi^+$; $\triangle$ (red) $\Rightarrow \pi^-$. Solid (red) DWEF fit to these data.

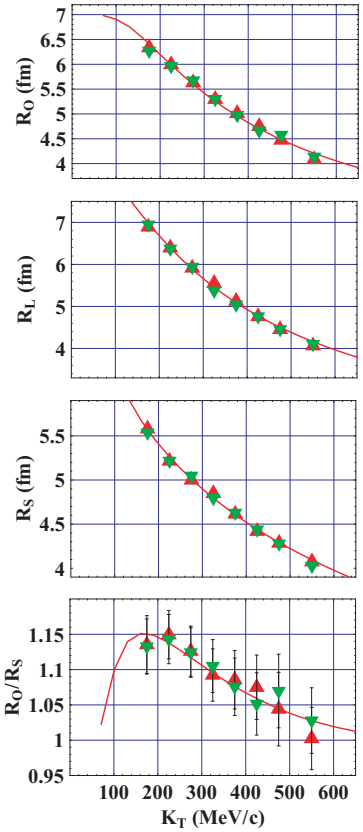


Figure 5.14-2. (Color online) HBT Radii $R_s, R_o,$, $R_l$ and the ratio $R_o/R_s$; Data from ref. 3: $\nabla$ (green) $\Rightarrow \pi^+\pi^+$; $\triangle$ (red) $\Rightarrow \pi^-\pi^-$. Curves: solid (red) DWEF fit to these data

[2]J. Adams and the STAR Collaborators, Phys. Rev. Lett. **92**, 112301 (2004).
[3] J. Adams and the STAR Collaborators, Phys. Rev. C **71**, 044906 (2005).

# 6 Electronics, Computing, and Detector Infrastructure

## 6.1 Electronic Equipment

R. Amitai, G. C. Harper, J. A. Mitchell,* A. W. Myers, T. D. Van Wechel and J. A. White

The electronics shop designed and constructed new laboratory electronic equipment, and maintained and repaired existing CENPA electronics. The electronics shop also supported ongoing efforts at SNO, both from Seattle as well as on-site support at Sudbury Ontario, Canada.

Other projects undertaken by the electronics shop include the following:

1. A PID temperature controller to make calorimetric measurements for the $^3$He+$^4$He experiment was developed. The input to the controller is a two thermistor bridge set up to maintain a set temperature differential. The temperature differential is adjustable between 0 and 3°C. The power required to maintain the temperature differential is recorded.

2. Development work on a parametric amplifier continued. A second prototype parametric amplifier and a demodulator board were designed and constructed. The 2.9 keV FWHM measured resolution of the prototype was poorer than the <500 eV FWHM resolution predicted by SPICE simulations. The dominant source of the excess noise has been traced to phase noise on the externally generated local oscillator (LO) signal. A new parametric amplifier board with an on board differential oscillator and several other improvements is currently being designed.

3. Additional development of a low power and low noise charge input preamplifier with a folded cascode JFET input stage was undertaken.

4. The electronics shop was involved in the design and construction of the External Alpha Counter for the NCD array at SNO. The feedback components of several spare SNO NCD current preamps were modified to convert them to charge preamps.

5. The power supply system of a Wiener 9U VME crate failed. The US factory representative was unable to repair it, so they forwarded it to Germany for repair. In the meantime the electronics shop constructed an array of linear power supplies as a temporary replacement.

6. CENPA has received funding for development of a new Shaper-ADC board. Preliminary research to determine the desired features and specifications for the Shaper-ADC board has begun.

7. Two high voltage power supplies for the KATRIN electron gun were repaired and recalibrated.

*Presently at nanoMaterials Discovery Corp, 2121 N 35th St #201, Seattle, WA 98103.

8. A vacuum controller was designed and built for the new experiment on the 0° beamline.
9. The analyzing magnet NMR oscillator was completely refurbished.
10. Several steerers, beam sweepers, and quadrupoles will be switched between the 0° and left 45° beamlines using a relay controlled transfer box that has been designed and is under construction.
11. A photo tube base was designed and constructed for the LArGe experiment.
12. Two time base counters were constructed for the $^{3}$He+$^{4}$He experiment.
13. Four adjustable current sources for general lab use were constructed.
14. Clean up and reorganization of electronic parts and components in the electronics stock room continues.

## 6.2 Additions to the ORCA DAQ system

J. Detwiler, M. A. Howe and J. F. Wilkerson

The Object-oriented Real-time Control and Acquisition (ORCA) system is an application software tool-kit that is designed for quickly building flexible and robust data acquisition systems. In Nov of 2006, ORCA finished a successful three year run as the production DAQ for the SNO NCD experiment and is now being used to readout an alpha counter to study 'hot spots' on the removed NCD tubes. For the last several months of the SNO experiment, it was also used for the muon tracking system. At CENPA, ORCA is installed in several test stands for the development of the KATRIN pre-spectrometer (see Sec. 1.8) and the Majorana electronics (see Sec. 1.14). Since ORCA has been described extensively in past annual reports[1] only the most recent developments will be reported here.

Improvements to the ORCA infrastructure over the last year include the addition of USB hardware support, a built-in log book, and SQL database interfaces. In addition, the alarm system can now email specified alarms to a list of recipients. Complex 'meta' dialogs were developed for the main KATRIN operator interface that show an overview of both the 145 channel main spectrometer and the 64 channel veto system. A similar dialog was developed for the 64 channel prespectrometer tests.

Support for a number of new hardware devices was implemented. New CAMAC cards included the Joerger ADC-L 16 channel scanning system, BiRa 3251 and 2351 I/O cards, and the LeCroy 4532 logic unit. The CCUSB CAMAC controller was also added, but because some throughput limitations have not yet been solved some work remains. For VME, an 8-channel digitizer developed at LBNL for the Gretina experiment as added. In addition, the HP 33220A pulse generator (USB, IP, and GPIB) and ADU200 Relay I/O controller unit (USB) were included. And finally, support for the KATRIN readout cards (Auger hardware) was completed.

One big advance for ORCA was the development of a scripting language called ORCA-Script. It is a minimalistic interpreted programming language that can be used to automate some ORCA run-time tasks. Among its design goals were that it could be interpreted using a relatively simple lex/yacc based interpreter, provide a C-like language that would be easy to learn, and provide full access to most of the objects in an ORCA configuration without having to add code to those objects. ORCAScripts are created and edited using the ScriptTask object. Scripts are automatically entered into the list of tasks managed by the Task Master and can be executed either from there or from the ScriptTask object itself. Scripts can be chained together to run one after another passing results forward to the next script in the chain. Most C library math functions are included as well as functions that allow scripts to synchronize operations with ORCA run control.

ORCARoot continues to be developed in lock-step with ORCA to fully support ROOT analysis of all of the data that ORCA supported hardware can generate.

[1] CENPA Annual Report, University of Washington (2001) 83; (2002) 81; (2003) 70; (2004) 66; (2005) 85; (2006) 80.

## 6.3 Laboratory computer systems

M. A. Howe, R. J. Seymour, H. E. Swanson and J. F. Wilkerson

This year continued a fairly low rate of additions, upgrades and replacements of existing systems.

Intel's low cost multi-core systems have allowed reasonable performance to be achieved at a $500 price point. A dual 1GHz Pentium III system was retired from central compute serving to become a project's file and web server.

As a part of that rearrangement, all of our central Linux compute servers were brought up to Fedora 6.

We continue using DenyHosts (http://denyhosts.sourceforge.net) on our externally accessible Linux systems to aggressively block access by various attack profiles within a few seconds of their initial probing.

Windows Vista and Office 2007 have been installed on one testbed. So far no unexpected issues have been seen.

Our computing and analysis facility consists of:

- A mix of Linux systems, RedHat v7.3 through v9.0 and Fedora Core 6.
- Twin dual-processor DEC/Compaq/HP Unix AlphaServer 4000s.
- Three VMS/Vaxes and two VMS Alphas for "legacy" computing.
- The SNO, NCD, KATRIN and emiT groups rely upon Macintosh systems.
- One SunBlade 100 workstation serves CADENCE circuit design, analysis and layout duties.
- A VAXstation is the Linac and Vacuum systems' control and display system.
- Three WindowsXP desktop JAM acquisition and analysis systems, plus two laptops for taking to other installations.
- The bulk of CENPA's Windows-based PCs are behind a Gibraltar Linux-based logical firewall using an automated setup procedure developed by Corey Satten of the University's Networks and Distributed Computing group ( http://staff.washington.edu/corey/fw/).
- Although not directly used by Lab personnel, we provide co-location services for the Institute for Nuclear Theory (INT) and the Physics Nuclear Theory group in the form of one VMS Alphastation 500. The Astronomy Department has located a 64-processor Xeon-based Beowulf cluster in our machine room.
- Since the superconducting Linac was mothballed, CENPA is blessed with an excess of power and cooling capacity compared to our current needs. This is a rare commodity on the UW campus. We are working with Physics, INT and Astronomy for providing co-location of a 2.5 to 3.5 teraflop compute facility in our computing room.

## 6.4 Studies of energy losses of fast charged particles

H. Bichsel

The purpose of these studies is to derive energy loss functions $\phi(T, x)$ for charged particles with kinetic energies $T$ traversing absorbers of thickness $x$. In order to explore the uncertainties in Monte Carlo calculations I use computer-analytic methods (for thin absorbers, see http://faculty.washington.edu/hbichsel for a description of such methods). For energy losses in thick absorbers, successive thin layers $\xi$ are combined. Assuming that the function $\phi(T, x)$ is known at a depth $x$ in the absorber, a straggling function $V(T, \xi)$ is calculated for a thin layer $\xi$ and the energy loss functions $\phi(T, x + \xi)$ is calculated with

$$\phi(T, x + \xi) \;=\; \int \phi(T + \chi, x) \;\; V(\chi, \xi; T + \chi) \; d\chi \tag{1}$$

where the energy $T + \chi$ before the layer $\xi$ is reduced to $T$ after this layer.

This method has been used to calculate the results described in Sec. 1.3. No direct comparisons with MC calculations have been made so far. Major applications are for planning of radiation fields for heavy ion cancer therapy.

# 7 Accelerator and Ion Sources

## 7.1 Injector deck and ion sources

G. C. Harper, A. W. Myers, A. L. Sallaska, T. D. VanWechel, J. A. White and D. I. Will

No tandem Van de Graaff acceleration of deck ion beams occurred this past year. The Direct Extraction Ion Source (DEIS) operated only for crew training. $^{23}$Na target development and implantation occupied 40 hours of SPutter Ion Source (SPIS) and injector deck operation.

The DEIS gas needle valve required rebuild to stop a small vacuum leak from the gas line through the valve. This type of valve and its parts are no longer available. When rebuild is next required, we must either make our own parts or replace the whole valve with another style.

The bearings of the beam profile monitor (the scanner) for the deck image region froze. The motor and rotary feedthrough required replacement.

The deck scanner circuitry failed completely and was repaired. The circuit had been intermittently flaky for some years. It accepts a continuous signal of alternating X and Y beam profiles (which could simply be displayed rather cryptically as a single, horizontal scope trace of intensity vs. time, said trace having two vertical peaks when the appropriate sweep rate is chosen). This circuitry parses this single input into two pieces for oscilloscope display: an X profile displayed horizontally with its peak rising from the bottom, and a Y profile displayed vertically with its peak projecting left from the right edge of the scope display. Once the failure was complete, our electronics shop diagnosed and repaired the circuit.

In preparation for measurement of the $^{22}$Na(p,$\gamma$)$^{23}$Mg reaction rate,[1] non-radioactive $^{23}$Na targets are required for tests. $^{23}$Na beam development using the SPIS and injector deck was begun. One rastered target containing roughly 1.7 x $10^{16}$ atoms was prepared and tested. Several new SPIS parts will be installed to decrease neutral Na and Cs migration from the ionizer region, thus increasing useful SPIS lifetime between rebuilds when sodium is sputtered by cesium.

[1] CENPA Annual Report, University of Washington (2006) 51.

## 7.2 Van de Graaff accelerator operations and development

R. Amitai, J. F. Amsbaugh, G. C. Harper, K. G. Jamieson, J. A. Mitchell,*
A. W. Myers, T. D. VanWechel, J. A. White and D. I. Will

The tandem was entered 11 times this year. Two anti-corona rings were touching due to a broken support which was replaced during one opening. The terminal ion source (TIS) parts were replaced during two openings. Gas mixtures of $^4$He and $^{40}$Ar were installed during two openings for plasma poisoning tests. Various TIS canals from 0.5 mm diameter to 0.78 mm diameter were installed during three openings. For one opening, the grid leads, which cross over each other in the TIS oscillator circuit, were found to be shorted and were separated. The low energy charge pickup wheel was replaced during one opening. The low energy georator belt broke and as a result both georator belts were replaced during one opening. Tank gas leaked into the TIS $^4$He gas bottle and that leak was repaired during one opening. Two of the openings were devoted entirely to switching the ion species.

For the plasma poisoning tests, various mixtures of $^{40}$Ar were introduced into $^4$He ranging in concentration from about 1% to about 20%. These tests were intended to produced a stable $^4He^+$ beam at a reduced intensity. Reduced diameter TIS canals were produced and installed for the same reason. These tests failed for reasons not yet understood.

The cooling water flow switch on the switching magnet power supply ruptured and the plastic unit was replaced with a brass one. A water hose in the analyzing magnet power supply ruptured and the hose was replaced and connectored in a more rational manner than it had been. The tandem and accelerator tube were run between 200 kV and 4.5 MV this year. The accelerator was run entirely in single ended mode this year. The only use of the injector deck ion sources was for crew training and ion implantation.

During the 12 months from April 1, 2006 to March 31, 2007 the tandem pellet chains operated 1133 hours, the SpIS 54 hours, and the DEIS 6 hours. We did no molecular research using the deck only this year. Additional statistics of accelerator operations are given in Table 7.2-1.

| **ACTIVITY Scheduled** | **DAYS Scheduled** | **PERCENT of Available time** |
|---|---|---|
| Ion implantation, deck ion sources | 1 | 1 |
| Nuclear physics research, terminal ion source | 85 | 23 |
| Subtotal, ion implant or nuclear physics research | 86 | 24 |
| Machine development, maintenance, or crew training | 52 | 14 |
| Grand total | 138 | 38 |

Table 7.2-1. Tandem Accelerator Operations April 1, 2006 to March 31, 2007

*Presently at nanoMaterials Discovery Corp, 2121 N 35th St #201, Seattle, WA 98103.

## 7.3 Physical plant maintenance, repairs, and possible upgrade

R. M. Coffey, B. J. Fulton, G. C. Harper, K. J. Higgins, D. L. Nastaj, H. Simons, R. J. Seymour, D. W. Storm and D. I. Will

Our facility consists of three structures: the Van de Graaff building, the Cyclotron building, and the Cyclotron Shop building (this last to be renamed the CENPA Instrument Shop building). Last year 254 work requests were placed for our structures: 128 for Van de Graaff, 74 for Cyclotron, and 52 for Cyclotron Shop.

Of these 254 work requests, 251 were paid for by the University. Of these 251 requests more than half, 163, were placed by physical plant personnel as preventive maintenance. Another 23 requests were placed by physical plant staff who noted items in need of repair during routine inspection or preventive maintenance. CENPA staff placed 68 of these work requests for repair of failed or failing items.

The remaining 3 requests by CENPA staff hired services: transportation of the Department of Physics and Astronomy scissor lift twice for research installations and repairs, and one estimate for an upgrade. These services cost $668.

As the result of decommisioning our superconducting linac booster some years back we now have 70 tons of excess chiller capacity plus reserve electrical power equal to several times our current peak usage. This cooling and power are available for modest costs of piping chilled water, running wires and conduit, plus purchase and installation of necessary fan coils. We already host Metate, a Beowulf cluster of 64 processors, for the Departments of Astronomy and of Medicinal Chemistry.[1] The Institute for Nuclear Theory and the Departments of Physics and Astronomy are exploring CENPA's capacity to host a new cluster. The Skagit cluster would have 128 nodes consisting of 256 processors containing a total of 512 cores, each node with 8 gigabytes of memory. It would provide 48 terabytes of disk space. A decision on the location of this cluster is expected in the next month.

[1] CENPA Annual Report, University of Washington (2006) 86.

## 7.4 Axion magnet cryostat: mechanical characteristics*

D. I. Will

The Axion experiment must move from its current location at Lawrence Livermore National Laboratory. The east end of the CENPA accelerator tunnel offers one possible relocation site. Specification of such a long move requires estimates of the magnet cryostat[1] mechanical characteristics since the suspended internal portions of the magnet cryostat account for ≈ 90% of the cryostat mass.

The three vertical 3.00"-diameter 316L stainless-steel helium-tank penetration tubes support the magnet and are loaded to 11,000 psi by the weight of the magnet and tank. This is 28% of the 39,000 psi tubing warm yield strength and 16% of the weldment warm tensile strength.[2,3] The weight of the magnet and tank stretch the tubes ≈ 20 mils where clearances are shown as (or in one case, calculated as) 0.75" for all gaps. The vertical resonant frequency is 20 Hz or higher. For fatigue life greater than 10 million cycles the strain must be kept below 1 part in 250 where 1 g produces a strain of 1/2500 and 2 g produces strain of 1/1250. With vertical accelerations of 1 g due to gravity combined with ± 1 g additional trucking accelerations the strain reaches no more than 56% of warm tube yield strain.

The three 3"-diameter helium-tank tubes not only support the tank vertically but also form a pantograph-like constraint so the tank and magnet could move horizontally. However, the tank and magnet are constrained laterally by four S-2 fiberglass belts. Each belt has cold rupture strength ≈ 35,000 pounds. Lateral acceleration of 0.1 g produces roughly 30 mils lateral displacement where clearances are all 0.375". The resonant frequency for lateral movement is 5 Hz or higher. Fatigue data suggest lifetimes greater than 10 million cycles for stresses less than 10% of the rupture stress, i.e., 3500 pounds or roughly 0.1 g lateral accelerations.

Transportation-induced rotary accelerations (about the vertical axis) are expected to be small, but lateral accelerations beyond belt preload will produce some rotation with belt loads of ≈ 1000 pounds. The resonant frequency for rotation about the vertical axis is 10 Hz or higher. Furthermore, a lateral acceleration limit of 0.1 g will assure that the strain in the three 316L SS helium-tank support tubes (caused by pantograph motions) remains below 1/50 of yield strain.

Should the Axion collaboration decide to move to CENPA, the currently proposed transport specifications would call for realtime monitoring and recording of cryostat accelerations in the truck cab with lateral accelerations limited to 0.05 g and vertical accelerations limited to 0.5 g (about the constant 1 g due to gravity).

*Not supported by DOE CENPA grant

[1] Built a decade ago by Wang NMR, Inc. of Livermore, CA.

[2] Cold regions have higher tensile and yield strengths.

[3] This assumes no top gussets on these tubes. The assembly drawings submitted as part of the proposal show two gussets at the bottom of each three inch diameter tube, but none at the top, for a total of six gussets; however, detail drawings call for the manufacture of 12 gussets. No as-built drawings were provided.

# 8 CENPA Personnel

## 8.1 Faculty

| | |
|---|---|
| Eric G. Adelberger | Professor |
| Hans Bichsel | Affiliate Professor |
| John G. Cramer | Professor |
| Peter J. Doe | Research Professor |
| Alejandro García | Professor |
| Jens H. Gundlach | Professor |
| Isaac Halpern | Professor Emeritus |
| Blayne R. Heckel | Professor |
| R. G. Hamish Robertson | Professor; Scientific Director |
| Stephan Schlamminger[1] | Research Assistant Professor |
| Kurt A. Snover | Research Professor |
| Derek W. Storm | Research Professor; Executive Director |
| Thomas A. Trainor | Research Professor |
| Robert Vandenbosch | Professor Emeritus |
| William G. Weitkamp | Professor Emeritus |
| John F. Wilkerson | Professor |

## 8.2 CENPA External Advisory Committee

| | |
|---|---|
| Baha Balantekin | University of Wisconsin |
| Russell Betts | University of Illinois at Chicago |
| Stuart Freedman | UC Berkeley |

## 8.3 Postdoctoral Research Associates

| | |
|---|---|
| Thomas Brown | Jason Detwiler |
| Seth Hoedl | C. D. Hoyle[2] |
| Daniel Melconian | Scott Pollack[1] |
| Brent VanDevender | |

[1] Not supported by DOE CENPA grant.

[2] Left during 2006; present address: Humboldt State University, One Harpst St., Arcata, CA 95521-8299.

## 8.4 Predoctoral Research Associates

| | |
|---|---|
| Ted Cook[1] | G. Adam Cox-Mobrand |
| Claire Cramer[1] | Charles Duba[2] |
| Charles Hagedorn[1] | Michael Hotz[1] |
| Robert Johnson | Kareem Kazkaz[3] |
| David Kettler | Michelle Leber |
| Michael Marino | Noah Oblath |
| Anne Sallaska | Alexis Schubert |
| Sky Sjue | William Terrano[1] |
| Smarajit Triambak | Todd Wagner[1] |
| Brandon Wall | Hok Seum Wan Chan Tseung |

## 8.5 Research Experience for Undergraduates participants

| | |
|---|---|
| Lia Ball | Middlebury College |
| Amy Crisp | Florida State University |
| Wesley Ketchum | University of Oklahoma |
| Clark Kogan | University of Montana |
| Eric Raymer | Minnesota State University |
| Abe Reddy | North Dakota State University |
| Stephanie Stattel | Holy Cross/Columbia |

## 8.6 University of Washington undergraduates taking research Credit

| | |
|---|---|
| Jacob Barnett | B. Heckel, Advisor |
| Patrick Ellerbroek | K. S. Snover, D. W. Storm, Advisors |
| Corey Fredericks | J. F. Wilkerson, Advisor |
| Mats Fredrickson | D. W. Storm, Advisor |
| Holly Hess | E. Adelberger, Advisor |
| David Hunt | A. García, Advisor |
| Kipp Krause | J. Gundlach, Advisor |
| William Maio | B. Heckel, Advisor |
| Fred March | B. Heckel, Advisor |
| Peter Kirkpatrick Morse | D. W. Storm, Advisor |
| Dan Schultheis | E. Adelberger, Advisor |
| Joseph White | J. Cramer, Advisor |
| David William Zumwalt | D. W. Storm, Advisor |

[1]Not supported by DOE CENPA grant.
[2]Ph.D., June, 2006.
[3]Ph.D., August, 2006.

## 8.7 Professional staff

The professional staff are listed with a description of their recent major efforts.

| | | |
|---|---|---|
| John F. Amsbaugh | Research Engineer | Mechanical design, vacuum systems |
| Tom H. Burritt | Research Engineer | Construction SNO NCD's |
| Gregory C. Harper | Research Engineer | Electronic and mechanical design |
| Mark A. Howe | Research Engineer | Software for DAQ, control systems |
| Sean McGee | Research Scientist | SNO |
| Duncan J. Prindle, Ph.D. | Research Scientist | Heavy ion software |
| Richard J. Seymour | Computer Systems Manager | |
| H. Erik Swanson, Ph.D. | Research Physicist | Precision experimental equipment |
| Timothy D. Van Wechel | Electronics Engineer | Analog and digital electronics design |
| Douglas I. Will | Research Engineer | Cryogenics, ion sources |

## 8.8 Technical staff

| | |
|---|---|
| James Elms | Instrument Maker |
| David Hyde | Instrument Maker |
| Allan Myers | Electronics Technician |
| Hendrik Simons | Instrument Maker, Shop Supervisor |

## 8.9 Administrative staff

| | |
|---|---|
| Kate J. Higgins | Fiscal Specialist |
| Debra L. Nastaj | Administrator |

## 8.10 Part time staff

Rahn Amitai
Corey Fredericks
Kevin Jamieson
Yama Kharoti[1]
Emily Lemagie[1]
Jessica Mitchell[1]
Michael Nickerson[1]
Colin O'Rourke[1]
Daniel Schultheis[1]
Joseph White[1]
Jonathan Will[1]

[1]Left during 2006.

# 9 Publications

## 9.1 Published papers:

"Deep Science," the report of the S1 Principal Investigators on the science and engineering case for a Deep Underground Science and Engineering Laboratory, E. W. Beier, T. C. Onstott, R. G. H. Robertson, B. Sadoulet, and J. M. Tiedje, published by Publications Office, Fermilab (2006).

"Arguments for a "US Kamioka": SNO Lab and its implications for North American underground science planning," W. C. Haxton, K. A. Philpott, R. D. Holtz, J. F. Wilkerson and P. Long, Nucl. Instrum. Meth. A **570**, 414 (2007).

"A search for neutrinos from the solar hep reaction and the diffuse supernova neutrino background with the Sudbury Neutrino Observatory," B. Aharmim and the SNO Collaborators,* Astrophys. J. **653**, 1545 (2006) hep-ex/0607010.

"Measurement of the response of a Ga solar neutrino experiment to neutrinos from an Ar-37 source," J. N. Abdurashitov and the SAGE Collaborators,* Phys. Rev. C **73**, 045805 (2006) nucl-ex/0512041.

"The BNO-LNGS joint measurement of the solar neutrino capture rate in $^{71}$Ga," J. N. Abdurashitov and the SAGE Collaborators,* Astropart. Phys. **25**, 349 (2006) nucl-ex/0509031.

"Measurement of the response of a Ga solar neutrino experiment to neutrinos from an Ar-37 source," J. N. Abdurashitov and the SAGE Collaborators,* J. Phys. Conf. Ser. **39**, 284 (2006) [Phys. Atom. Nucl. **69**, 1820 (2006)].

"New CP-violation and preferred-frame tests with polarized electrons," B. R. Heckel, C. E. Cramer, T. S. Cook, E. G. Adelberger, S. Schlamminger, and U. Schmidt, Phys. Rev. Lett. **97**, 021603 (2006).

"Measurement of Newton's constant," S. Schlamminger, E. Holzschuh, W. Kündig, F. Nolting, R. E. Pixley, J. Schurr, and U. Straumann, Phys. Rev. D **74**, 082001 (2006).

"High sensitivity torsion balance tests for LISA proof mass modeling," S. Schlamminger, C. A. Hagedorn, M. G. Famulare, S. E. Pollack, and J. H. Gundlach, Laser Interferometer Space Antenna: $6^{th}$ International LISA Symposium, June, 2006, *AIP Conference Proceedings*, **873**, 151-157 (2006).

"Outgassing, temperature gradients and the radiometer effect in LISA: A torsion pendulum investigation," S. E. Pollack, S. Schlamminger, J. H. Gundlach, Laser Interferometer Space Antenna: $6^{th}$ International LISA Symposium, June, 2006, *AIP Conference Proceedings*, **873**, 158-164 (2006).

"Quality factors of bare and metal-coated quartz and fused silica torsion fibers,"

C. A. Hagedorn, S. Schlamminger, and J. H. Gundlach, Laser Interferometer Space Antenna: $6^{th}$ International LISA Symposium, June, 2006, *AIP Conference Proceedings*, **873** 189-193 (2006).

"Tests of the gravitational inverse-square law at the dark-energy length scale," D. J. Kapner, T. S. Cook, E. G. Adelberger, J. H. Gundlach, B. R. Heckel, C. D. Hoyle and H. E. Swanson, Phys. Rev. Lett. **98**, 021101 (2007).

"Photon mass bounds destroyed by vortices,", E. G. Adelberger, G. Dvali and A. Gruzinov, Phys. Rev. Lett. **98**, 010402 (2007).

"Particle physics constraints from a recent test of the gravitational inverse-square law," E. G. Adelberger, B. R. Heckel, S. A. Hoedl, C. D. Hoyle, D. J. Kapner and A. Upadhye, Phys. Rev. Lett. **98**, 131104 (2007).

"Precise study of the final-state continuum in $^{8}$Li and $^{8}$B decays," M. Bhattacharya, E. G. Adelberger and H. E. Swanson, Phys. Rev. C **73**, 055802 (2006).

"Mass of the lowest $T = 2$ state of $^{32}$S: A test of the isobaric multiplet mass equation," S. Triambak, A. García, G. J. P. Hodges, E. G. Adelberger, H. E. Swanson, S. A. Hoedl, S. K. L. Sjue and A. L. Sallaska, Phys. Rev. C **73**, 054313 (2006).

"Excitation energies in $^{33}$Cl via $^{32}$S$(p,\gamma)$," S. Triambak, A. García, D. Melconian, M. Mella, and O. Biesel, Phys. Rev. C **74**, 054306 (2006).

"Precision branching ratio measurement for the superallowed $\beta^+$ emitter $^{62}$Ga and isospin-symmetry breaking corrections in $A \geq 62$ nuclei," B. Hyland, C. E. Svensson, G. C. Ball, J. R. Leslie, T. Achtzehn, D. Albers, C. Andreoiu, P. Bricault, R. Churchman, D. Cross, M. Dombsky, P. Finlay, P. E. Garrett, C. Geppart, G. F. Grinyer, G. Hackman, V. Hanemaayer, J. Lassen, J. P. Lavoie, D. Melconian, A. C. Morton, C. J. Pearson, M. Pearson, A. A. Phillips, M. A. Schumaker, M. B. Smith, I. S. Towner, J. J. Valiente-Dobon, K. Wendt, and E. F. Zganjar, Phys. Rev. Lett. **97** 102501 (2006).

"Superallowed beta decay studies at TRIUMF - nuclear structure and fundamental symmetries," E. F. Zganjar, T. Achtzehn, D. Albers, *et al.* (D. Melconian), 2006 Zakopane Conference on Nuclear Physics, Acta Phys. Pol. B **38** 1107 (2007).

"A proposed STAR microvertex detector using active pixel sensors with some relevant studies on APS performance," S. Kleinfelder, S. Li, H. Bichsel, *et al.*, Nucl. Instrum. Methods A **565**, 132-138 (2006).

"Extrapolating parton fragmentation to low $Q^2$ in $e^+ - e^-$ collisions," T. A. Trainor and D. T. Kettler, Phys. Rev. D **74**, 034012 (2006).

"Autocorrelations from the scale dependence of transverse-momentum fluctuations in Hijing-simulated Au-Au collisions at ${s_{NN}}^{1/2} = 200$-GeV," Q. J. Liu, D. J. Prindle and T. A. Trainor, Phys. Lett. B **632**, 197 (2006).

"Transverse momentum correlations and minijet dissipation in Au-Au collisions at $s_{NN}{}^{1/2}$ = 130-GeV," B. I. Abelev, T. A. Trainor and the STAR Collaborators,* J. Phys. G. **34**, 799 (2007).

"The energy dependence of $p_t$ angular correlations inferred from mean-$p_t$ fluctuation scale dependence in heavy ion collisions at the SPS and RHIC," B. I. Abelev, D. J. Prindle, T. A. Trainor and the STAR Collaborators,* J. Phys. G **33**, 451 (2007).

"The multiplicity dependence of inclusive $p_t$ spectra from p-p collisions at $s^{1/2}$ = 200-GeV," B. I. Abelev, T. A. Trainor and the STAR Collaborators,* Phys. Rev. D **74**, 032006 (2006).

"Transverse-momentum $p_t$ correlations on (eta,phi) from mean-$p_t$ fluctuations in Au-Au collisions at $s_{NN}{}^{1/2}$ = 200-GeV," B. I. Abelev, Q. J. Liu, D. J. Prindle, T. A. Trainor and the STAR Collaborators,* J. Phys. G **32**, L37 (2006).

"$e^+e^-$ fragmentation functions," D. T. Kettler and T. A. Trainor, International workshop on Correlations and fluctuations in relativistic nuclear collisions, Florence, Italy, July, 2006, *Proceedings of Science* (CFRNC 2006) 003 (2006).

"Correlations in p-p collisions," R. J. Porter and T. A. Trainor, International workshop on Correlations and fluctuations in relativistic nuclear collisions, Florence, Italy, July, 2006, *Proceedings of Science* (CFRNC 2006) 004 (2006).

"Review of $p_t$ fluctuations and correlations," D. J. Prindle and T. A. Trainor, International workshop on Correlations and fluctuations in relativistic nuclear collisions, Florence, Italy, July, 2006, *Proceedings of Science* (CFRNC 2006) 007 (2006).

"Review of analysis methods for correlations and fluctuations," T. A. Trainor, International workshop on Correlations and fluctuations in relativistic nuclear collisions, Florence, Italy, July, 2006, *Proceedings of Science* (CFRNC 2006) 009 (2006).

"Low-$Q^2$ partons in p-p and Au-Au collisions," T. A. Trainor (STAR Collaboration), 35th International Symposium on Multiparticle Dynamics (ISMD 05), Kromeriz, Czech Republic, August, 2005, V. Simak, M. Sumbera, S. Todorova, B. Tomasik, Editors, *AIP Conference Proceedings* **828**, 238 (2006).

"Energy and centrality dependence of anti-p and p production and the anti-Lambda/anti-p ratio in Pb+Pb collisions between 20/A-GeV and 158/A-Gev," C. Alt and the NA49 Collaborators,* Phys. Rev. C **73**, 044910 (2006).

"Inclusive production of charged pions in p+C collisions at 158-GeV/c beam momentum," C. Alt and the NA49 Collaborators,* Eur. Phys. J. **49**, 897-917 (2007) hep-ex/0606028.

"Upper limit of D0 production in central Pb-Pb collisions at 158-A-GeV." C. Alt and the NA49 Collaborators,* Phys. Rev. C, **73**, 034910 (2006) nucl-ex/0507031.

"Identified hadron spectra at large transverse momentum in p+p and d+Au collisions at $\sqrt{s_{NN}}$ = 200 GeV," B. I. Abelev and the STAR Collaborators,* Phys. Lett. B **637**, 161

(2006) nucl-ex/0601033.

"Strange baryon resonance production in $\sqrt{s_{NN}} = 200$ GeV p+p and Au+Au collisions," B. I. Abelev and the STAR Collaborators,* Phys. Rev. Lett. **97**, 132301 (2006), nucl-ex/0604019.

"Identified baryon and meson distributions at large transverse momenta from Au+Au collisions at $\sqrt{s_{NN}} = 200$ GeV," B. I. Abelev and the STAR Collaborators,* Phys. Rev. Lett. **97**, 152301 (2006) nucl-ex/0606003.

"Forward neutral pion production in p+p and d+Au Collisions at $\sqrt{s_{NN}} = 200$ GeV," B. I. Abelev and the STAR Collaborators,* Phys. Rev. Lett. **97**, 152302 (2006) nucl-ex/0602011.

"Direct observation of dijets in central Au+Au collisions at $\sqrt{s_{NN}} = 200$ GeV," B. I. Abelev and the STAR Collaborators,* Phys. Rev. Lett. **97**, 162301 (2006) nucl-ex/0604018.

"Neutral kaon interferometry in Au+Au collisions at $\sqrt{s_{NN}} = 200$ GeV," B. I. Abelev and the STAR Collaborators,* Phys. Rev. C **74**, 054902 (2006) nucl-ex/0608012.

"Longitudinal double-spin asymmetry and cross section for inclusive jet production in polarized proton collisions at $\sqrt{s_{NN}} = 200$ GeV," Phys. Rev. Lett. **97**, 252001 (2006) hep-ex/0608030.

"Delta-phi delta-eta correlations in central Au+Au collisions at $\sqrt{s_{NN}} = 200$ GeV," B. I. Abelev and the STAR Collaborators,* Phys. Rev. C **75**, 034901 (2007) nucl-ex/0607003.

"Straggling of fast electrons," Z-E-A Chaoui and H. Bichsel, Surf. Inter. Anal. **38**, 664-667 (2006).

"Approximation methods to calculate straggling functions," H. Bichsel, Nucl. Instrum. Methods A **566**, 1-4 (2006).

"A method to improve tracking and particle identification in TPCs and silicon detectors," H. Bichsel, Nucl. Instrum. Methods A **562**, 154-197 (2006).

## 9.2 Papers submitted or to be published 2006:

"Direct Neutrino Mass Measurements," P. J. Doe, *Proceedings of the Neutrino 2006 Conference*, Neutrino 2006 Conference, Santa Fe, NM, June, 2006, accepted for publication in J. Phys. Conf. Ser.

"Operation of a high purity germanium crystal in liquid argon as a Compton suppressed radiation spectrometer," J. L. Orrell, C. E. Aalseth, J. F. Amsbaugh, P. J. Doe, T. W. Hossbach, July, 2006, submitted for publication to Nucl. Instrum. Methods A, nucl-ex/0610018.

"A search for neutrinos from solar hep reaction and the diffuse supernova neutrino background with the Sudbury Neutrino Observatory," B. Aharmim and the SNO Collaborators,* July, 2006, submitted for publication to Astrophys. J., hep-ex/0607010.

"Multi-layer scintillation detector for the MOON double beta decay experiment: Scintillation photon responses studied by a prototype detector MOON-1," H. Nakamura and the MOON Collaborators,* submitted for publication to Nucl. Instrum. Methods, nucl-ex/0609008.

"Measurement of the $\nu_e$ and total $^8$B solar neutrino fluxes with the Sudbury Neutrino Observatory Phase I Data Set," B. Aharmim and the SNO Collaborators,* Phys. Rev. C (in press) nucl-ex/0610020.

"Multi-layer scintillation detector for the MOON double beta decay experiment: Scintillation photon responses studied by a prototype detector MOON-1," H. Nakamura and the MOON Collaborators,* submitted for publication in Nucl. Instrum. Methods, nucl-ex/0609008.

"E0 emission in $\alpha$ + $^{12}$C fusion at astrophysical energies," G. Baur, K. A. Snover, and S. Typel, Phys. Rev. C (in press) nucl-th/0701027v2.

"$ft$ value of the $0^+ \rightarrow 0^+$ $\beta^+$ decay of $^{32}$Ar: a measurement of isospin breaking in a super-allowed decay," M. Bhattacharya, D. Melconian, A. Komives, A. García, E. G. Adelberger, B. A. Brown, M. W. Cooper, T. Glasmacher, V. Guimaraes, P. F. Mantica, A. M. Oros-Peusquens, J. I. Prisciandaro, M. Steiner, H. E. Swanson, S. L. Tabor, M. Wiedeking, submitted for publication to Phys. Rev. C.

"Measurement of the neutrino asymmetry in the $\beta$ decay of laser-cooled, polarized $^{37}$K," D. Melconian, J. A. Behr, D. Ashery, O. Aviv, P. G. Bricault, M. Dombsky, S. Fostner, A. Gorelov, S. Gu, K. P. Jackson, V. Hanemaayer, M. R. Pearson and I. Vollrath, accepted for publication in Phys. Lett. B.

"Polishing the lens: l Pionic final state interations and HBT correlations - Distorted Wave Emission Function (DWEF) formalism and examples," G. A. Miller and J. G. Cramer, 2007, accepted for publication to J. Phys. G, nucl-th/0507004.

"The azimuth structure of nuclear collisions - I," T. A. Trainor and D. T. Kettler, submitted to J. Phys. G, hep-ph/07041674.

"A power-law description of collision centrality applied to Hijing-1.37-simulated Au-Au collisions at $s_{NN}{}^{1/2}$ = 200-GeV," T. A. Trainor and D. J. Prindle, submitted for publication to J. Phys. G, hep-ph/0411217.

"Centrality and system size dependence of multiplicity fluctuations in nuclear collisions at 158-A/GeV," C. Alt and the NA49 Collaborators,* December, 2005, submitted for publication to Phys. Rev. C.

"Elliptic flow of Lambda hyperons in Pb + Pb collisions at 158A- GeV," C. Alt and the

NA49 Collaborators,* 2006, submitted for publication to Phys. Rev. Lett., nucl-ex/0606026.

"Transverse momentum and centrality dependence of high-pT non-photonic electron suppression in Au+Au collisions at $\sqrt{s_{NN}} = 200$ GeV," B. I. Abelev and the STAR Collaborators,* 2006, submitted for publication to Phys. Rev. Lett., nucl-ex/0607012.

"Measurements of strange particle production in p+p collisions at $\sqrt{s} = 200$ GeV," B. I. Abelev and the STAR Collaborators,* 2006, submitted for publication to Phys. Rev. C, nucl-ex/0607033.

"Rapidity and species dependence of particle production at large transverse momentum for d+Au collisions at $\sqrt{s_{NN}} = 200$ GeV," B. I. Abelev and the STAR Collaborators,* 2006, nucl-ex/0609021.

"Mass, quark-number, and $\sqrt{s_{NN}} =$ dependence of the second and fourth flow harmonics in ultra-relativistic nucleus-nucleus collisions," B. I. Abelev and the STAR Collaborators,* 2007, submitted for publication to Phys. Rev. C, nucl-ex/0701010.

"Measurements of identified particles at intermediate transverse momentum in the STAR experiment from Au+Au collisions at $\sqrt{s_{NN}} = 200$ GeV," B. I. Abelev and the STAR Collaborators,* 2006, Phys. Rev. C, nucl-ex/0601042.

"Energy dependence of charged pion, proton and anti-proton transverse momentum spectra for Au+Au collisions at $\sqrt{s_{NN}} = 62.4$ and 200 GeV," B. I. Abelev and the STAR Collaborators,* 2007, submitted for publication.

"Scaling properties of hyperon production in Au+Au collisions at $\sqrt{s_{NN}} = 200$ GeV," B. I. Abelev and the STAR Collaborators,* 2006, submitted for publication to Phys. Rev. Lett., nucl-ex/0606014.

### 9.3 Invited talks, abstracts and other conference presentations:

"Direct neutrino mass measurement and the status of KATRIN," P. J. Doe, NNN2009, Seattle, WA, September, 2006.

"Direct neutrino mass measurements," P. J. Doe, Neutrinos 2006, Santa Fe, NM, June, 2006.

"In pursuit of a solar neutrino flux number from SNO's Phase III," S. McGee, Joint Meeting of Pacific Region Particle Physics Communities, Honolulu, HI, October, 2006.

"Solar Neutrinos," R. G. H. Robertson, *Proceedings of International School on Nuclear Physics*; 27th Course: "Neutrinos in Cosmology, in Astro, Particle and Nuclear Physics" in Erice, Sicily, Italy; September, 2005, Prog. Part. Nucl. Phys. **57** 90-105 (2006) report-no: CENPA 2006-2.

"Tribute to Ray Davis and John Bahcall," R. G. H. Robertson, International Conference on

Neutrino Physics and Astrophysics, Neutrinos 2006, Santa Fe, NM, June, 2006.

"A Deep Underground Science and Engineering Laboratory in the U.S.,"
R. G. H. Robertson, International Conference on Neutrino Physics and Astrophysics, Neutrinos 2006, Santa Fe, NM, June, 2006.

"Neutrinos in nuclear physics, setting a course," R. G. H. Robertson, Pre-Town Meeting for NSAC Long-Range Plan Process, Santa Fe, NM, December, 2006.

"Deep Underground Science and Engineering Lab," R. G. H. Robertson, Pre-Town Meeting for NSAC Long-Range Plan Process, Santa Fe, NM, December, 2006.

"Experimental determination of neutrino mass," R. G. H. Robertson, Aspen Winter Physics Conference, Aspen, CO, January 2007.

"DUSEL Cascades," J. F. Wilkerson, Neutrinos 2006, Santa Fe, NM, June, 2006.

"The Majorana and GERDA $^{76}$Ge Double Beta Decay Experiments," J. F. Wilkerson, Workshop on Next Generation Nucleon decay and Neutrino Detectors, Seattle, WA, September, 2006.

"Next-Generation Neutrinoless Double-Beta Decay Experiments," J. F. Wilkerson, Aspen 2007 Winter Conference on Neutrinos in Physics and Astrophysics, Aspen, CO, January, 2007.

"Digging Neutrinos: Pursuing Science Deep Underground," J. F. Wilkerson, University of South Dakota, Vermillion, SD, February 2007.

"Majorana Experiment Status," J. F. Wilkerson, GERDA Collaboration Meeting, Ringberg, Germany, February 2007.

"A torsion pendulum axion search," S. A. Hoedl, Indiana University Nuclear Physics Seminar, Bloomington, IN, March 2007.

"A torsion pendulum axion search," S. A. Hoedl, Axions at the Institute Workshop, Institute for Advanced Study, Princeton, NJ, November, 2006.

"Exciting physics with torsion balances," S. Schlamminger, Seminar in Experimental Physics, Universität Zürich, January 2007.

"Unitarity of the CKM mass-mixing as a test of the Standard Model: status and future prospects," D. Melconian, APS Northwest Annual Meeting, Tacoma, WA, May, 2006.

"Characterization of solid state ultracold neutron detectors," A. L. Sallaska, A. García, S. K. L. Sjue, S. A. Hoedl, D. Melconian, A. Young, A. Holley, P. Geltenbort, APS Northwest Annual Meeting, Tacoma, WA, May, 2006.

"Polarized neturon beta-decay: proton asymmetry and recoil-order currents," S. K. L. Sjue,, APS Northwest Annual Meeting, Tacoma, WA, May, 2006.

"$^{31}$P($\rho$,$\gamma$) gamma and the isobaric multiplet mass equation," S. Triambak, A. García, E. G. Adelberger, G. J. P. Hodges, D. Melconian, H. E. Swanson, S. A. Hoedl, S. K. L. Sjue,, A. L. Sallaska, H. Iwamoto, APS Northwest Annual Meeting, Tacoma, WA, May, 2006.

"Second-forbidden beta decay of $^{8}$B," M. K. Bacrania, D. W. Storm, and R. G. H. Robertson, American Physical Society, Dallas, TX, April, 2006, Bull. Am. Phys. Soc. **51** 90 (2006).

"Be + p and $^{3}$He + $^{4}$He fusion reactions and neutrino astrophysics," K. A. Snover, Physics Division colloquium, Oak Ridge National Lab, Oak Ridge, TN, May, 2006.

"Analyzing sources of uncertainty in a precision measurement of $^{3}$He$(\alpha, \gamma)^{7}$Be," A. M. Crisp, T. A. D. Brown, C. Bordeanu, K. A. Snover, D. W. Storm, APS Division of Nuclear Physics, Session 3A00018, Nashville, TN, 2006.

"Probing fundamental properties of the weak interaction: Some recent experimental progress," D. Melconian, Physics colloquium, Louisiana State University, Baton Rouge, LA, March 2007.

"Ideas for research at the Cyclotron Institute at Texas A & M University," D. Melconian, Physics seminar, Cyclotron Institute, Texas A& M University, College Station, TX, March 2007.

"Probing fundamental properties of the weak interaction: Some recent experimental progress," D. Melconian, Physics colloquium, Texas A& M University, College Station, TX, March 2007.

"Probing fundamental properties of the weak interaction: What haven't we seen yet?," D. Melconian, Physics colloquium, Colorado School of Mines, Golden, CO, February 2007.

"Correlation measurements using laser-cooled, polarized $^{37}$K," D. Melconian, 2006 Canadian Association of Physicists DNP Thesis Prize, Winter Nuclear and Particle Physics Conference, Banff, Alta, Canada February 2007.

"$\mathcal{F}t$ value for the superallowed decay of $^{32}$Ar," D. Melconian, APS Division of Nuclear Physics Conference, Nashville, TN, October, 2006, Bull. Am. Phys. Soc. **51**, 39 (2006), Session CF.

"Measurement of the $\gamma$ branches in the $\beta^{+}$ decay of $^{32}$Cl," D. Melconian, APS Division of Nuclear Physics Conference, Nashville, TN, October, 2006, Bull. Am. Phys. Soc. **51**, 40 (2006), Session CF.

"Standard Model Tests of the Weak Interaction using the $\beta$-decay of Laser-Cooled $^{37,38m}$K," D. Melconian, physics seminar, Kellogg Radiation Laboratory, California Institute of Technology, Pasadena, CA, March, 2006.

"Minijets in Nuclear Collisions," T. A. Trainor, 1st Workshop on Soft Physics in Ultrarelativistic Heavy Ion Collisions, (SPHIC06) Catania, Italy, September, 2006.

"A parametric amplifier for semiconductor radiation detectors," R. G. H. Robertson and

T. D. Van Wechel, IEEE Conference on Nuclear Science, San Diego, CA, October, 2006.

"Physical processes produced by radiations in water and biological cells," H. Bichsel, National Institutes of Radiological Sciences, Chiba, Japan, October, 2006.

"Detailed study of charged particle interactions in water with application to radiation cancer therapy with carbon ions," H. Bichsel, National Institutes of Radiological Sciences, Chiba, Japan, October, 2006.

*UW collaborators for the various CENPA research groups are listed below (April 1, 2006 - March 31, 2007):

MOON Collaborators: P. J. Doe, R. G. H. Robertson, J. F. Wilkerson and D. I. Will

NA49 Collaborators: J. G. Cramer and D. J. Prindle

SAGE Collaborators: J. F. Wilkerson

SNO Collaborators: J. F. Amsbaugh, T. A. D. Brown, G. A. Cox-Mobrand, J. A. Detwiler, P. J. Doe, G. C. Harper, M. A. Howe, S. McGee, A. W. Myers, N. S. Olbath, R. G. H. Robertson, B. A. VanDevender, T. D. VanWechel and J. F. Wilkerson

STAR Collaborators: H. Bichsel, J. G. Cramer, D. T. Kettler, R. J. Porter, D. J. Prindle and T. A. Trainor. In cases where some CENPA personnel played a major role in a STAR publication, their names are listed explicitly.

## 9.4 Ph.D. degrees granted:

*Finding Excited-State Decays of Germanium-76*, Kareem Kazkaz (August, 2006).

*Electronics for the Neutral Current Detection Array at the Sudbury Neutrino Observatory*, Charles Duba (June, 2006).